Urban Heat Island and its Influencing Mechanism

In the City of Berlin

Dissertation

zur Erlangung des akademischen Grades

des Doktors der Naturwissenschaften

am Fachbereich Geowissenschaften

an der Freie Universität Berlin

Vorgelegt von

Huidong Li

April 2018

Gutachter:

Prof. Dr. Sahar Sodoudi

Prof. Dr. Martijn Schaap

Date of defense: 25 July, 2018

Table of Contents

Abstract

A comprehensive understanding of urban heat island (UHI) can help to evaluate the potential heat risk and to design the mitigation strategies efficiently. This study quantifies the UHI in the city of Berlin and investigates the underlying physical mechanism and influencing factors using the integration of in-situ observation, remote sensing (MODIS), and numerical modelling (WRF). Berlin shows UHI for both observations and simulations. Up-to-date land cover data can contribute to improving the model performance in simulating the UHI, especially in the rural areas. The urban expansion increases the spatial extent of UHI in Berlin but has little impact on the intensity of UHI based on the modelling results. The MODIS LST shows a highly positive correlation with the ISA regionalized by a Kernel Density Estimation method (ISA_{KDE}). The linear functions of LST against ISA_{KDE} are fitted well at both annual and daily scales. The slope of the linear function represents the increase in LST from the natural surface in rural areas to the impervious surface in urban areas and is defined as SUHI intensity. The derived surface UHI intensity shows high values in summer and during the day than in winter and at night. The WRF/UCM simulated 2 m air temperature (T_{2m}) shows a good relationship with the ISA in the WRF grids (ISA_{WRF}). Similarly, the UHI intensity is quantified using the slope of the ISA_{WRF}-based linear functions of the simulated T_{2m}. The derived UHI intensity shows U-shaped diurnal variations, with large values at nighttime. The daytime UHI intensity is low and even negative, due to the shading of the buildings. UHI and urban aerosols can interact with each other. UHI could promote the turbulent dispersion of aerosol particles, decreasing the urban-rural difference in near-surface aerosol concentrations. Urban aerosols affect UHI by reducing the incoming solar radiation and increasing the atmospheric longwave radiation in the urban areas. The response of the surface to the change of the absorbed energy is strong at night and weak during the day. As a result, the surface UHI is enhanced by the urban-rural difference of incoming longwave radiation at night, while is negligibly altered in the daytime, due to the offset of the opposite change of solar radiation

and atmospheric longwave radiation and the weak response of the surface. It is hoped that the study results can contribute to a better understanding of the urban climate in Berlin and can provide useful information for designing the UHI mitigation strategies and urban planning for Berlin.

Zusammenfassung

Ein umfassendes Verstehen der städtischen Wärmeinsel (UHI) kann helfen, potenzielle Hitzebelastung zu bewerten und Mitigationsstrategien effizient zu entwerfen. Diese Studie untersucht die UHI in der Stadt Berlin und untersucht den zu Grunde liegenden physikalischen Mechanismus, sowie den Einfluss von unterschiedlichen Faktoren mit Hilfe von in-situ Beobachtungen, Fernerkundung durch Satelliten (MODIS) und numerische Modellierung (WRF). Berlin zeigt eine UHI sowohl für Beobachtungen als auch für Simulationen. Aktuelle Landnutzungsdaten können dazu beitragen, die Modelleistung in der Simulation der UHI besonders in den ländlichen Bereichen zu verbessern. Die Urbanisierung vergrößert die räumliche Ausdehnung der UHI, wobei sich die Intensität der mit WRF modellieren UHI nicht erhöht. Die MODIS LST zeigt eine hohe positive Korrelation mit den regionalisierten ISA mit Hilfe eines Kerndichteschätzers (ISA_{KDE}). Die geradlinigen Funktionen der LST werden mit dem ISA_{KDE} sowohl in jährlichen als auch in täglichen Skalen gut wiedergegeben. Der Anstieg der geradlinigen Funktion reproduziert die Steigerung der LST von natürlichen Oberflächen in ländlichen Bereichen zu versiegelten Oberflächen in städtischen Bereichen und wird als SUHI Intensität definiert. Die abgeleitete SUHI Intensität zeigt höhere Werte im Sommer als im Winter beziehungsweise am Tag als in der Nacht. Die simulierte 2m-Lufttemperatur von WRF/UCM (T_{2m}) zeigt eine gute Beziehung mit den ISA im WRF-Gitter (ISA_{WRF}). Ähnlich wird die UHI Intensität mit dem Anstieg der ISAWRF-basierten geradlinigen Funktionen der simulierten T_{2m} gemessen. Die abgeleitete UHI Intensität zeigt U-förmige tägliche Schwankungen mit großen Werten in der Nacht. Die UHI Tagesintensität ist niedrig und wegen des Schattenwurfs der Gebäude sogar negativ. Die UHI und die städtische Verschmutzungsinsel (UPI) können einander beeinflussen. Die UHI kann die turbulente Streuung von Aerosolpartikeln fördern oder den städtisch-ländlichen Unterschied in oberflächennahen Aerosolkonzentrationen vermindern. Städtische Aerosole können die Strahlungsübertragung verändern. Die urbanen Gebiete erhalten weniger direkte

Sonneneinstrahlung und mehr langwellige atmosphärische Strahlung aufgrund der höheren Konzentration von Aerosolen. Die verminderte eingehende Solarstrahlung in der Stadt wird durch das niedrigere Reflexionsvermögen der städtischen Oberflächen teilweise ersetzt. Außerdem ist die Empfindlichkeit der Oberfläche zur Änderung der absorbierten Energie nachts stark und während des Tages schwach. Infolgedessen wird die Oberflächen-UHI durch den städtisch-ländlichen Unterschied der einfallenden Strahlung nachts erhöht, während die Veränderungen tagsüber unwesentlich sind. Die Studienergebnisse sollen zu einem besseren Verstehen des städtischen Klimas in Berlin beitragen und nützliche Auskunft geben, um UHI Mitigationsstrategien und nachhaltige städtische Planung für Berlin zu gestalten.

Chapter 1

Introduction

1.1 Research background

Cities are the centers of human activities. In the past century, the earth went through the fastest urbanization process in history. Nowadays, more than half of the world's population (54%) lives in urban areas (United Nations 2015). Fast urbanization and urban population growth are still undergoing, especially in the developing regions. It is predicted that until the mid of 21st century, around 66% of the global population will live in cities. Intensive human activities during urbanization produce special urban climate, which is characterized by the Urban Heat Island (UHI) (e.g. Zhou et al. 2004; AAAS 2016).

Urban climate is closely related to the daily lives of urban residents (Lee 1984; Souch and Grimmond 2006; Yow 2007). With the improvement of living conditions, people show higher expectation and more considerations for their living and working environment (Hartig and Kahn 2016). Urban climate has become an important influencing factor for the livability and sustainable development of a city (e.g. Wu 2014; Baklanov et al. 2016; Marin 2017). In order to create a better living environment and face global warming, some cities have made targets to create climate-friendly (Dhakal 2008) and climate-smart cities (Chapman et al. 2015; http://www.climatesmartcities.org/). UHI is the most important characteristic of urban climate and aggravates urban thermal environment (Georgescu 2015). Moreover, climate change further increases the frequency and intensity of heat waves (e.g. Meehl and Tebaldi 2004). Urban residents are suffering from more heat stress (Ward et al. 2016). A comprehensive understanding of UHI can help to efficiently evaluate the potential heat risk and to design mitigation strategies, which are crucial for city management and sustainable development (Grimmond et al. 2010; Baklanov et al. 2018). The study of UHI has received wide attention

in recent years (Santamouris 2007; Grimm et al. 2008; Inouye 2015; McDonnell and MacGregor-Fors 2016).

1.2 The definition of UHI

UHI refers to the higher temperatures in urban areas than in surrounding rural areas (Figure 1). UHI was firstly found by Howard in London (Mills 2008). Since then, the observations of UHI were widely reported in different cities all over the world (e.g. Arnfield 2003; Roth 2007; Rizwan et al. 2008).

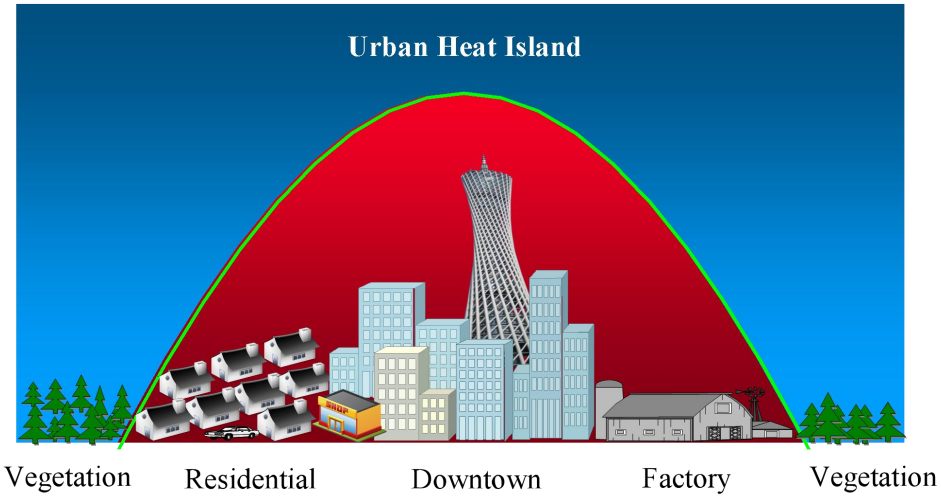

Figure 1. The diagram of urban heat island.

According to the location of study objects, there are three kinds of UHI, including canopy UHI, boundary layer UHI, and surface UHI (Oke 1982). The canopy UHI and boundary layer UHI refer to the warmer air temperature in urban areas below and above the city canopy, respectively (Oke 1976). The surface UHI refers to the warmer urban surface temperature. Most of the previous studies are about canopy UHI and surface UHI. Usually, the default UHI refers to canopy UHI and the surface UHI is represented as SUHI. The UHI varies largely with the cities all over the world (Figure 2). Even the small town with 1000 inhabitants can show a UHI, with the intensity of 1 K (Oke 1973). In big cities, the UHI intensity can reach to 10 K under optimum conditions (Oke 1982).

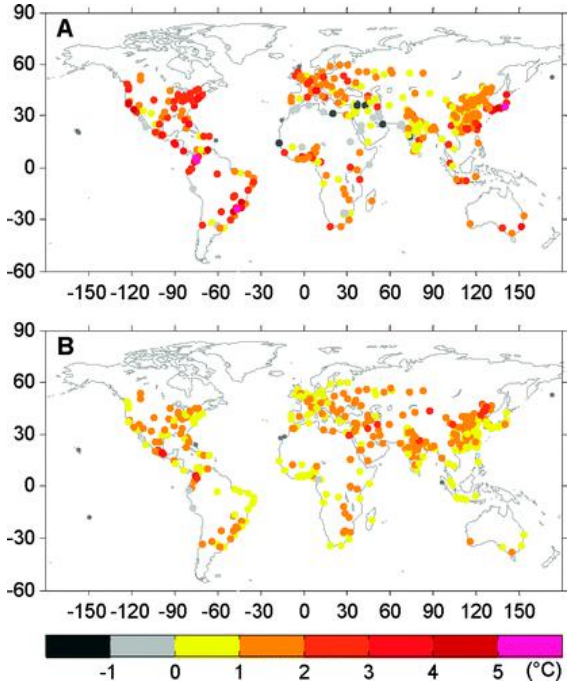

Figure 2. Spatial distribution of (A) annual mean daytime SUHII and (B) annual mean nighttime SUHII averaged over the period 2003-2008 across 419 global big cities (after Peng et al. 2011).

1.3 The impact of UHI

UHI-induced warmer temperature increases the heat load to city dwellers and consequently raises a series of negative problems on hot days, involving energy demand, air quality, and human health.

1.3.1 Increasing building's energy demand

Elevated temperature in summer increases the energy demand for air conditioners and other cooling equipment in the buildings (Shahmohamadi et al. 2010; Kolokotroni et al. 2012). Akbari (2005) found that the increase in air temperature from UHI is responsible for 5 to 10% of urban peak electricity demand for air-conditioning in the United States. During extreme heat events, too much demand for cooling may overload electricity systems.

1.3.2 Reducing air quality

Higher temperature can directly accelerate the photochemical reaction in the atmosphere, increasing the concentration of ground-level ozone and smog (Rosenfeld 1998). Additional, in

order to meet the demands of electricity used for cooling, power plants will increase the consumption of fossil fuels, indirectly leading to higher emissions of air pollution and greenhouse gases. It is found that the increase in air temperature was responsible for 20% of smog concentrations in urban areas in the United States (Akbari 2005). In the United Kingdom, it is predicted that CO_2 emissions will increase by 15% in the urban areas compared to rural areas in 2050 due to more use of the cooling system (Kolokotroni et al. 2012).

1.3.3 Threatening human health

UHI strengthens the heat waves in urban areas (e.g. Tan et al. 2010). Higher temperature decreases the human thermal comfort, which has a negative effect on human health. People living in urban areas suffer from more heat stress (e.g. Constantinescu et al. 2016) and a higher risk of heat-related disease and mortality (e.g. Kovats and Hajat 2008; Gabriel and Endlicher 2011; Burke et al. 2018). In addition, higher air pollution concentrations associated with UHI can also threaten human health.

1.4 The physical mechanism of UHI

Urbanization is the major reason for the formation of UHI (Xie et al. 2010). Land use change during the urbanization process alters surface physical properties, generating lower albedo, lower water availability, and larger heat capacity of the urban surface (Oke 1988a). The difference in the surface energy balance between urban areas and rural areas results in UHI (Oke 1982; 1988a). Additionally, the consumption of fossil fuels emits anthropogenic heat into the atmosphere, which also contributes to UHI (Taha 1997).

1.4.1 The energetic basis of UHI

The energy balance on the urban surface is as follows

$$R_n = R_S(1-\alpha) + L_{A\_D} - L_S = SH + LE + Q_s + Q_{AH} \quad (1)$$

where R_n is the net radiation of the urban surface; R_S is the incoming solar radiation; a is the surface albedo; L_{A_D} is the incoming atmospheric longwave radiation; L_s is the upward

longwave radiation emitted by the urban surface; SH is the sensible heat flux; LE is the latent heat flux; Q_s is the stored heat on the urban surface; Q_{AH} is the anthropogenic heat emissions.

UHI is mainly determined by the urban-rural difference in the surface energy balance. Figure 3 shows the radiation transfer processes and energy budget of the urban and rural surface. During the day, urban surface absorbs more energy, due to lower albedo. Most of the absorbed energy in urban areas is allocated to SH. LE for evapotranspiration is much smaller than SH in the urban areas, due to the lower water availability and higher sealing. Meanwhile, more heat is stored in the urban surface with larger Q_s than in the rural surface, because of the larger heat capacity of buildings and other artificial materials. At night, Q_s becomes the energy source of the surface. The larger Q_s from urban build-up surface releases amounts of heat into the urban canopy and decrease the cooling process in urban areas. On the contrary, the rural surface cools down fast, due to limited storage heat. The UHI is usually strong at night and reaches the maximum a few hours (typically 3 to 5 h) later after sunset (Oke and Maxwell 1975). Q_{AH} is an additional heat input to the energy balance on the urban surface and can contribute to UHI in both day and night.

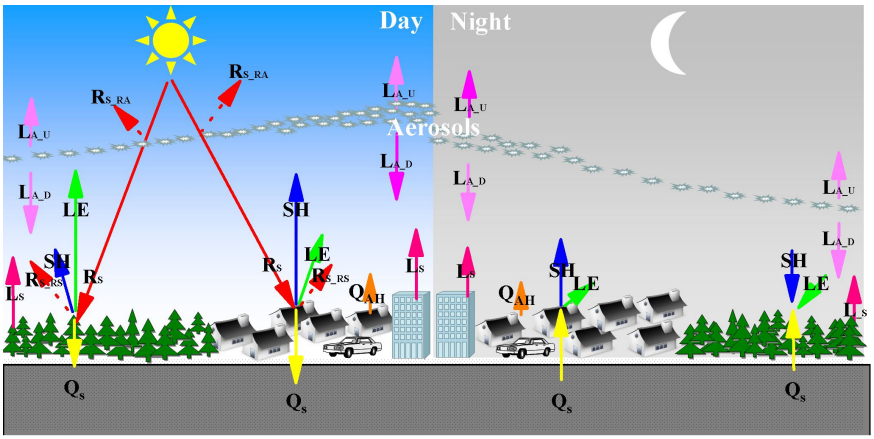

Figure 3. Radiation transfer processes and energy budget of the urban and rural surface. The arrows and lengths of the lines represent the direction of energy transfer and the magnitude of the energy components, respectively.

1.4.2 The attributions of UHI intensity

Zhao et al. (2014) developed an attribution method to quantitatively separate the contributions to SUHI intensity (SUHII) based on the energy balance analysis. The urban-rural difference of

the surface temperature, namely SUHII, is determined by five biophysical drivers as follows

$$SUHII \approx \frac{\lambda_0}{1+f}\Delta R_n + \frac{-\lambda_0}{(1+f)^2}(R_n - Q_s + Q_{AH})\Delta f_1 + \frac{-\lambda_0}{(1+f)^2}(R_n - Q_s + Q_{AH})\Delta f_2 + \frac{-\lambda_0}{1+f}\Delta Q_s + \frac{-\lambda_0}{1+f}\Delta Q_{AH} \quad (2)$$

where Δ represents the urban-rural difference; λ_0 is the local climate sensitivity; f is the energy redistribution factor; Δf_1 and Δf_2 are the change of f related to the change in surface roughness and Bowen ratio, respectively. The terms on the right side of Equation 2 represent the contributions associated with the urban-rural difference in radiation balance (term 1), aerodynamic resistance to sensible heat flux (term 2), Bowen ratio (term 3), heat storage (term 4) and anthropogenic heat emissions (term 5).

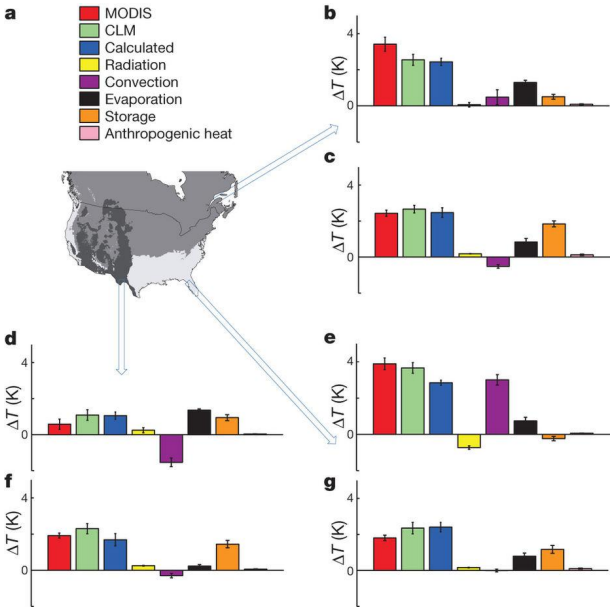

Figure 4. Attributions of SUHI intensity in three climate zones. (a) Map of climate zones: (white) mild temperate; (grey) continental; (dark grey) dry climate. (b), (d), and (e) show daytime values; (c), (f), and (g) show nighttime values (after Zhao et al. 2014).

Zhao et al. (2014) and Cao et al. (2016) evaluated the SUHII derived from attribution method against those derived from MODIS data and CLM modelling data and found reasonable agreement between them in North America and China, respectively. Zhao et al. (2014) found that the reduction of evaporation due to lower water availability (term 2) and the change of sensible heat convection due to the urban-rural difference in the roughness (term 3)

are the dominant drivers of the daytime SUHII and the change in the release of the stored heat (term 4) is the dominant contributor to the nighttime SUHII (Figure 4).

1.5 The influencing factors of UHI

1.5.1 Urbanization

Urbanization is the direct reason for UHI (e.g. Phelan et al. 2015; Zhou et al. 2016). Urbanization degree can be represented by several indicators, including population (Oke 1973;1982) and city size (e.g. Peng et al. 2011; Zhou et al. 2017). Oke (1973; 1982) found that UHI intensity is closely related to the logarithm of the population (Figure 5). Land use change is the most important form of urbanization. The near-surface temperatures rise along with the surface changing from natural to urban. The near-surface temperature usually shows a positive relationship with urban indicators, such as Impervious Surface Area (Yuan and Bauer 2007, Li et al. 2018a) and Urban Fraction (Hu et al. 2016; Li et al. 2017), while a negative relationship with vegetation indicators, such as Normalized Difference Vegetation Index (Yuan and Bauer 2007).

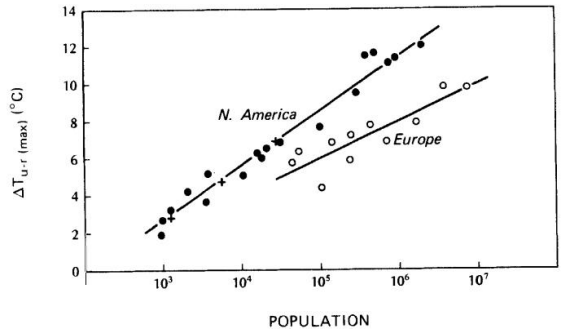

Figure 5. The relation between maximum urban heat island intensity and population for European and North American settlements (after Oke et al. 1982).

1.5.2 Regional climate

Regional climate determines the local biomass characterized by natural vegetation (Scheffers et al. 2016). Usually, the humid climate zone is characterized by forests, while the arid climate zone is characterized by sparse grassland and even bare soil. Generally, the urban-rural difference of near-surface temperature is large in humid regions, showing strong UHI, compared to that in the arid regions (e.g. Imhoff et al. 2010; Zhao et al. 2014). For the cities

in desert environments, the UHI becomes weak and even negative. Zhang et al. (2010) found that the near-surface temperature presents a 'U-shaped' horizontal gradient from rural to urban areas. Rasul et al. (2015) reported a cool island during the dry season in Erbil, Iraqi Kurdistan.

1.5.3 Urban morphology

Urban morphology includes the size and orientation of the buildings and streets (Moudon 1997). Buildings can affect the radiation transfer within the urban canopy by changing the sky view factor (Oke 1982; Arnfield 1990; Chaapman et al. 2001). Buildings shade the ground, decreasing the received solar radiation. In cities with dense tall buildings, urban areas are even cooler than the rural areas during the day, due to the significant shading of the buildings (Runnalls and Oke 2000; Yang et al. 2017). On the other hand, buildings can trap the longwave radiation emitted from the ground, decreasing the energy loss and enhancing UHI (Oke 1981; Unger 2004).

Standing buildings also change the roughness of urban canopy (Ashie et al. 1999). The convection efficiency of sensible heat is changed on the urban surface through changing the aerodynamic resistance. Zhao et al. (2014) found that urbanization reduced the convection efficiency by 58% in humid climate zone, but increased the convection efficiency by about 20% in arid climate zone. Additionally, the orientation of the buildings and streets can affect the airflow within the street (Oke 1988b). Wind channel paralleling to the prevailing wind can contribute to the advection of excess heat within the canopy and weaken UHI.

1.5.4 Synoptic conditions

Cloud and wind are taken as the most important influencing weather conditions of UHI (e.g. Oke 1982; Arnfield 2003; Rizwan et al. 2008). Clouds can affect radiation transfer processes, and wind can affect the advection and convection of the air. Clear skies and calm wind are the optimum weather conditions for UHI. Oke (1998) came up with a new definition of 'weather factor' by combining clouds and wind. Runnalls and Oke (2000) found the weather factor was linearly related to the maximum UHI magnitude. Increases in the amount of clouds and the frequency of strong wind speeds could result in a statistically significant reduction of UHI magnitude (Morris and Simmonds 2001).

1.5.5 Anthropogenic heat emissions

Anthropogenic heat released from buildings, vehicles, and human metabolic adds extra heat to the air, which increases the near-surface temperature in urban areas and then enhances UHI (Taha 1997; Feng et al. 2012). Cities usually show the hotspot of anthropogenic heat emission, compared to rural areas (Figure 6). Ichinose et al. (1999) found that the peaks of high-temperature appeared around the areas with the largest anthropogenic heat emissions in Tokyo. Dong et al. (2017) developed a global anthropogenic heat flux database and reported the highest anthropogenic heat emissions of 493 W/m^2 for Hong Kong, 353 W/m^2 for Singapore, 297 W/m^2 for New York, 188 W/m^2 for Portland, 185 W/m^2 for Macau, 175 W/m^2 for Seoul, 147 W/m^2 for Pusan, 147 W/m^2 for Montreal, 141 W/m^2 for Chicago, and 141 W/m^2 for Tokyo. The influence of anthropogenic heat on UHI was relatively large in winter, as the shortwave radiation was weak (Ichinose et al. 1999). Anthropogenic heat emission is affected by the intensity of human activity, which is related to population density.

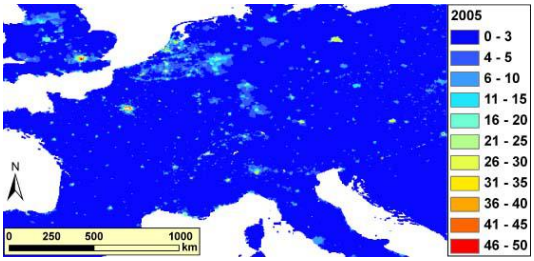

Figure 6. Annual average anthropogenic heat emission (W/m^2) across Central Europe in 2005 (after Allen et al. 2011).

1.5.6 Air pollutants

Air pollutants, especially aerosols, can affect radiation transfer. On one hand, aerosols can scatter solar radiation back into space, consequently decreasing the solar radiation to the ground (Navarro et al. 2016). On the other hand, the aerosols can absorb the longwave radiation emitted by the surface, and some aerosol particles, such as black carbon, can absorb solar radiation (e.g. Gatari and Boman, 2003; Ramanathan and Carmichael, 2008), heating the atmosphere and re-emitting more downward longwave radiation (e.g. Pueschel and Kuhn 1975; Vogelmann et al. 2003). Urban areas are usually shaded by more aerosols, due to anthropogenic emissions (e.g. Zhou et al. 1991; Crutzen 2004). Dense urban aerosols scatter

more solar radiation and re-emit more longwave radiation to the urban surface. As a result, urban areas receive less solar radiation and more atmospheric longwave radiation (Peterson and Stoffel 1980; Jauregui and Luyando 1999). The urban-rural difference in the incoming radiation will affect the urban-rural difference in the energy balance, consequently changing UHI (Cao et al. 2016).

1.6 Study methodology of UHI

Currently, field measurement, remote sensing, and numerical modelling are the most used approaches for the study of UHI (Mirzaei and Haghighat 2010). Each of these methods has both advantage and disadvantage.

1.6.1 Field observation

Field observation of UHI includes in-situ and mobile observations. The in-situ observation is usually conducted at paired stations in urban and rural areas, respectively (Wang et al. 1990; Stone 2007). In-situ stations are convenient for long-term observations. Robust in-situ data can be used to analyze UHI and to evaluate modelling results. However, the lack of observation stations is frequently encountered problems. The urban surface is inhomogeneous, with large variation in the near-surface temperature. The sparse stations cannot reflect the spatial pattern and the detailed characteristic of UHI (Oke 2006). In order to overcome this problem, some urban climate observation networks were established across the world. In Berlin, there is an urban climate measurement network consisting of 54 stations (http://www.geo.fu-berlin.de/en/met/service/stadtmessnetz/index.html). In the city of Madison, USA, more than 130 temperature data loggers were installed across the city (Schatz and Kucharik 2014). In Shanghai of China, an Urban Integrated Meteorological Observation Network (SUIMON) was established (Tan et al. 2015). Meanwhile, some collaborative, multi-institutional, multi-national and interdisciplinary initiatives urban climate observational programs were established (Grimmond 2006; Christen 2009). URBANFLUXES project includes three observation networks in Heraklion, Basel, and London (http://urbanfluxes.eu/data/). International Association for Urban Climate also established an urban flux database to collect and share the data of the micrometeorological tower in the

mega-cities all over the world (http://ibis.geog.ubc.ca/urbanflux/). Intensive observation stations help to obtain robust data to study the spatial variation of UHI, but cost a lot of money for the equipment.

Mobile observation is an important complement to the observation of UHI profile (Oke 1972; Leconte et al. 2015). Mobile observation is usually conducted through the equipment that is installed on cars or bicycles. Mobile carrier is more flexible, compared to fixed stations. However, mobile observation needs a manual operation, which is time-consuming and is not convenient for long-term operation.

1.6.2 Remote sensing observation

With the development of satellite technique, remote sensing has been widely used in the study of UHI (Voogt and Oke 2003). Remote sensing can be used to monitor UHI at city scale (Cheval et al. 2015; Azevedo et al. 2016), regional scale (Zhao et al. 2014; Cao et al. 2016), as well as global scale (Zhang et al. 2010; Peng et al. 2011). Currently, MODIS and Landsat are the two most popular remote sensing datasets. Both of them are easy to access at a large scale. Robust remote sensing data make the comparison study of UHI across different regions convenient. The influencing factors of UHI, such as city size (e.g. Peng et al. 2011; Zhou et al. 2017) and biomass (e.g. Imhoff et al. 2010; Zhang et al. 2010), were examined, through a comparison study of UHI in multi-cities.

However, there is a trade-off between spatial and temporal resolutions of remote sensing datasets (Lillo-Saavedra and Gonzalo 2006; Thomas et al. 2008). For example, the MODIS data have a high temporal resolution, four times per day, but a low spatial resolution, 1000 m (Cool et al. 2009), while Landsat data have a high spatial resolution, 30 m, but a low temporal resolution, 16 days per observation (Zhang et al. 2006). Moreover, remote sensing is easy to be disturbed by clouds (Williamson et al. 2013). There are a large number of missing values. Li et al. (2018b) found that the available MODIS land surface temperature covers less than 30% of the urban areas in the conterminous United States. In addition, most of the current thermal remote sensing products are about land surface temperature. Compared to surface temperature, air temperature is more concerned in term of heat stress. However, there are little

remote sensing air temperature products available (Benali et al. 2012).

1.6.3 Numerical modelling

Numerical models can simulate UHI at both high spatial and temporal resolution (Loridan et al. 2013; San José et al. 2013) and at large spatial and temporal scales (Oleson 2008; 2011). Furthermore, numerical modelling can be conducted under different weather conditions. Numerical modelling is a powerful and convenient approach for the study of UHI (Martilli 2007; Mirzaei and Haghighat 2010). With the development of numerical modelling, urban climatology has already become a more predictive science. Numerical modelling has been widely used for the investigation of the physical mechanism and drivers of UHI (e.g. Rizwan et al. 2008; Hidalgo et al. 2008; Chen et al. 2012), the pre-warning of heat waves (e.g. Zauri et al. 2010; Wang and Li 2016), the simulation of future scenarios (e.g. Kusaka et al. 2012; Hamdi et al. 2014), and the evaluation of mitigation strategies (e.g. Salamanca et al. 2008; Zhou and Shepherd 2010). A large number of numerical models were developed, such as WRF/UCM (Chen et al. 2011), COSMO/CLM (Schubert and Grossman-Clarke 2014), and MUKLIMO (Min et al. 2005).

Urban surface processes are parameterized in different levels of complexity in numerical models (Martilli 2007). Take the WRF/urban modelling system as an example (Chen et al. 2011). This system provides three urban parameterization schemes with different degrees of freedom, including bulk approach, single layer urban canopy module (SLUCM) and multi-layer urban canopy module (BEP) (Figure 7). Bulk urban parameterization is simple and only considers the zero-order effects of urban surfaces using some urban parameters. SLUCM considers the shadowing, reflections, and trapping of radiation, surface energy budget of roofs, walls and roads, canyon drag, and anthropogenic heat emissions in the street canopy. BEP is the most sophisticated and further recognizes three-dimensional urban surfaces. BEP considers the effects of vertical (walls) and horizontal (streets and roofs) surfaces on the momentum, turbulent kinetic energy, and potential temperature.

Urban surface processes are complicated and include numerous sub-processes. Current urban parameterization schemes cannot consider all of the sub-processes in detail, due to the

limitation of computing resources and the insufficient understanding of urban surface processes in theory (Mirzaei 2015). There are many urban parameters in the models, which can largely affect the simulation results. The users must update these parameters for a new city using different urban datasets, which is full of challenges and costs a lot of time (Martilli 2007; Chen et al. 2011). In addition, some models applied coarse urban land cover classification with few urban land cover types. The urban surface has high heterogeneity. The limited types of urban land cover data may fail to represent real urban surface and generate simulation errors.

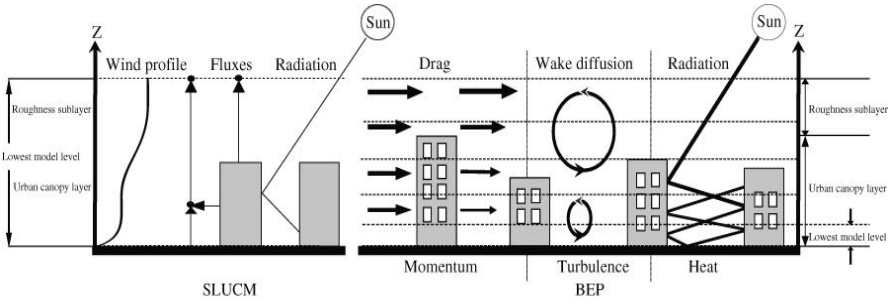

Figure 7. A schematic of the SLUCM (on the left-hand side) and the multi-layer BEP models (on the right-hand side) in the WRF model (after Chen et al. 2011).

1.7 The urban climate in Berlin

The study was conducted in Berlin, the capital city of Germany. Berlin covers an area of around 900 km^2 and has more than 3.6 million inhabitants. It is the largest city in Germany and the second populous city in the European Union. Berlin has a large fraction of built-up areas and paving areas. Most of the non-urban areas are covered by forest and farmland. The large build-up areas and paving areas create a distinct UHI (Li et al. 2017; 2018a). Berlin suffers from high heat risk, especially in central inner-city areas with dense residential uses (Dugord et al. 2014).

The local people in Berlin, especially old people, are sensitive to hot weather, due to limited cooling equipment. The UHI-enhanced heat wave has a negative impact on the human health of the Berlin dweller (Gabriel and Endlicher 2011). Every year between 2001 and 2010, there are about 1600 excess deaths related to heat-stress risk in Berlin, accounting for about 5 % of all deaths (Scherer et al. 2014). Most of the affected people are 65 years or older.

Today, Berlin is growing and the population is rising. Berlin aims to become more competitive and attractive in Europe and even in the world. A comfortable urban climate is an important content for the sustainable development of the city. Berlin strategy clearly considers 'Laying the groundwork for a climate-friendly metropolis' as an important development principle (Urban Senate 2015). However, Berlin may face more frequent and strong heat waves in the future, under the background of climate change (Figure 9). How to adapt to the future climate change to achieve a climate-friendly target is full of challenges. The study of UHI in Berlin is becoming more important and urgent.

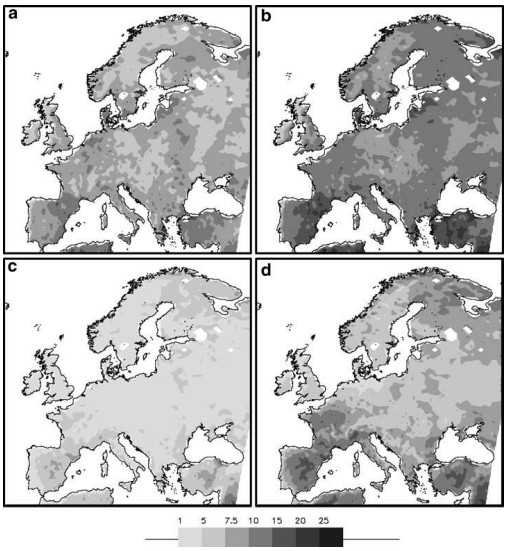

Figure 9. Changes (expressed as a ratio) in the heat wave indices (a) HWN, (b) HWF, (c) HWD, and (d) HWI between the 1961–1990 and 2071–2100 periods, based on HIRHAM4 simulations. HWN: mean number of heat waves; HWF: the frequency of heat-wave days; HWD: mean duration of heat waves; HWI: mean intensity of heat wave. (after Beniston et al. 2007)

1.8 Research questions, contents, and targets

This study attempts to quantify the UHI in the city of Berlin and examine the underlying physical processes and influencing factors. Multiple approaches, including in-suite observation, remote sensing (MODIS), and numerical modelling (WRF), are used. The main research questions in this study include four aspects as follows: (1) what are the characteristics of the spatial and temporal variations of the UHI/SUHI in the city of Berlin? (2)

how does the UHI/SUHI response to the recent urbanization in the WRF simulation? (3) what is the relationship between the near-surface temperature and the imperviousness of the surface in both observations and modeling results? (4) what is the influence of urban aerosols on the UHI? In order to answer these questions, four independent studies were conducted. Each study answers one or more of the above questions. The innovations of this study include three aspects as follows: (1) multi-source data and multi-methods were used to analyze the spatial and temporal variations of UHI/SUHI at different scale; (2) a new method based on the relationship between temperature and ISA to calculate UHI/SUHI intensity was proposed; and (3) the influence of urban pollution on UHI was quantified using an attribution method.

The detailed descriptions of the research contents, methodology, and the targets of the four studies refer to the papers in the appendix. The brief descriptions of them are shown below.

1.8.1 Impact of land cover data on the simulation of UHI using WRF/Noah-LSM

Urbanization-induced urban-rural difference of land cover is the key determinant of UHI (e.g. Phelan et al. 2015; Zhou et al. 2016). Previous studies reported that the UHI intensity showed a close relationship with urban size (e.g. Oke 1973; 1982; Zhou et al. 2017). Current default land cover data for WRF modelling is the US Geological Survey (USGS) data, which is old and can not reflect the real UHI. In order to evaluate the impact of land cover data on the simulation of UHI, a comparative study between up-to-date CORINE land cover (CLC) and Urban Atlas (UA) with fine resolution (100 and 10 m) and old USGS data with coarse resolution (30 s) was conducted using the WRF coupled with bulk approach of Noah-LSM for Berlin. The comparison between old data and new data partly reveals the effect of urbanization on UHI and the historical evolution of UHI. Meanwhile, the comparison between different resolution data reveals the impact of the resolution of land cover on the simulation of UHI. The simulation results were evaluated against in-situ measured air temperature and remotely sensed land surface temperature. The UHI of both air temperature and land surface temperature were analyzed. The UHI curve (UHIC) was developed based on the relationship between temperature and urban fraction. The simulated surface energy balance using the three land cover data was compared. The target of the study is to (1) investigate the spatial and

temporal variation of the UHI in Berlin, (2) examine the impact of different land cover on the simulation of UHI, which could show the response of UHI to urbanization, and (3) reveal the physical mechanism that controls the UHI in the model.

1.8.2 Quantifying SUHI intensity using remote sensing

Reliable quantification of UHI intensity can contribute to the effective evaluation of potential heat risk. Traditional methods for the quantification of UHI intensity using pairs-measurements are sensitive to the choice of stations or grids (Schwarz et al. 2011). Previous studies found that near-surface temperatures were closely related to impervious surface areas (ISA) (e.g. Yuan and Marvin 2007; Rajasekar and Weng 2009). As a good indicator of urban land use, ISA dominates the spatial pattern of UHI/SUHI. Imhoff et al. (2010) found that ISA explained 70% of the total variance in LST for 38 the most populous cities combined in the continental United States. The relationship between temperature and ISA can be a potentially powerful tool for the quantification of UHII/SUHII. This study proposes a new approach to quantify SUHI intensity based on the good relationship between remote sensing LST and ISA. Given the footprint of LST measurement, the ISA was regionalized to include the information of neighborhood pixels through a Kernel Density Estimation (KDE) method. The linear regression function of LST was fitted using the KDE-regionalized ISA (ISA_{KDE}). The regression slope of the fitted function was used as SUHI intensity. The temporal variations of the calculated SUHI intensity of Berlin in 2010 were investigated. The target of this paper is to (1) investigate the relationship between MODIS LST and ISA in Berlin, (2) develop a promising approach for the quantification of SUHI intensity, and (3) investigate the spatial and temporal variation of SUHI intensity in Berlin.

1.8.3 Quantifying UHI intensity using WRF/UCM

Numerical modelling is a powerful and convenient approach for the study of UHI (Martilli, 2007; Mirzaei, 2015) and has been widely used in different aspects of UHI. However, accurate quantification of UHII using modelling grid data is still a challenge at present, although robust data are available from numerical modelling. The ISA-based function of the

near-surface temperature provides a promising new method to quantify UHII using grid data. However, there is no study about the application and evaluation of this new method in quantifying UHII using modelling grid data at present. This study attempts to quantify UHII by applying the new method and the modelling data of WRF/UCM, which is a popular numerical model for the study of urban climate. The UCM considers the imperviousness in three categories of urban land cover and the mosaic approach of Noah LSM scheme of WRF distinguishes sub-grid land cover categories (Li et al., 2014), making the calculation of ISA in WRF grids (ISA_{WRF}) convenient. In this study, the high-resolution UHI during a clear-sky and calm-wind period in the city of Berlin was simulated. The weighted sum of the fractions of UCM-used three categories of urban land cover and their corresponding imperviousness in each WRF grid was calculated as ISA_{WRF}. The relationship between the simulated air temperature and ISA_{WRF} was analyzed for different time periods of the day. The linear functions of the simulated air temperature were fitted using ISA_{WRF}. The slope of the fitted function was used to calculate UHII. The temporal variation of the derived UHII was investigated. A comparison between the derived UHII using the new method and those using traditional methods was conducted. The physical mechanism that controlled the derived UHII in the WRF/UCM was discussed. The target of this study is to (1) evaluate the accuracy of WRF/UCM in simulating the UHI in the city of Berlin, (2) investigate the spatial and temporal variations of the simulated UHI, (3) evaluate the feasibility of the ISA_{WRF}-based functions of the simulated air temperature in quantifying UHII, and (4) examine the physical mechanism that controls the derived UHII.

1.8.4 Interaction between UHI and urban pollution island

UHI and Urban Pollution Island (UPI) are two major problems of the urban environment in large cities and have become more serious with rapid urbanization. Since UHI and UPI can interact with each other, these two issues should be studied concurrently for a better urban environment. The interactive impacts of growing UHI and UPI are becoming a new research field (Crutzen, 2004). However, most of the previous studies on UHI and UPI were conducted separately. Insufficient knowledge of the interaction between UHI and UPI inhibits the development of integrative mitigation strategies. In this study, we attempted to connect UHI

and UPI and carried out an integrated study of these two problems in the city of Berlin. In-situ and remote sensing observations of aerosols and meteorological variables in June, July, and August from 2010 to 2017 were collected. The atmospheric UPI (AUPI), near-surface UPI (NSUPI), atmospheric UHI (AUHI), and surface UHI (SUHI) were analyzed. The AUPI describes the urban-rural difference of the aerosol optical depth (AOD) from remote sensing observation, and the NSUPI describes the urban-rural difference of the near-surface aerosol concentrations characterized by the in-situ observations of Particulate Matter (PM10). The AUHI describes the urban-rural difference of the air temperature from in-situ observation, and the SUHI describes the urban-rural difference of the LST from remote sensing observation. The study consists of three sections. Firstly, the relationship between the SUHI and AUPI in spatial variations was investigated using remote sensing data. Secondly, the impact of the AUHI on the NSUPI was examined using in-situ observations. Thirdly, the impact of the AUPI on the radiation transfer was studied by comparing the incoming solar radiation and atmospheric longwave radiation between the urban and rural areas. Moreover, the response of the SUHI to the urban-rural difference of the absorbed radiation was analyzed using an attribution method (Cao et al., 2016). The target of this study is to (1) improve the understanding of the interactive influence between urban thermal environment and air pollution, (2) discuss the potential physical mechanism of the interaction, and (3) provide a scientific basis for the mitigation of these two problems.

Chapter 2

Impact of land cover data on the simulation of urban heat island for Berlin using WRF coupled with bulk approach of Noah-LSM

Abstract Urban-rural difference of land cover is the key determinant of urban heat island (UHI). In order to evaluate the impact of land cover data on the simulation of UHI, a comparative study between up-to-date CORINE land cover (CLC) and Urban Atlas (UA) with fine resolution (100 and 10 m) and old US Geological Survey (USGS) data with coarse resolution (30 s) was conducted using the Weather Research and Forecasting model (WRF) coupled with bulk approach of Noah-LSM for Berlin. The comparison between old data and new data partly reveals the effect of urbanization on UHI and the historical evolution of UHI, while the comparison between different resolution data reveals the impact of the resolution of land cover on the simulation of UHI. Given the high heterogeneity of urban surface and the fine-resolution land cover data, the mosaic approach was implemented in this study to calculate the sub-grid variability in land cover compositions. Results showed that the simulations using UA and CLC data perform better than that using USGS data for both air and land surface temperatures. USGS-based simulation underestimates the temperature, especially in rural areas. The longitudinal variations of both temperature and land surface temperature show good agreement with urban fraction for all the three simulations. In order to better study the comprehensive characteristic of UHI over Berlin, the UHI curves (UHIC) are developed for all the three simulations based on the relationship between temperature and urban fraction. CLC- and UA-based simulations show smoother UHICs than USGS-based simulation. The simulation with old USGS data obviously underestimates the extent of UHI, while the up-to-date CLC and UA data better reflect the real urbanization and simulate the spatial

distribution of UHI more accurately. However, the intensity of UHI simulated by CLC and UA data is not higher than that simulated by USGS data. The simulated air temperature is not dominated by the land cover as much as the land surface temperature, as air temperature is also affected by air advection.

Chapter 3

A new method to quantify surface urban heat island intensity

Abstract Reliable quantification of urban heat island (UHI) can contribute to the effective evaluation of potential heat risk. Traditional methods for the quantification of UHI intensity (UHII) using pairs-measurements are sensitive to the choice of stations or grids. In order to get rid of the limitation of urban/rural divisions, this paper proposes a new approach to quantify surface UHII (SUHII) using the relationship between MODIS land surface temperature (LST) and impervious surface areas (ISA). Given the footprint of LST measurement, the ISA was regionalized to include the information of neighborhood pixels using a Kernel Density Estimation (KDE) method. Considering the footprint improves the LST-ISA relationship. The LST shows a highly positive correlation with the KDE regionalized ISA (ISA_{KDE}). The linear functions of LST are well fitted by the ISA_{KDE} in both annual and daily scales for the city of Berlin. The slope of the linear function represents the increase in LST from the natural surface in rural regions to the impervious surface in urban regions, and is defined as SUHII in this study. The calculated SUHII show high values in summer and during the day than in winter and at night. The new method is also verified using finer resolution Landsat data, and the results further prove its reliability.

Chapter 4

Quantifying Urban Heat Island Intensity and its Physical Mechanism Using WRF/UCM

Abstract Reliable quantification of urban heat island intensity (UHII) is crucial for the evaluation of extreme heat waves and the related heat stress. As a powerful approach for the study of urban climate, numerical models can simulate urban heat island (UHI) in both high spatial and temporal resolutions. However, accurate quantification of UHII using modelling grid data is still a challenge at present, due the different criterions for the selection of urban/rural grids. This study simulates the high-resolution UHI in the city of Berlin using the Weather Research and Forecasting Model coupled with Urban Canopy Module. A new method to quantify UHII, which is based on the fitted linear functions of simulated 2-m air temperature (T_{2m}) using the impervious surface area in WRF grids (ISA_{WRF}), was adopted and evaluated. The simulated T_{2m} matches the observations well, with a correlation coefficient of 0.95 (P<0.01) and RMSE of 1.76 °C. The study area shows a strong UHI at nighttime. The simulated nighttime T_{2m} increases with the increase in the ISA_{WRF}. The linear functions of simulated nighttime T_{2m} against ISA_{WRF} are well fitted. The UHII is calculated as the products of the slopes of fitted functions and the largest ISA_{WRF}. The derived UHII shows U-shaped diurnal variations, with high values at nighttime. The difference of simulated surface temperature and sensible heat flux between the impervious surface and the vegetation surface jointly determines the derived UHII. The large difference of surface temperature and the small difference of sensible heat flux between the impervious and the vegetation surface generate the high UHII at nighttime and vice versa during the daytime. The method of ISA_{WRF}-based function of T_{2m} overcomes the problems of traditional methods in arbitrary selecting urban/rural grids. It can be used easily to quantify UHII and to do the comparison study of UHII between different cities.

Chapter 5

Interaction between Urban Heat Island and Urban Pollution Island during summer in Berlin

Abstract Urban Heat Island (UHI) and Urban Pollution Island (UPI) are two major problems of the urban environment and have become more serious with rapid urbanization. Since UHI and UPI can interact with each other, these two issues should be studied concurrently for a better urban environment. This study investigated the interaction between the UHI and UPI in Berlin, through a combined analysis of in-situ and remote sensing observations of aerosols and meteorological variables in June, July, and August from 2010 to 2017. The atmospheric UHI (AUHI), surface UHI (SUHI), atmospheric UPI (AUPI), and near-surface UPI (NSUPI) were analyzed. The SUHI and AUPI are represented by the remote sensing land surface temperature (LST) and aerosol optical depth (AOD), and the AUHI and NSUPI are represented by the in-situ air temperature and Particulate Matter (PM10) concentrations. The study area shows spatial consistency between SUHI and AUPI, with higher LST and AOD in the urban areas. UHI strengthens the turbulent dispersion of particles in the urban areas, decreasing the NSUPI. The NSUPI intensity shows a negative relationship with the AUHI intensity, especially at night with a correlation coefficient of -0.31. The increased aerosols in the urban atmosphere reduce the incoming solar radiation and increase the atmospheric longwave radiation in the urban areas. The response of the surface to the change of absorbed radiation is strong at night and weak during the day. This study estimates that the SUHI intensity is enhanced by around 12% at clear night by the increased absorbed radiation in the urban areas using an attribution method. The goal of this paper is to strengthen the understanding of the interactive influence between UHI and UPI and provide a basis for designing mitigation strategies of UHI and UPI.

Chapter 6

Conclusions and Outlooks

6.1 Conclusions

This study quantified the UHI in the city of Berlin and investigated the underlying physical processes and influencing factors using multiple datasets and approaches. Some meaningful results were achieved. The major findings of this study are as follows:

(1) Simulations using up-to-date land cover data (CLC and UA in 2012) performed better than the simulation using old land cover data (USGS in 1994) for both air temperature and land surface temperature. The USGS-based simulation underestimated the temperature in the rural areas. The UA- and CLC-based simulations more accurately reflected the spatial distribution of UHI, while the USGS-based simulation underestimated the extent of UHI. Generally, the updated and fine-resolution land cover data reflect the real land surface condition and are much better for the simulation of UHI. The difference between old USGS data and up-to-date CLC and UA data partly reflects the urbanization process, particularly in the surrounding developing areas. The city center is highly urbanized. The simulated temperatures in central areas were similar for all the three land cover datasets. The recent urbanization in the rural areas increased the extent of UHI in Berlin, but had little influence on the intensity of UHI based on the simulation results. The resolution of the land cover data could also affect the simulation results and the impact was related to the magnitude of the resolution itself. When the resolution of land cover data was coarse, increasing the resolution could produce better simulation results. However, when the resolution became fine enough (much better than the resolution of grids), increasing the land cover resolution may not further improve the simulation results.

(2) The study area showed spatial consistency between the MODIS LST and ISA, consistent

with the previous studies (e.g. Yuan and Marvin, 2007; Rajasekar and Weng, 2009). Considering the footprint of LST observation could improve the LST-ISA relationship. The linear functions of LST were fitted well using the KDE-regionalized ISA (ISA_{KDE}) at both the annual and daily scale. The SUHI intensity was calculated using the slope of the fitted functions. The annual mean SUHI intensity was 5.72, 5.38, 4.09 and 4.61 K at four observation times of the day. The SUHI at daytime and summer is stronger than those at nighttime and winter, consistent with the previous study in Europe (Schwarz et al. 2011). Precipitation could weaken the LST-ISA relationship and then influenced the calculation of SUHI intensity. The well-fitted linear function of LST using ISA_{KDE} provide a promising approach to quantify SUHI intensity using remote sensing data.

(3) The WRF/UCM performed reasonably well in simulating $T_{2m,}$ with the correlation coefficient of 0.95 ($P<0.01$) and the RMSE of 1.76 °C, which are consistent with the previous study in this region (Jänicke et al., 2017) and the studies in other regions (Bhati and Mohan, 2016). The simulated nighttime T_{2m} linearly increased with the increase in the ISA_{WRF}. There was a pronounced UHI at nighttime in the study area. The ISA_{WRF}-based linear functions of T_{2m} were well fitted. The derived UHI intensity showed 'U-shaped' diurnal variations, with large values at nighttime. The daytime UHI intensity was low and even negative. The differences of the simulated surface temperature (T_s) and sensible heat flux (SH) between impervious surface and vegetation surface jointly controlled the derived UHI intensity. In the nighttime, the large difference of T_s and small difference of SH between impervious surface and vegetation surface generated high nighttime UHI intensity and vice versa in the daytime. The derived UHI intensity showed a reasonable agreement with the results from traditional methods. The derived UHI intensity using the new method considers the overall T_{2m} at all the grids in the study area and is not limited to the selection of urban and rural grids. The new method is more universal, compared to traditional methods. It can be easily used for the comparison study of UHI intensity among different studies.

(4) The study area showed both SUHI and AUPI. There was a positive correlation between the spatial configurations of the SUHI and AUPI, with a coefficient of 0.62 ($p<0.01$) during the day. UHI-related warm temperature promoted the turbulent dispersion of aerosol particles in

the urban areas, decreasing the NSUPI. The NSUPI intensity showed a negative relationship with the AUHI intensity, especially at night. The increased aerosols in the urban areas reduced the incoming solar radiation and increased the atmospheric longwave radiation. The SUHI was more sensitive to the change of absorbed radiation at night than during the day. It was estimated that the SUHI was enhanced by around 12% by the increased absorbed radiation in the urban areas at clear night using an attribution method. During the day, the change of SUHI intensity caused by the change of the incoming radiation was negligible, due to the offset of the opposite change of solar radiation and atmospheric longwave radiation and the weak sensitivity of the surface. Our study reveals some insights regarding the interaction between UHI and UPI that provide starting points for urban planning authorities in order to design reasonable mitigation strategies.

6.2 Outlooks

Urban land process is pretty complicated. The physical mechanism and the influencing factors vary among cities with different urbanization process, regional climate, and the morphology of buildings. This study only focuses on the UHI in the city of Berlin at the local scale. The conclusions may not be suitable for other cities. The comparison study of UHI among multi-cities should be conducted in the future to draw more universal conclusions. In addition, there may be some uncertainties for our current study, due to the limited observations data and short-term modelling. Future study needs long-term observation and modelling.

This study quantifies the UHI and reveals the underlying physical processes and the influencing factors using the historical observations and the simulations of past times. The future scenarios of climate change and urbanization are not discussed. For a sake of better projection of future heat risk, the future scenarios should be evaluated in the next step. In addition, the current conclusions provide some inspiration for the potential mitigation strategies of UHI, such as urban greening and decreasing urban pollution. However, the mitigation effects of these strategies are not evaluated and quantified and need further studies.

Urban climatology is an interdisciplinary major, involving meteorology, ecology, environmental science, and urban and landscape planning. There are a number of

sub-processes inside a city. Our study mainly focuses on the meteorological processes and draws the conclusions in the respect to the meteorological aspect. It should be noted that the interactions between different processes exist. The changes of the meteorological process may affect other processes. For example, Fallman et al. (2016) found that the mitigation of UHI may weaken turbulence mixing, then increasing the near-surface concentrations of some pollutants. Our study also found similar phenomena. When designing mitigation strategies, we need to consider its following effects on other processes in order to achieve the best benefits of overall urban environments. Future urban climate study needs more cooperation with the scientist from other subjects and needs to consider the interactions between different processes.

Remote sensing and numerical modelling can generate grid datasets, which can be used to study UHI at large scale. Most of the current remote sensing products are land surface temperature, which is used to study surface UHI. However, canopy UHI associated with air temperature is more related to our daily lives and is more concerned by people. There is a big difference between surface UHI and canopy UHI (Schwarz et al. 2012), in spite of good relationships between them. Developing air temperature products derived from remote sensing observation signals is worth more effort for the future studies. Numerical modelling makes urban climatology become a more predictive science. However, numerical modelling is subject to the numerous urban parameters and limited urban land cover types in the model (Chen et al. 2011). The biases of the WRF simulation in urban areas are larger than in the rural areas. There is a big improvement space for the simulation accuracy. Urbanized high-resolution land data assimilation system can combine numerical modelling and observation datasets (Chen et al. 2011; Meng et al. 2013). Data assimilation technique should be a promising way to improve model performance in the simulation of UHI and can be used to develop some useful datasets for the study of urban climate.

Bibliography

Akbari H. 2005. Energy Saving Potentials and Air Quality Benefits of Urban Heat IslandMitigation. Ernest Orlando Lawrence Berkeley National Laboratory, Berkeley, CA (US).

Allen L, Lindberg F, Grimmond CSB. 2011. Global to city scale urban anthropogenic heat flux: model and variability. International Journal of Climatology, 31(13): 1990-2005.

American Association for the Advancement of Science (AAAS). 2016. Rise of the City. Science, 352: 906-907.

Arnfield AJ. 2003. Two decades of urban climate research: a review of turbulence, exchanges of energy and water, and the urban heat island. International Journal of Climatology, 23: 1-26.

Arnfield AJ. 1990. Street design and urban canyon solar access. Energy and Buildings, 14(2): 117-131.

Ashie Y, Ca VT, Asaeda T. (1999). Building canopy model for the analysis of urban climate. Journal of Wind Engineering and Industrial Aerodynamics, 81: 237-248.

Azevedo JA, Chapman L, Muller CL. 2016. Quantifying the daytime and night-time urban heat island in Birmingham, UK: A comparison of satellite derived land surface temperature and high resolution air temperature observations. Remote Sensing, 8(153), doi:10.3390/rs8020153.

Baklanov A, Grimmond CSB, Carlson D, Terblanche D, Tang X, Bouchet V, Lee B, Langendijk G, Kollia RK, Hovsepyan A. 2018. From urban meteorology, climate and environment research to integrated city services. Urban Climate, 23:330-341.

Benali A, Carvalho AC, Nunes JP, Carvalhais N, Santos A. 2014. Estimating air surface

temperature in Portugal using MODIS LST data. Remote Sens Environ 2012; 124:108-121.Dugord P A, Lauf S, Schuster C, et al. Land use patterns, temperature distribution, and potential heat stress risk–the case study Berlin, Germany. Computers, Environment and Urban Systems, 48: 86-98.

Beniston M, Stephenson DB, Christensen OB, Ferro CA, Frei C, Goyette S,Halsnaes K, Holt T, Jylhä K, Palutikof J, Schöll R, Semmler T, Woth K. 2007. Future extreme events in European climate: an exploration of regional climate model projections. Climatic change, 81(1): 71-95.

Bhati S, Mohan M. 2016. WRF model evaluation for the urban heat island assessment under varying land use/land cover and reference site conditions. Theoretical and Applied Climatology, 126: 385-400.

Burke M, González F, Baylis P, Heft-Neal S, Baysan C, Basu S, Hsiang S. 2018. Higher temperatures increase suicide rates in the United States and Mexico. Nature climate change, 8: 723–729.

Chapman L, Muller CL, Young DT, Warren EL, Grimmond CSB, Cai XM, Ferranti EJ. 2015. The Birmingham urban climate laboratory: An open meteorological test bed and challenges of the Smart City. Bulletin of the American Meteorological Society, 96(9): 1545-1560.

Chapman L, Thornes JE, Bradley AV. 2001. Rapid determination of canyon geometry parameters for use in surface radiation budgets. Theoretical and Applied Climatology, 69: 81-89.

Cao C, Lee X, Liu S, Schultz N, Xiao W, Zhang M, Zhao L. 2016. Urban heat islands in China enhanced by haze pollution. Nature Communications, 7, doi:10.1038/ncomms12509.

Chen F, Bornstein R, Grimmond S, Li J, Liang X, Martilli A, Miao S, Voogt J, WangY. 2012. Research priorities in observing and modeling urban weather and climate. Bulletin of the American Meteorological Society, 93(11): 1725-1728.

Chen F, Kusaka H, Bornstein R, Ching J, Grimmond CSB, Grossman-Clarke S, Loridan T, Manning KW, Martilli A, Miao S, Sailor D, Salamanca FP, Taha H, Tewari M, Wang X, Wyszogrodzki AA and Zhang C. 2011. The integrated WRF/urban modelling system: development, evaluation, and applications to urban environmental problems. International Journal of Climatology, 31:273-288.

Cheval S, Dumitrescu A. 2015. The summer surface urban heat island of Bucharest (Romania) retrieved from MODIS images. Theoretical and Applied Climatology, 121: 631-640.

Christen A, Grimmond S, Roth M, Pardyjak E. 2009. The IAUC Urban Flux Network-An international network of micrometeorological flux towers in urban ecosystems. In AGU Fall Meeting Abstracts.

Coll C, Wan Z, Galve JM. 2009. Temperature-based and radiance-based validations of the V5 MODIS land surface temperature product. Journal of Geophysical Research, Atmosphere, 114(20).

Constantinescu D, Cheval S, Caracaş G, Dumitrescu A. 2016. Effective monitoring and warning of Urban Heat Island effect on the indoor thermal risk in Bucharest (Romania). Energy and Building, 127: 452-468.

Crutzen P. 2004. New Directions: The growing urban heat and pollution island effect-impact on chemistry and climate. Atmospheric Environment, 38(21): 3539-3540.

Dhakal S. 2008. Climate change and cities: The making of a climate friendly future. In Urban Energy Transition, pp. 173-192.

Dong Y, Varquez ACG, Kanda M. 2017. Global anthropogenic heat flux database with high spatial resolution. Atmospheric Environment, 150:276-294.

Fallmann J, Forkel R, Emeis S. 2016. Secondary effects of urban heat island mitigation measures on air quality. Atmospheric Environment, 125: 199-211.

Feng JM., Wang YL, Ma ZG, Liu YH. 2012. Simulating the regional impacts of urbanization and anthropogenic heat release on climate across China. Journal of Climate, 25(20): 7187-7203.

Gabriel KM, Endlicher WR. 2011. Urban and rural mortality rates during heat waves in Berlin and Brandenburg, Germany. Environmental Pollution, 159(8): 2044-2050.

Gatari, M.J., Boman, J., 2003. Black carbon and total carbon measurements at urban and rural sites in Kenya, East Africa. Atmospheric Environment, 37(8): 1149-1154.

Georgescu M. 2015. Challenges associated with adaptation to future urban expansion. Journal of Climate, 28(7): 2544-2563.

Grimm NB, Faeth SH, Golubiewski NE, Redman CL, Wu J, Bai X, Briggs JM. 2008. Global change and the ecology of cities. Science, 319: 756-760.

Grimmond CSB. 2006. Progress in measuring and observing the urban atmosphere. Theoretical and Applied Climatology, 84: 3-22.

Grimmond CSB, Roth M, Oke TR, Au YC, Best M, Betts R, Carmichael G, Cleugh H, Dabberdt W, Emmanuel R, Freitas E, Fortuniak K, Hanna S, Klein P, Kalkstein LS, Liu CH, Nickson A, Pearlmutter D, Sailor D, Voogts J. 2010. Climate and more sustainable cities: climate information for improved planning and management of cities (producers/capabilities perspective). Procedia Environmental Sciences, 1: 247-274.

Hamdi R, Vyver H, Troch R, Termonia P. 2014. Assessment of three dynamical urban climate downscaling methods: Brussels's future urban heat island under an A1B emission scenario. International Journal of Climatology, 34(4): 978-999.

Hartig T, Kahn PH. 2016. Living in cities, naturally. Science, 352: 938-940.

Hidalgo J, Masson V, Baklanov A, Pigeon G, Gimeno L. 2008. Advances in urban climate modeling. Annals of the New York Academy of Sciences, 1146(1): 354-374.

Hu L, Monaghan A, Voogt JA, Barlage M. 2016. A first satellite-based observational assessment of urban thermal anisotropy. Remote Sensing Environment, 181:111-121.

Ichinose T, Shimodozono K, Hanaki K. 1999. Impact of anthropogenic heat on urban climate in Tokyo. Atmospheric Environment, 33: 3897-3909.

Imhoff ML, Zhang P, Wolfe RE, Bounoua L. 2010. Remote sensing of the urban heat island,

effect across biomes in the continental USA. Remote Sensing Environment, 114 (3): 504-513.

Inouye DW. 2015. The next century of ecology. Science, 349: 565-565.

Jauregui E, Luyando E. 1999. Global radiation attenuation by air pollution and its effects on the thermal climate in Mexico City. International Journal of Climatology, 19(6): 683-694.

Kolokotroni M, Ren X, Davies M, Mavrogianni A. 2012. London's urban heat island: Impact on current and future energy consumption in office buildings. Energy and Buildings, 47: 302-311.

Kovats RS, Hajat S. 2008. Heat stress and public health: a critical review. Annual Review of Public Health, 29: 41-55.

Kusaka H, Hara M, Takane Y. 2012. Urban climate projection by the WRF model at 3-km horizontal grid increment: dynamical downscaling and predicting heat stress in the 2070's August for Tokyo, Osaka, and Nagoya metropolises. Journal of the Meteorological Society of Japan, 90: 47-63.

Leconte F, Bouyer J, Claverie R, Pétrissans M. 2015. Using Local Climate Zone scheme for UHI assessment: Evaluation of the method using mobile measurements. Building and Environment, 83: 39-49.

Lee DO. 1984. Urban cliamte. Progress in Physical Geography, 8(1):1-31.

Li D, Bou-Zeid E, Barlage M, Chen F, Smith JA. 2013. Development and evaluation of a mosaic approach in the WRF-Noah framework. Journal of Geophysical Research: Atmospheres. 118: 918-935.

Li H, Wolter M, Wang X, Sodoudi S. 2017. Impact of land cover data on the simulation of urban heat island for Berlin using WRF coupled with bulk approach of Noah-LSM. Theoretical and Applied Climatology, https://doi.org/10.1007/s00704-017-2253-z.

Li H, Zhou Y, Li X, Meng L, Wang X, Wu S, Sodoudi S. 2018a. A new method to quantify surface urban heat island intensity. Science of the Total Environment, 624: 262-272.

Li X, Zhou Y, Asrar GR, Zhu Z. 2018b. Creating a seamless 1km resolution daily land surface temperature dataset for urban and surrounding areas in the conterminous United States. Remote Sensing of Environment, 206: 84-97.

Lillo-Saavedra M, Gonzalo C. 2006. Spectral or spatial quality for fused satellite imagery? A trade-off solution using the wavelet à trous algorithm. International Journal of Remote Sensing, 27(7): 1453-1464.

Lin TP, Matzarakis A, Hwang RL. 2010. Shading effect on long-term outdoor thermal comfort. Building and Environment, 45(1): 213-221.

Loridan T, Lindberg F, Jorba O, Kotthaus S, Grossman-Clarke S, Grimmond C. 2013. High resolution simulation of the variability of surface energy balance fluxes across central London with urban zones for energy partitioning. Boundary-layer Meteorology, 147(3): 493-523.

Marin NF. 2017. Sustainable Self/Livable Net: Balancing sustainability and livability in dense urban environments through strategies for the mitigation of the UHI effect. Delft University of Technology, master thesis.

Martilli A. 2007. Current research and future challenges in urban mesoscale modelling. International Journal of Climatology, 27(14): 1909-1918.

McDonnell MJ, MacGregor-Fors I. 2016. The ecological future of cities. Science, 352: 936-938.

Meehl GA, Tebaldi C. 2004. More intense, more frequent, and longer lasting heat waves in the 21st century. Science, 305: 994-997.

Meng C, Zhang C, Miao S, Chen F. 2013. Localization and validation of an urbanized high-resolution land data assimilation system (u-HRLDAS). Science China Earth Sciences, 56(6): 1071-1078.

Mills G. 2008. Luke Howard and the climate of London. Weather, 63(6):153-157.

Min KD, Yoon JW, Ahn KD. 2005. A Study on the Atmospheric Environment and Simulations

of Wind Field using MUKLIMO at the KNU Campus. Journal of Environmental Science International, 14(3): 311-325.

Mirzaei PA, Haghighat F. 2010. Approaches to study urban heat island–abilities and limitations. Building and Environment, 45(10): 2192-2201.

Mirzaei PA. 2015. Recent challenges in modeling of urban heat island. Sustainable Cities and Society, 19: 200-206.

Morris CJG, Simmonds I, Plummer N. 2001. Quantification of the influences of wind and cloud on the nocturnal urban heat island of a large city. Journal of Applied Meteorology, 40(2): 169-182.

Moudon AV. 1997. Urban morphology as an emerging interdisciplinary field. Urban Morphology, 1(1): 3-10.

Navarro JA, Varma V, Riipinen I, Seland Ø, Kirkevåg A, Struthers H, Iversen T, Hansson HC, Ekman AM. 2016. Amplification of Arctic warming by past air pollution reductions in Europe. Nature Geoscience, 9(4): 277-281.

Oke TR, Fuggle RF. 1972. Comparison of urban/rural counter and net radiation at night. Boundary-Layer Meteorology, 2(3): 290-308.

Oke TR. 1973. City size and the urban heat island. Atmospheric Environment, 7(8): 769-779.

Oke TR, Maxwell GB. 1975. Urban heat island dynamics in Montreal and Vancouver. Atmospheric Environment, 9(2): 191-200.

Oke TR. 1976. The distinction between canopy and boundary-layer urban heat islands. Atmosphere, 14(4): 268-277.

Oke TR. 1982. The energetic basis of the urban heat island. Quarterly Journal of the Royal Meteorological Society, 108(455): 1-24.

Oke TR. 1981. Canyon geometry and the nocturnal urban heat island: comparison of scale model and field observations. International Journal of Climatology, 1(3): 237-254.

Oke TR. 1988a. The urban energy balance. Progress in Physical geography, 12(4): 471-508.

Oke TR. 1988b. Street design and urban canopy layer climate. Energy and buildings, 11: 103-113.

Oke TR. 1998. An algorithmic scheme to estimate hourly heat island magnitude. In Preprints Second Urban Environment Symposium. Boston, MA: American Meteorological Society, 80-83

Oke TR. 2006. Instruments and observing methods: Report No. 81: initial guidance to obtain representative meteorological observations at urban sites. World Meteorological Organization, WMO/TD (1250).

Oleson KW, Bonan GB, Feddema J, Vertenstein M. 2008. An urban parameterization for a global climate model. Part II: Sensitivity to input parameters and the simulated urban heat island in offline simulations. Journal of Applied Meteorology and Climatology, 47(4): 1061-1076.

Oleson KW, Bonan GB, Feddema J, Jackson T. 2011. An examination of urban heat island characteristics in a global climate model. International Journal of Climatology, 31(12): 1848-1865.

Peng S, Piao S, Ciais P, Friedlingstein P, Ottle C, Bréon FM, Nan H, Zhou L, Myneni RB. 2011. Surface urban heat island across 419 global big cities. Environmental Science & Technology, 46(2): 696-703.

Peterson JT, Stoffel TL. 1980. Analysis of urban-rural solar radiation data from St. Louis, Missouri. Journal of Applied Meteorology, 19(3): 275-283.

Phelan PE, Kaloush K, Miner M, Golden J, Phelan B, Silva III H, Taylor RA. 2015. Urban heat island: mechanisms, implications, and possible remedies. Annual Review of Environment and Resources, 40: 285-307.

Pueschel RF, Kuhn PM. 1975. Infrared absorption of tropospheric aerosols: Urban and rural aerosols of Phoenix, Arizona. Journal of Geophysical Research, 80(21): 2960-2962.

Rasul A, Balzter H, Smith C. 2015. Spatial variation of the daytime surface urban cool island , from Landsat 8. Urban Climate, 14:176-186.

Rajasekar U, Weng QH. 2009. Urban heat island monitoring and analysis using a non-parametric model: A case study of Indianapolis. ISPRS Journal of Photogrammetry and Remote Sensing, 64(1): 86–96.

Ramanathan, V., Carmichael, G., 2008. Global and regional climate changes due to black carbon. Nature geoscience, 1(4): 221.

Rizwan AM, Dennis LYC, Chunho LIU. 2008. A review on the generation, determination and mitigation of Urban Heat Island. Journal of Environmental Sciences, 20(1): 120-128.

Roth M. 2007. Review of urban climate research in (sub) tropical regions. International Journal of Climatology, 27(14): 1859-1873.

Rosenfeld AH, Akbari H, Romm JJ. 1998. Cool communities: Strategies for heat island mitigation and smog reduction. Energy and Buildings, 28: 51–62.

Runnalls KE, Oke TR. 2000. Dynamics and controls of the near-surface heat island of Vancouver, British Columbia. Physical Geography, 21(4): 283-304.

Salamanca F, Martilli A, Yagüe C. 2012. A numerical study of the Urban Heat Island over Madrid during the DESIREX (2008) campaign with WRF and an evaluation of simple mitigation strategies. International Journal of Climatology, 32(15): 2372–2386.

San José R, Pérez JL, González RM. 2013. Very High Resolution Urban Simulations with WRF/UCM and CMAQ over European Cities. Urban Environment. Springer, Dordrecht, pp 293-301.

Santamouris M. 2007. Heat island research in Europe: the state of the art. Advances in Building Energy Research, 1(1): 123-150.

Schatz J, Kucharik CJ. 2014. Seasonality of the urban heat island effect in Madison, Wisconsin. Journal of Applied Meteorology and Climatology, 53(10): 2371-2386.

Schwarz N, Lautenbach S, Seppelt R. Exploring indicators for quantifying surface urban heat islands of European cities with MODIS land surface temperatures. Remote Sens Environ 2011; 115(12): 3175-3186.

Schwarz N, Schlink U, Franck U, Großmann K. 2012. Relationship of land surface and air temperatures and its implications for quantifying urban heat island indicators—An application for the city of Leipzig (Germany). Ecological Indicators, 18: 693-704.

Scherer D, Fehrenbach U, Lakes T, Lauf S, Meier F, Schuster C. 2014. Quantification of heat-stress related mortality hazard, vulnerability and risk in Berlin, Germany. DIE ERDE–Journal of the Geographical Society of Berlin, 144: 238-259.

Scheffers BR, Meester LD, Bridge TCL, Hoffmann AA, Pandolfi JM, Corlett RT, Butchart SHM, Pearce-Kelly P, Kovacs KM, Dudgeon D, Pacifici M, Rondinini C, Foden WB, Martin TG, Mora C,Bickford D,†Watson, James EM. 2016. The broad footprint of climate change from genes to biomes to people. Science, 354: aaf7671.

Schubert S, Grossman‐Clarke S. 2014. Evaluation of the coupled COSMO‐CLM/DCEP model with observations from BUBBLE. Quarterly Journal of the Royal Meteorological Society, 140(685): 2465-2483.

Shahmohamadi P, Che-Ani AI, Ramly A, Maulud KNA, Mohd-Noret MFI. 2010. Reducing urban heat island effects: A systematic review to achieve energy consumption balance. International Journal of Physical Sciences, 5(6): 626-636.

Souch C, Grimmond S. 2006. Applied climatology: urban climate. Progress in Physical Geography, 30(2): 270-279.

Stone B. 2007. Urban and rural temperature trends in proximity to large US cities: 1951–2000. International Journal of Climatology, 27(13): 1801-1807.

Taha H. 1997. Urban climates and heat islands: albedo, evapotranspiration, and anthropogenic heat. Energy and Buildings, 25(2): 99-103.

Tan J, Zheng Y, Tang X, Guo C, Li L, Song G, Zhen X, Yuan D, Kalkstein AJ, Li F, Chen H. 2010. The urban heat island and its impact on heat waves and human health in Shanghai. International Journal of Climatology, 54(1):75-84.

Tan J, Yang L, Grimmond CSB, Shi J, Gu W, Chang Y, Hu P, Sun J, Ao X, Han Z. 2015. Urban integrated meteorological observations: practice and experience in Shanghai,

China. Bulletin of the American Meteorological Society, 96(1): 85-102.

Thomas C, Ranchin T, Wald L, Chanussot J. 2008. Synthesis of multispectral images to high spatial resolution: A critical review of fusion methods based on remote sensing physics. IEEE Transactions on Geoscience and Remote Sensing, 46(5): 1301-1312.

United Nations, Department of Economic and Social Affairs, Population Division (2015). World Urbanization Prospects: The 2014 Revision, (ST/ESA/SER.A/366).https://esa.un.org/unpd/wup/Publications/Files/WUP2014-Report.pdf.

Unger J. 2004. Intra-urban relationship between surface geometry and urban heat island: review and new approach. Climate research, 27(3): 253-264.

Urban Senate. 2015 Urban Development Concept Berlin 2030 http://www.stadtentwicklung.berlin.de/planen/stadtentwicklungskonzept/download/strategie/BerlinStrategie_Broschuere_en.pdf.

Vogelmann AM, Flatau PJ, Szczodrak M, Markowicz KM, Minnett PJ. 2003. Observations of large aerosol infrared forcing at the surface. Geophysical Research Letters, 30(12), DOI: 10.1029/2002GL016829.

Voogt JA, Oke TR. 2003. Thermal remote sensing of urban climates. Remote sensing of environment, 86(3): 370-384.

Ward K, Lauf S, Kleinschmit B, Endlicher W. 2016. Heat waves and urban heat islands in Europe: A review of relevant drivers. Science of the Total Environment, 569: 527-539.

Wang X, Li Y. 2016. Predicting urban heat island circulation using CFD. Building and Environment, 99: 82-97.

Wang WC, Zeng Z, Karl TR. 1990. Urban heat islands in China. Geophysical Research Letters, 17(13): 2377-2380.

Williamson SN, Hik DS, Gamon JA, Kavanaugh JL, Koh S. 2013. Evaluating cloud contamination in clear-sky MODIS Terra daytime land surface temperatures using

ground-based meteorology station observations. Journal of Climate, 26(5):1551–1560.

Wu J. 2014. Urban ecology and sustainability: The state-of-the-science and future directions. Landscape and Urban Planning, 125: 209-221.

Xie ZQ, Du Y, Zeng Y, Yan ML, Zhu CY. 2010. Accelerated human activities affecting the spatial pattern of temperature in the Yangtze River Delta. Quaternary International, 226: 112-121.

Yang X, Li Y, Luo Z, Chan PW. 2017. The urban cool island phenomenon in a high‐rise high‐density city and its mechanisms. International Journal of Climatology, 37(2): 890-904.

Yow DM. 2007. Urban heat islands: observations, impacts, and adaptation. Geography Compass, 1(6): 1227-1251.

Yuan F, Bauer ME. 2007. Comparison of impervious surface area and normalized difference vegetation index as indicators of surface urban heat island effects in Landsat imagery. Remote sensing of Environment, 106(3): 375-386.

Zauri R, Schiaroli R, Leonardi FG, Berni N. 2010. Numerical weather prediction models' temperature post-processing in heat wave early warning in Umbria: a case study and preliminary results. Italian Journal of Agrometeorology, 15(3): 43-60.

Zhang P, Imhoff ML, Wolfe RE, Bounoua L. 2010. Characterizing Urban Heat Islands of Global Settlements Using MODIS and Nighttime Lights Products. Canadian Journal of Remote Sensing, 36(3): 185-196.

Zhang J, Wang Y, Li Y. 2006. A C++ program for retrieving land surface temperature from the data of Landsat TM/ETM+ band6. Computers & Geosciences, 32(10): 1796-1805.

Zhao L, Lee X, Smith RB, Oleson K. 2014. Strong contributions of local background climate to urban heat islands. Nature, 511: 216-219.

Zhou L, Dickinson RE, Tian Y, Fang J, Li Q, Kaufmann RK, Compton JT, Myneni RB. 2004. Evidence for a significant urbanization effect on climate in China. Proceedings of the

National Academy of Sciences of the United States of America, 101(26): 9540-9544.

Zhou S, Chow S, Zheng J. 1991. The turbidity island effect in Shanghai urban climate. Energy and Buildings, 16(1): 657-662.

Zhou B, Rybski D, Kropp JP. 2017. The role of city size and urban form in the surface urban heat island. Scientific Reports, 7(1): 4791.

Zhou Y, Shepherd JM. 2010. Atlanta's urban heat island under extreme heat conditions and potential mitigation strategies. Natural Hazards, 52(3): 639-668.

Zhou D, Zhang L, Hao L, Sun G, Liu Y, Zhu C. 2016. Spatiotemporal trends of urban heat island effect along the urban development intensity gradient in China. Science of The Total Environment, 544: 617-626.

Appendix

This Appendix presents the full context of chapter 2 to 5, which are submitted to peer-reviewed journals. All these papers have been published and can be found online.

Paper I

This article has been published on “Theoretical and Applied Climatology”. It is available at https://doi.org/10.1007/s00704-017-2253-z. This paper was attached below with kind permission from the journal.

Citation: Li H., Wolter M., Wang X., Sodoudi S. 2017. Impact of land cover data on the simulation of urban heat island for Berlin using WRF coupled with bulk approach of Noah-LSM. *Theoretical and Applied Climatology*, https://doi.org/10.1007/s00704-017-2253-z.

Author Contributions: Li H. designed the research, carried out model simulation and data analysis, and drafted the manuscript. Sodoudi S. contributed ideas to the data analysis and the drafting of the manuscript, and supervised the study. Wolter M. provided the technical support for model simulation and data analysis, and reviewed the manuscript. Wang X. contributed to the discussion of the results and the manuscript revision.

Impact of land cover data on the simulation of urban heat island for Berlin using WRF coupled with bulk approach of Noah-LSM

Huidong Li[1], Michael Wolter[1], Xun Wang[1], Sahar Sodoudi[1*]

1 Institute of Meteorology, Freie Universität Berlin

Abstract

Urban-rural difference of land cover is the key determinant of urban heat island (UHI). In order to evaluate the impact of land cover data on the simulation of UHI, a comparative study between up-to-date CORINE land cover (CLC) and Urban Atlas (UA) with fine resolution (100 and 10 m) and old US Geological Survey (USGS) data with coarse resolution (30 s) was conducted using the Weather Research and Forecasting model (WRF) coupled with bulk approach of Noah-LSM for Berlin. The comparison between old data and new data partly reveals the effect of urbanization on UHI and the historical evolution of UHI, while the comparison between different resolution data reveals the impact of resolution of land cover on the simulation of UHI. Given the high heterogeneity of urban surface and the fine-resolution land cover data, the mosaic approach was implemented in this study to calculate the sub-grid variability in land cover compositions. Results showed that the simulations using UA and CLC data perform better than that using USGS data for both air and land surface temperatures. USGS-based simulation underestimates the temperature, especially in rural areas. The longitudinal variations of both air and land surface temperature show good agreement with urban fraction for all the three simulations. To better study the comprehensive characteristic of UHI over Berlin, the UHI curves (UHIC) are developed for all the three simulations based on the relationship between temperature and urban fraction. CLC- and UA-based simulations show smoother UHICs than USGS-based simulation. The simulation with old USGS data obviously underestimates the extent of UHI, while the up-to-date CLC and UA data better reflect the real urbanization and simulate the spatial distribution of UHI more accurately. However, the intensity of UHI simulated by CLC and UA data is not higher than that simulated by USGS data. The simulated air temperature is not dominated by the land cover as much as the land surface temperature, as air temperature is also affected by air advection.

Keywords: Urban heat island. CORINE land cover. Urban Atlas. WRF mesoscale model. Noah-LSM. Mosaic approach. Urbanization

1 Introduction

The phenomenon of urban heat island (UHI) refers to higher temperatures in urban areas, compared with their surrounding areas (Oke1982; Rizwan et al. 2008). In some metropolitan regions, the UHI effect is very distinct, with intensity exceeding 10 K (Huang et al. 2005). UHI increases the intensity of extreme heat waves (McCarthy et al. 2010; Huang and Lu 2015). People living in cities suffer from more heat stress (Zhou and Shepherd 2010) than those living in rural areas. UHI causes serious health (Kovats and Hajat 2008), environment (Sarrat et al. 2006), and even energy problems (Kolokotroni et al. 2012). Given the continuous growth of urban areas and their populations in the twenty-first century, UHI will continue to grow (Rizwan et al. 2008). Concerns about the possible hazards caused by UHI are rising (Roth 2007; Grimm et al. 2008). The accurate localization and forecasting of UHI are becoming increasingly important.

Numerical simulation is an important method to investigate UHI, with a wide area of successful applications. Myrup (1969) used a numerical energy budget model to simulate UHI and suggested that such a model could be used in engineering calculations to improve the climate of existing and future cities. Chen et al. (2004) simulated the UHI phenomenon over the Greater Houston area utilizing the coupled Weather Research and Forecasting (WRF)/land surface model (LSM)/Urban modeling system. Huang et al. (2005) developed an urban thermal environment numerical simulation tool, coupled with convection, radiation, and conduction, and studied the urban thermal environment of an actual complex urban area covering a large district-wide heating and cooling system in summer. Cheng et al. (2013) investigated the effect of different land use and land cover patterns on mesoscale meteorological simulations of the Taiwan area using the WRF model. Trusilova et al. (2013) coupled COSMO climate limited-area model (COSMO-CLM) with town energy budget (TEB) parameterization and found that the COSMO-CLM+TEB model was able to more accurately represent the magnitude of the urban heat island than the standard COSMO-CLM model. Meanwhile, Trusilova et al. (2016) compared bulk, single-layer, and multi-layer urban land

parameterizations using COSMO-CLM and found that they all captured the urban heat island despite how the results differ in spatial detail, magnitude, and the diurnal variation. Giannaros et al. (2013) simulated UHI over Athens using the WRF model coupled with Noah-LSM and found that the model could reveal a satisfactory performance. Fallmann et al. (2016) assessed the effect of urban heat island mitigation strategies on regional air quality using WRF/Chem. Zuvela-Aloise et al. (2015) modeled the urban climate under global climate change in Central European cities using MUKLIMO_3. Arnfield (2003) and Rizwan et al. (2008) listed many other numerical models in their reviews of urban heat island studies. Urban numerical simulations have come a long way since the 1970s. Nevertheless, they still suffer from some basic problems, one of which is the unsatisfactory specification of land cover data (Oke 1988).

Land cover is an important input data for urban climate models, affecting the simulation of land processes such as mass and energy exchange between the surface and the atmosphere (Twine et al. 2004). Chen et al. (2007) found that the improvements in predictions of boundary layer development, cloud, precipitation, and surface meteorological conditions rely on the land surface physics and the initialization of land state. Sertel et al. (2010) compared the up-to-date land cover data derived from Landsat ETM+ images and the US Geological Survey (USGS) data for the Marmara Region, Turkey, and found that the WRF simulation with new land cover dataset produces higher temperature within the region, which is more accurate than the USGS data. The difference in land cover between urban and rural regions is the key factor causing UHI (Arnfield 2003; Rizwan et al. 2008). The urban surface absorbs more solar radiation due to its lower albedo than natural surfaces. Meanwhile, the sealed surface allocates more intercepted energy to sensible heat flux, rather than latent heat flux, due to the unavailability of water. Bowen ratio, the ratio of sensible heat flux and latent heat flux, is an important indicator of the type of surface and represents the allocation of the obtained energy (Oke 1988; Li et al. 2016). Christen and Vogt (2004) found that the values of Bowen ratio for urban surface are much larger than those for the rural surface. The higher absorbed energy and Bowen ratio lead to the higher temperature in urban regions, compared to rural regions (Oke 1982). Accurate numerical simulations of UHI require reliable land

cover data. The default land cover data used by current climate models, however, are not satisfactory, and unsuitable for urban climate simulation. In the WRF model, for example, the default land cover data come from USGS, recorded in 1994, with the resolution of 30 s. Old land cover data are unable to reflect land-use modification due to rapid urbanization (De Meij and Vinuesa 2014), and the coarse resolution is incapable of representing the high heterogeneity of urban surface. Both of these are important error sources in urban climate simulation. It is necessary, therefore, to continually update land cover data and increase its resolution to represent real surface characteristics.

In this study, the old (1994) USGS land cover data with 30-s resolution, updated (2012) CORINE land cover data with 100-m resolution, and updated (2012) Urban Atlas data with 10-m resolution were applied to simulate the urban heat island of Berlin. The mesoscale climate model of WRF was utilized. Given the high heterogeneity of urban surface and the fine resolution land cover data, the mosaic approach was implemented in this study to calculate the sub-grid variability in land cover compositions. The simulation results were evaluated against in-situ measured air temperature and remotely sensed land surface temperature. The urban heat islands of both air temperature and land surface temperature were analyzed. To better study the comprehensive characteristic of UHI over Berlin, the UHI curve (UHIC) was developed based on the relationship between temperature and urban fraction. Three land cover data used in this study have different timeliness and resolution. The comparison between old data and new data can partly reveal the effect of urbanization on UHI and the historical evolution of UHI, while the comparison between different resolution data can reveal the impact of resolution on the simulation of UHI. Both of these can provide a useful reference for the future study of the simulation of urban climate.

2 Data and method

2.1 Study area

The study area is Berlin, the capital city of Germany. Berlin (52.34°–52.68° N, 13.10°–13.77° E) is located in northeast Germany (Fig. 1a) and is influenced by a temperate maritime climate with a mean annual temperature of 9.5 °C and annual precipitation of 591 mm (data

based on the German Meteorological Office Dahlem station measurements in the 30-year period 1981–2010). It has a flat topography (34– 122 m, altitude) and covers an area of about 900 km^2. According to the year 2015 report of the Statistical Office of Berlin-Brandenburg (https://www.statistik-berlinbrandenburg.de), Berlin has about 3.5 million inhabitants, with a third living in the inner city in an area of about 88 km^2. It is the second most populous city in the European Union. Berlin is a heavily urbanized region with about 35% built-up areas. In addition, transport and infrastructure areas cover about 20% of the city. Berlin's built-up areas create a microclimate with pronounced urban heat island effects, leading to a higher potential heat stress risk in central city areas (Dugord et al. 2014).

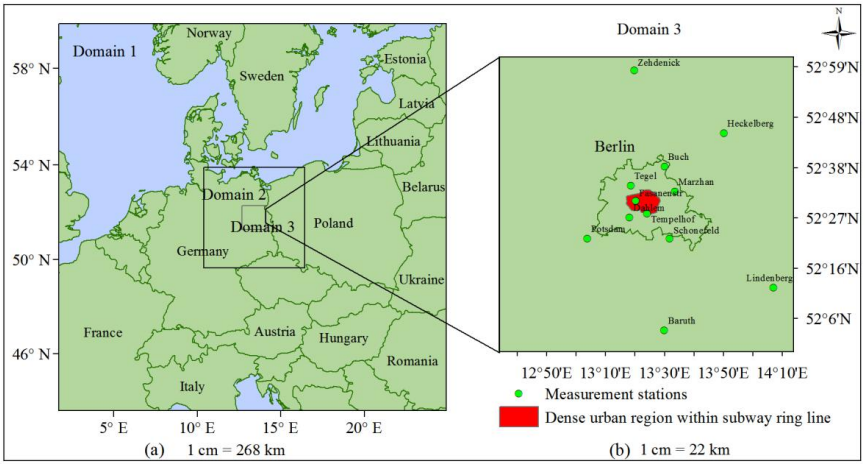

Fig. 1 Domain setup (a) and the locations of the measurement stations in Berlin and surrounding rural regions (b).

2.2 Land cover data

Land cover data from the USGS, CORINE land cover (CLC), and Urban Atlas (UA) were used in this study. The USGS data is the original land cover data for WRF simulations (De Meij and Vinuesa 2014). It was compiled by the United States Geological Survey in 1994. USGS data with a resolution of 30s (~1km) was used herein. The CLC and UA data come from Copernicus, a European system for monitoring the Earth. The data are collected from different sources, including earth observation satellites and in-situ sensors, and provide reliable and updated information. The scale of CLC is 1:100,000 with minimum mapping unit of 25 ha (Feranec et al. 2007). The Urban Atlas provides pan-European comparable land cover data for functional urban areas (Prastacos et al. 2011). It has a scale of 1:10,000, and

minimum mapping unit of 0.25 ha for artificial surfaces, with 1 ha for other surfaces. The CLC and UA data adopt the CORINE land cover nomenclature scheme, while the UA data use a fourth level of artificial surfaces to distinguish between the different subcategories. The CLC and UA data are updated every 6 years, and the 2012 data are used here. Default USGS data for WRF running has 28 land cover classes (including lake). It does not distinguish detailed urban surface and only includes one urban class. To keep the land cover classification unified and reduce the uncertainties, the CLC and UA data are also reclassified into 28 classes, referring to the land-use category equivalence study conducted by Pineda et al. (2004). Furthermore, given large areas of lakes surround Berlin (6.7% based on CLC data), the lakes are distinguished from other water bodies as their own independent class in this study. This partition can prevent the surface temperature over lakes from being extrapolated from the nearest sea surface temperature (SST), leading to inaccurate initial values for lake surface temperatures.

2.3 Configuration of the WRF model

The WRF model is a next-generation mesoscale numerical weather prediction system designed for both operations and research. WRF provides recent advances in meteorology and numerics. It has been in development since its first version was published in 2001. As one of the most popular numerical models currently, the WRF model is suitable for a broad span of applications across different topics, including urban climate studies (Chen et al. 2011).

WRF model version 3.7.1 was employed in this study. Three nested domains with horizontal grid spacing of 15, 3, and 1 km were designed, with 119 × 119, 155 × 155, and 111 × 111 grid cells, respectively (Fig. 1a). In the vertical direction, 35 levels were used. The vertical resolution near the surface was set as 10 m and stretched above. The physical parameterization schemes were chosen as follows: (1) the WRF single-moment 5-class scheme (Hong et al.2004) for microphysics; (2) the Dudhia and RRTM scheme (Mlawer et al.1997) for shortwave and longwave radiation, respectively; (3) the Eta similarity scheme for surface layer; (4) the Mellor-Yamada-Janjic planetary boundary layer scheme; and (5) the Noah-LSM scheme for land surface process (WarrachSagi et al. 2013). Given that the 28 classes land cover data only includes one urban class, the UCM scheme is not coupled here.

Noah-LSM adopts bulk approach to represent zero order effects of the urban surface. Giannaros et al. (2013) found that WRF model coupled with Noah-LSM could reveal a satisfactory performance for the UHI simulation over Athens. Bhati and Mohan (2016) compared the simulation of urban climate in Delhi using WRF and WRF/UCM and found out that WRF model could perform satisfactorily, although WRF/UCM shows a better performance. WRF model coupled with Noah-LSM could simulate UHI well. The values of the urban surface parameters used here are set referring to Giannaros et al. (2013) as follows: 0.15 for albedo, 0.8 for roughness, 1.9×10^6 J m^3 K^{-1} for heat capacity, and 3.0 W m^{-1} K^{-1} for heat conductivity.

Reanalysis data from Global Forecast System (GFS) at the spatial resolution of 0.5° and temporal resolution of 6 h (ftp://nomads.ncdc.noaa.gov/GFS/) is input as the initial and lateral boundary conditions. In addition, given the long-term running, the daily SST (ftp://polar.ncep.noaa.gov/pub/history/sst/) at the spatial resolution of 0.5° is also used in this study.

The simulations were conducted over the period from June 21 to July 3, 2010. This period had typical weather conditions for the formation of urban heat island (Oke and Maxwell1975). Most days had clear sky with calm wind. During half of the period, the cloud fraction was less than 25%. The mean value of wind speed was 2.46 m/s during the day and 1.81 m/s at night. The simulation results were collected at 30-min interval for the finer grid simulations. The first 24 h were taken as spin-up time. The simulation results from domain 3 (finest) were used for evaluation and for studying the characteristic of UHI in Berlin.

2.4 Land cover data configuration

Three simulations were designed using different configurations of land cover data, as shown in Table 1. The USGS simulation used the default USGS data for all three domains. The CLC and UA simulations both used CLC data for domains 1 and 2. For domain 3, the CLC simulation also used CLC data, while the UA simulation used UA data. Given the differences in resolution between the grid cell and the fine land cover data, the mosaic approach in the WRF-Noah framework was applied in this study, instead of the default dominant approach, to

configure the land cover data over each grid cell. As shown in Fig. 2, the default dominant approach just considers the land cover category which has the largest coverage and loses all the other land cover information. It is easy to generate errors, especially for the coarse grid simulation using fine resolution land cover data. Mosaic approach allows considering more land cover types within each single grid cell based on the choice of the user (N=3 in Fig. 2c). In this way, it is possible to account for the sub-grid scale variability of land surface characteristics within each grid. Surface fluxes and surface state variables were calculated for each tile using its surface properties, such as albedo and emissivity, and were aggregated to yield the weighted average variables within each grid cell (Li et al. 2013). Sensible heat flux, latent heat flux, surface temperature, emissivity, albedo, and momentum roughness length are the key grid cell averaged surface variables in the mosaic approach. Mosaic approach could reduce the sensitivity of grid resolution on the results and avoid the errors resulting from the interpolation of land cover data. In this paper, the number (N) of tiles is determined when the accumulated areas of the first N principal land cover types exceed 99% of the areas of the grid cell. Table 2 displays the mean area fractions occupied by N tiles averaged over domain 3. Within the USGS grids, the first largest category accounts for 95.92%. When the first two largest categories are considered, the percentage becomes very large, close to 100%. Within the UA and CLC grids, however, the first largest categories have fractions of just 77.01 and 78.04%, respectively. For CLC grids, when the number of tiles increases to three, the total fraction (99.14%) becomes larger than 99%. For UA grids, the number of tiles needs to increase to four before the total fraction (99.67%) reaches over 99%. On average, the USGS grids have three categories at most, while the number of land cover categories of UA and CLC grids both reaches to six. In order to save simulation time, the first 99% land cover categories were considered in this paper. Eventually, the mosaic values were determined as two, three, and four for the three simulations (Table 2).

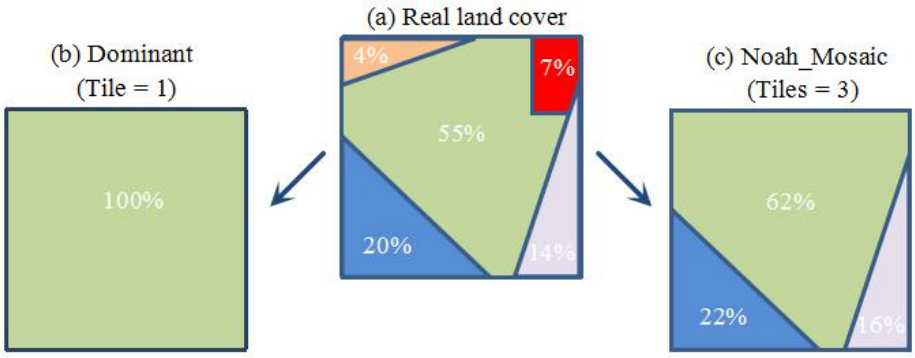

Fig. 2 Schematic diagram of interpolation of (a) real land cover datasets using (b) dominant approach and (c) Noah-Mosaic approach. Each color in the tiles represents one land cover type. As an example in this schematic diagram, three tiles that contain 90% of the real land cover information were chosen to represent the land cover characteristic of the grid cell.

Table 1. Configuration of land cover data for the three simulations.

Simulations	Land cover data configuration			Urban information within domain 3		
	Domain 1	Domain 2	Domain 3	Number of urban grids	Urban fraction within urban grids (%)	Total urban fraction (%)
USGS	USGS	USGS	USGS	728	86.94	5.26
CLC	CLC	CLC	CLC	1314	72.18	11.64
UA	CLC	CLC	UA	1401	68.88	13.64

Table 2. Cumulative area fractions (%) occupied by N tiles (land cover types) within the grids of domain 3 and the mosaic values of the three simulations.

Simulations	Cumulative area fractions by N tiles						Mosaic values
	1	2	3	4	5	6	
USGS	95.92	99.97	100.00	100.00	100.00	100.00	2
CLC	78.04	95.17	99.14	99.89	99.99	100.00	3
UA	77.01	94.11	98.50	99.67	99.95	100.00	4

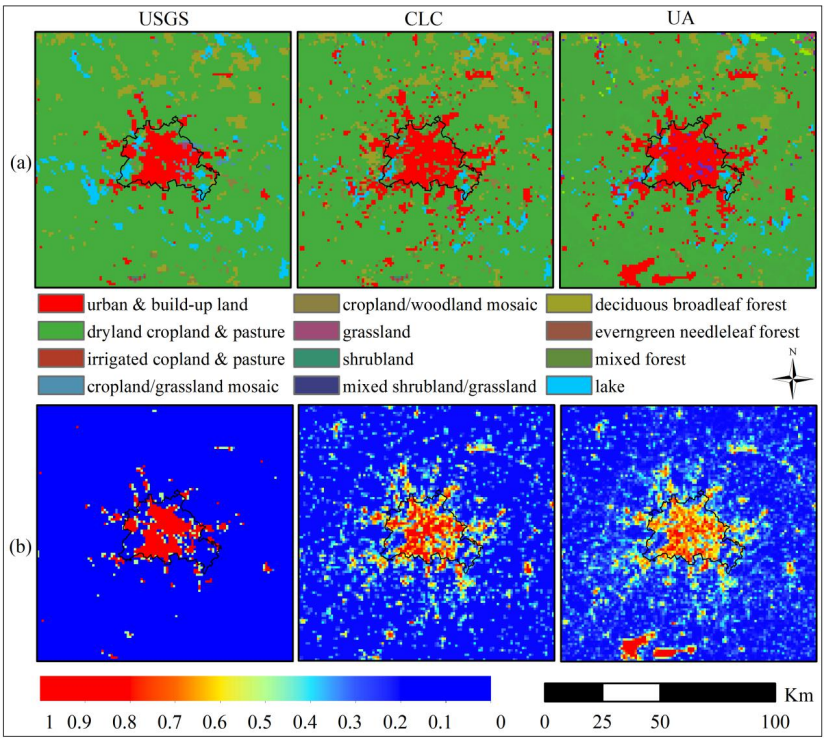

Fig. 3 Spatial distribution of (a) dominant land cover and (b) urban fractions within domain 3 for USGS data (left), CORINE data (middle), and Urban Atlas data (right). The color bar below represents the urban fraction changing from zero to one. The black line is the border of the Berlin. Here, the dominant land cover classes refer to the land cover class that has the largest coverage, while urban fraction is the coverage of urban land cover areas over each grid cell. They are retrieved from the LANDUSEF and LU_INDEX within the results of geogrid.exe program on the platform of WRF Preprocessing System (WPS).

Spatial distribution of dominant land cover classes (land cover class that has largest coverage within the grid cell) and urban fractions (coverage of the land cover class "urban" within the grid cell) within domain 3 for all three cases is presented in Fig. 3. The USGS domain has the fewest urban areas, and most of its urban grids are concentrated in central Berlin. UA and CLC domains have more urban areas, with some urban grids also located in the surrounding rural regions. The numbers of urban grids in the UA, CLC, and USGS domains are 1401, 1314, and 728, while the urban fractions are 13.64, 11.64, and 5.26%, respectively (Table 1). UA and CLC data display the results of urbanization better than USGS data. Meanwhile, UA and CLC data represent land covers more accurately because of their finer resolution. Fig. 3(b) shows the spatial distribution of urban fraction within each grid.

The USGS data have large urban fractions (close to 1) in the city center, concentrated in a small area, while the CLC and UA data have a wider distribution of urban surface, with smaller values in the city center. The mean value of urban fractions within urban grids of the UA and CLC domains are 68.88 and 72.18%, respectively, while the fraction within USGS domain reaches 86.94% (Table 1).

2.5 Measurement data and processing

Table 3. Land cover information at measurement stations.

Station	Lon (E)/ Lat (N)	USGS		CLC		UA	
		Dominant land cover	Urban fraction	Dominant land cover	Urban fraction	Dominant land cover	Urban fraction
Heckelberg	13.84/52.77	Crop/pasture	0.00	Crop/pasture	0.03	Crop/pasture	0.07
Lindenberg	14.11/52.21	Crop/pasture	0.00	Crop/pasture	0.26	Crop/pasture	0.16
Zehdenick	13.22/52.97	Crop/pasture	0.00	Crop/pasture	0.47	Crop/pasture	0.35
Baruth	13.50/52.06	Crop/pasture	0.00	Urban	0.44	Crop/pasture	0.35
Potsdam	13.06/52.38	Crop/pasture	0.00	Forest	0.12	Forest	0.24
Schoenefeld	13.53/52.38	Crop/pasture	0.00	Crop/pasture	0.48	Urban	0.56
Tempelhof	13.40/52.47	Urban	0.50	Forest	0.00	Grassland	0.01
Fassanenstr	13.34/52.51	Urban	1.00	Forest	0.29	Forest	0.39
Buch	13.50/52.63	Crop/pasture	0.00	Urban	0.82	Urban	0.81
Tegel	13.31/52.56	Crop/pasture	0.00	Urban	1.00	Urban	0.86
Dahlem	13.30/52.45	Urban	1.00	urban	0.67	Urban	0.65
Marzahn	13.56/52.54	Urban	1.00	Urban	0.99	Urban	0.80

Hourly measured in-situ data at twelve meteorological stations were used to evaluate the simulated 2-m air temperature in domain 3 (Fig. 1b). Land cover information for these measurement sites is shown in Table 3. At stations located in the dense built-up regions, such as Dahalem, Fassanenstr, Tempelhof, and Marzahn, the USGS data always overestimates the urban fraction, because the coarse resolution cannot recognize the small green areas. UA data

has the finest spatial resolution and can best recognize the urban areas in the suburban regions and the green areas in the urban regions. At stations located in the rapidly developing suburban regions, such as Schoenefeld, Potsdam, Buch, and Tegel, the USGS data always underestimates the urban areas within the grids, due to the failure of the old USGS data in reflecting the reality of urbanization. On the other hand, the coarse spatial resolution of USGS data easily omits small urban areas. The updated CLC and UA data are able to represent real-time surface characteristics, and their fine spatial resolution assists in recognizing small urban areas. At stations located in the Berlin surrounding regions, such as Lindenberg, Zehdenick, Heckelberg, and Baruth, the urban fractions are relatively low. In particular the station of Heckelberg shows very low urban fraction, close to 0 for all three land covers. Heckelberg station is very little affected by urbanization and reflects the natural conditions.

Land surface temperature (LST) from Moderate Resolution Imaging Spectroradiometer (MODIS) satellite observations was used to assess the simulated LST. Daily MODIS LST products version 6 level 3 at the resolution of 1000 m were applied in this study (Wan2014). Two images observed by AQUA satellite at ~1:30 am (UTC) on June 27, 2010, and at ~1:30 pm (UTC) on June 28, 2010, were chosen for the evaluation due to their high quality and few clouds. The LST images were downloaded from NASA (https://ladsweb.nascom.nasa.gov/search/). Next, the LST images were reprojected and resampled to match the model grids in domain 3 using ArcGIS.

2.6 Development of UHI curves

Urban heat island intensity (UHII), the temperature difference between urban and rural areas, is the classical indicator to quantitatively describe UHI effect (Rizwan et al. 2008). Currently, UHII calculations are usually conducted using the measurements over the dense built-up surfaces and rural natural surfaces. However, this method only reflects parts of the feature of UHI over measurement stations. The values of UHII are very sensitive to the selection of urban and rural stations (Oke 2006). To overcome the problem caused by urban/rural divisions and to study the overall characteristic of UHI, a good approach for the quantification of UHII is required to consider the comprehensive conditions of cities at large scale. Urban fraction reflects the degree of land-use change and provides a robust estimation of the intensiveness of

human activities. Schubert and Grossman-Clarke (2013) analyzed the relationship between air temperatures and urban fraction for Berlin during extreme heat events and found that the air temperature showed a small increase with the rising urban fraction. Hu and Brunsell (2015) came up with a new approach, urban heat island curve (UHIC), using the relationship between temperature and urban fraction. In this study, the grids of domain 3 were divided into 50 parts with 2% interval of the urban fractions. The mean values of temperature and urban fractions were calculated within each interval and were used to develop the UHIC. Water bodies show a big difference with other land covers in thermal properties and would affect the relationship between temperature and urban fraction (Hu and Brunsell 2015). To eliminate the disturbance of lakes, the grids with areas of more than 10% lakes are excluded during the development of the UHIC. The UHICs were developed for both day and night, respectively. Periods of daytime and nighttime were determined based on the time of sunrise (UTC 3:00) and sunset (UTC 19:30) during the study period in the Berlin region.

2.7 Evaluation measures

Mean bias (MB), root mean square error (RMSE), and Pearson correlation coefficient (r) were used as model evaluation measures in this study. The equations of these measures are as follows:

$$MB = \frac{1}{n}\sum_{i=1}^{n}(T_{m,i} - T_{o,i}) \quad (1)$$

$$RMSE = \sqrt{\frac{\sum_{i=1}^{n}(T_{m,i} - T_{o,i})^2}{n}} \quad (2)$$

$$r = \frac{1}{n-1}\sum_{i=1}^{n}\left(\frac{T_{m,i} - \mu_{T_m}}{\sigma_{T_m}}\right)\left(\frac{T_{o,i} - \mu_{T_o}}{\sigma_{T_o}}\right) \quad (3)$$

where $T_{m,i}$ and $T_{o,i}$ are the modelling and observation temperature at time i for in-situ 2m air temperature and grid i for land surface temperature, respectively, °C. μ and σ are the mean and standard deviation of temperature.

3 Results

3.1 Evaluation of simulated LST

Table 4 shows the RMSE and MB of the simulated LST, compared to the MODIS observation data. In the daytime, the MB shows positive values for all the three simulations, in particular the USGS-based simulation with the smallest value of 4.39 °C. The RMSE of the USGS-based simulation (5.59 °C) is much larger than that of the CLC- (4.20 °C) and UA (4.13 °C)-based simulations. At night, the USGS-based simulation still shows underestimation (-0.47 °C), while CLC- (0.17 °C) and UA-based simulations (0.31 °C) show a little overestimation. The RMSE shows a smaller difference between the three simulations, at 2.81, 2.46, and 2.47 °C, respectively. Overall, the USGS-based simulation has the largest bias. CLC- and UA-based simulations show no obvious difference in both the RMSE and MB. The RMSE and MB were calculated for urban (urban fraction larger than 50% based on CLC data) and rural regions (urban fraction less than 50% based on CLC data), separately. The CLC- and UA-based simulations always perform better than USGS-based simulation in both the urban and the rural regions. In addition, the model performance in the urban regions is not as good as in the rural regions. The high heterogeneity of urban surface should be the reason.

Table 4. RMSE and MB (°C) of the simulated LST compared against the MODIS data at daytime (UTC 1:30 pm on 28/06/2010) and nighttime (UTC time 1:30 am on 27/06/2010). Urban and rural grids are separated based on CLC data. Urban and rural grids refer to the grid with urban fraction larger and less than 50%, separately.

Indicators	Time	USGS			CLC			UA		
		USGS	CLC	UA	USGS	CLC	UA	USGS	CLC	UA
RMSE	Daytime	5.36	6.35	5.26	4.00	4.02	4.00	3.92	4.34	3.87
	Nighttime	2.23	2.72	2.17	1.93	3.12	1.77	1.94	2.74	1.84
MB	Daytime	-4.39	-5.55	-4.28	-2.72	-3.01	-2.69	-2.65	-3.43	-2.58
	Nighttime	-0.47	0.66	-0.58	0.17	2.75	-0.08	0.34	2.32	0.11

3.2 Evaluation of simulated air temperature

The simulated 2-m air temperature was evaluated using in-situ measurement data. Table 5 shows the RMSE, MB, and correlation coefficients between the simulations and measurements. All the simulations show good agreement with measurements, with high correlation coefficients. CLC- and UA-based simulations show much lower RMSE, meaning better performance than USGS-based simulation. USGS-based simulation underestimates the air temperature at most of the stations, because the old USGS data cannot reflect the urbanization and underestimate the urban fraction (Table 3). CLC- and UA-based simulations also show underestimations at most stations, but their absolute values of MB are much smaller than that of the USGS-based simulation. The difference in MB and RMSE between the USGS-based simulation and the other two simulations is related to the difference in urban fraction. At the rural station of Heckelberg, the urban fractions are close to 0 for all three land cover data. The difference of the model performance is very small among the three simulations. Fig. 4 shows the mean diurnal variations of 2-m air temperature of measurements and simulations over the stations in Berlin during the simulation period. Diurnal variations of mean urban temperature (temperature over the girds with urban fraction more than 50%) of the three simulations are very similar (Fig. 4a). In general, WRF simulations could capture the diurnal variation of 2-m air temperature. Compared to the measurements, all the simulations show underestimation during the day and overestimation at night. When the comparison of the diurnal variation is only conducted over measurement grids (Fig. 4b), the difference among the simulations becomes more significant. USGS-based simulation is always lower than CLC- and UA-based simulations. At night, CLC- and UA-based simulations are very close to the measurements, while USGS-based simulation still shows underestimation. This is because most of the stations are located in the suburban regions, and old USGS data largely underestimate the urban fraction, leading to the underestimation of air temperature (Table 3). The simulations based on the CLC and UA data always show similar variations and do not vary a lot. When the resolution of land cover data is good enough (much higher than the resolution of the grids), the higher resolution cannot further improve the model performance.

Table 5. RMSE and MB (°C) of the simulated air temperature compared against in-situ measurement data.

Stations	RMSE			MB			*r*		
	USGS	CLC	UA	USGS	CLC	UA	USGS	CLC	UA
Zehdenick	2.25	1.67	1.73	-1.41	-0.42	-0.58	0.96	0.97	0.96
Heckelberg	1.77	1.73	1.73	-0.64	-0.18	-0.19	0.96	0.96	0.96
Baruth	3.05	2.07	2.12	-1.63	-0.87	-0.89	0.95	0.96	0.95
Lindenberg	2.99	2.18	2.21	-2.56	-1.65	-1.66	0.95	0.96	0.96
Potsdam	2.08	1.40	1.38	-1.55	-0.36	-0.37	0.97	0.97	0.97
Schoenefeld	2.35	1.55	1.45	-1.82	-0.65	-0.46	0.96	0.96	0.97
Tempelhof	1.80	1.45	1.46	-1.16	-0.34	-0.44	0.96	0.96	0.97
Fassanenstr	1.81	1.92	1.87	-0.58	-0.68	-0.65	0.95	0.95	0.95
Buch	2.30	1.70	1.71	-1.61	0.08	0.01	0.96	0.96	0.96
Tegel	2.22	1.32	1.36	-1.67	-0.08	-0.27	0.96	0.97	0.97
Dahlem	1.98	2.02	1.88	0.63	0.76	0.68	0.95	0.95	0.95
Marzahn	1.78	1.39	1.53	-1.23	-0.50	-0.76	0.97	0.97	0.97
Total	2.34	1.72	1.73	-1.27	-0.41	-0.48	0.94	0.95	0.96

3.3 Comparison of the spatial patterns of the simulated temperature

Fig. 5 presents the spatial distribution of mean simulated LST. The CLC and UA simulations show larger areas affected by UHI in both the city center and the recently developed surrounding regions, compared with the USGS simulation. The old USGS data cannot reflect the recent urbanization and underestimate the UHI extent. In the USGS-based simulation, the UHI is mainly located in the central part of Berlin (if areas containing lakes are ignored). The mean LST of USGS is 1.06 and 1.11 °C and 0.67 and 0.77 °C lower than CLC and UA simulations during the day and at night (Table 6). The difference of mean LST between three simulations during the day is larger than at night. In addition, the USGS-simulated LST is

relatively homogeneous within urban regions, with fewer high value areas than in the CLC and UA simulations. LST relies strongly on the land cover data. The coarse resolution of USGS data is unable to represent the impact of sub-grid variation of land cover data on the simulations of LST. The boundary for the USGS-simulated UHI is very remarkable. Spatial distribution of mean simulated 2-m air temperature is presented in Fig. 6. The CLC and UA simulations show more grids with high temperature compared with USGS simulation, similar to the distributions of LST above. The high temperature areas of the CLC and UA simulations are located not only in the central regions but also in some surrounding regions where the urban fractions are large. The USGS simulation only has high temperature areas in the central city (if areas with lakes are not included). The mean air temperature of USGS is about 0.77 and 0.79 °C, and both 0.82 °C lower than CLC and UA simulations during the day and at night (Table 6). The USGS simulation also shows more homogeneous spatial pattern than CLC and UA simulations. Furthermore, the spatial distributions of T_{2m} are smoother than those of LST for all the three simulations. Air temperature does not depend on land cover data as much as LST, as it is also affected by air advection.

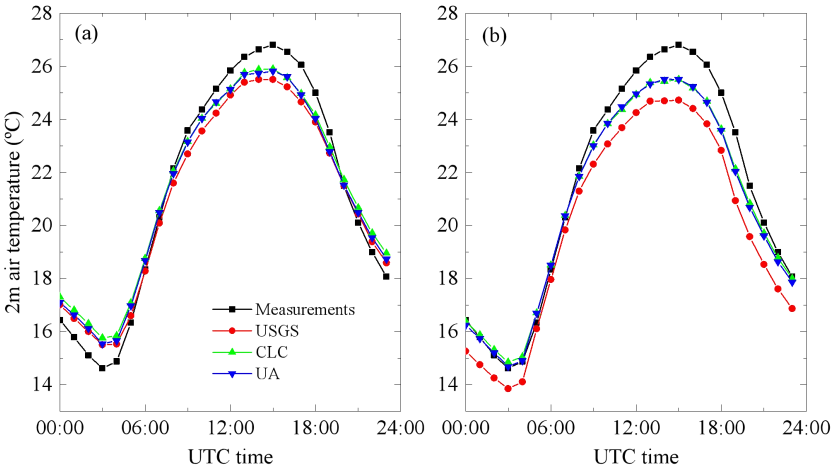

Fig. 4 Mean diurnal variations of the measured and simulated 2m air temperature during the simulation period. Black curves represent the mean value of the measurements at the urban and suburban stations listed in Table 3. Green, red and blue curves represent the mean values of WRF-simulated air temperature using USGS, CLC and UA data, respectively, over (a) the urban grids of each land cover dataset over Berlin, and (b) over the grids that the measurement stations located over Berlin.

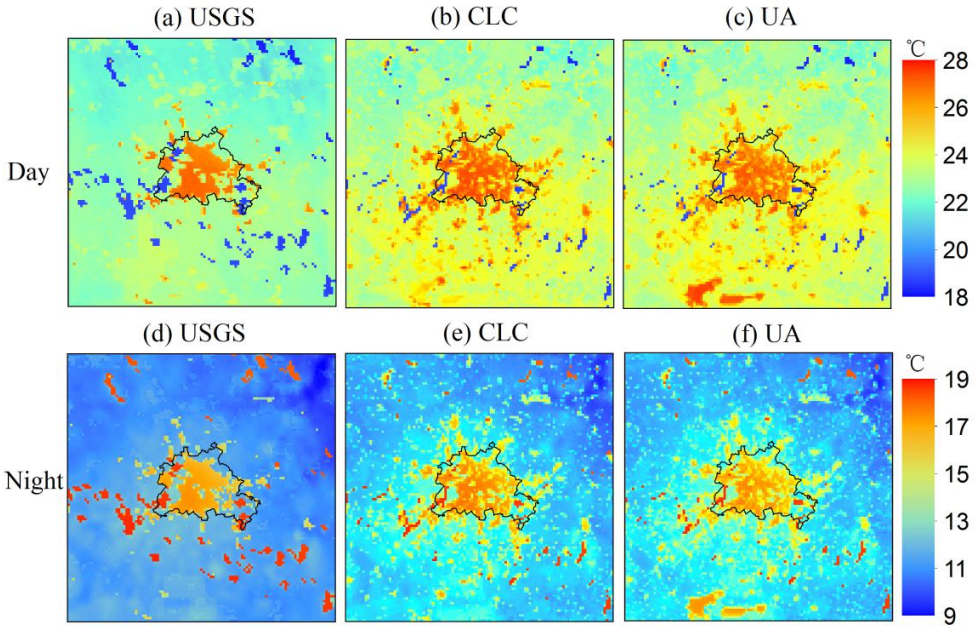

Fig. 5 Spatial distribution of mean simulated LST. (a), (b) and (c) are the map of mean LST during the day, while (d), (e) and (f) are the map for the mean nighttime LST for USGS, CLC and UA simulations.

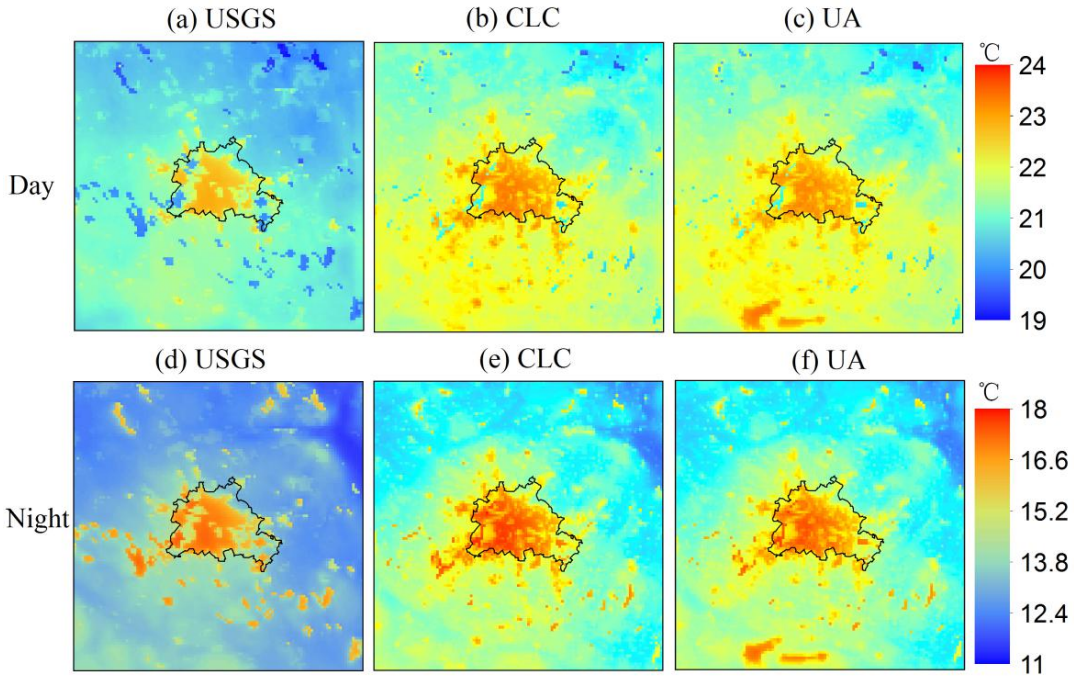

Fig. 6 Spatial distribution of the mean simulated 2m air temperature. (a), (b) and (c) are the map of mean air temperature during the day, while (d), (e) and (f) are the map for the mean nighttime air temperature for USGS, CLC and UA based simulations.

Table 6. Mean values of the simulated LST and T_{2m} (°C) within domain 3 for all the three simulations.

Temperature	Time	USGS	CLC	UA
LST	Daytime	22.60	23.66	23.71
	Nighttime	11.74	12.38	12.48
T_{2m}	Daytime	20.90	21.67	21.69
	Nighttime	13.38	14.20	14.20

3.4 Comparison of the longitudinal profiles of the simulated temperature

For a clear overview of the spatial structure of the simulated UHI over Berlin, the longitudinal variations of both mean air temperature and LST within the latitude 52.28 – 52.33° North (extent of ring subway line, Fig. 1b) for both daytime and nighttime are presented in Fig. 7. It shows that as areas change from rural to inner-city, land covers change from natural to urban, and both temperatures and urban fraction increase. In the city center, urban fractions rise beyond 90% for USGS data and 80% for CLC and UA data. Temperatures also maintain high values, presenting a typical urban heat island phenomenon. Then back from the center towards rural regions, land covers change from urban to natural with the decrease of urban fractions. The temperature also decreases. The urban temperature of the USGS simulation is similar to that of the CLC and UA simulations, while the rural temperature of the USGS simulation is significantly lower than that of the CLC and UA simulations, leading to the overestimation of the intensity of UHI. Furthermore, both temperature and urban fraction of USGS-based simulation decrease significantly near the suburban region, while the temperature of CLC- and UA-based simulations varies smoothly along with the urban fraction. USGS-based simulation overestimates the intensity of UHI but underestimates its extent. In all three simulations, during the day, the air temperature is always lower than LST. The LST-T2m difference in the central regions is more noticeable than that in the rural regions. In contrast, at night, in the urban center, the air temperature is very close to the land surface temperature, and even takes a smaller value at some points, while in rural regions, the air temperature is always much higher than the land surface temperature.

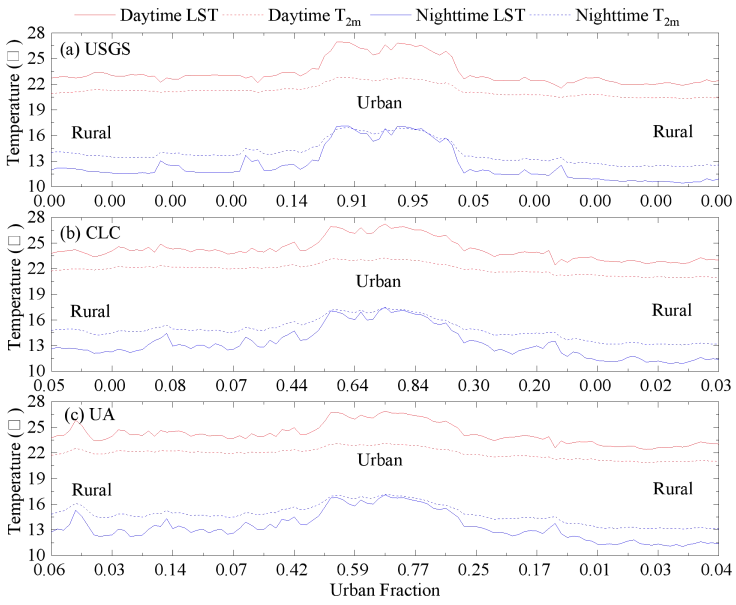

Fig. 7 Longitudinal variations of the simulated temperature versus urban fraction within the latitude 52.28-52.33 degrees North.

3.5 Variation of the simulated temperature versus urban fraction, UHIC

In an attempt to study the overall characteristic of UHI in the whole city scale, UHIC, namely the variation of temperature versus urban fraction, was developed for each simulation. The developed UHICs are presented in Fig. 8. Both air temperature and LST show good positive relationship with urban fractions, especially LST with higher correlation coefficient. LST increases more drastically than air temperature along with urban fraction. This means that the SUHII is higher than the UHII. At night, when the urban fraction is very small, the LST is much lower than the air temperature, but the difference between them gradually reduces with the increase in urban fraction, and finally the LST even exceeds the air temperature. The change of the LST-T_{2m} difference is consistent with Fig. 6. The LST shows a much closer correlation with land cover than the air temperature does.

The distribution of the urban fraction of the three land cover varied significantly. The old USGS data cannot reflect recent urbanization and its coarse resolution cannot identify the small urban areas in rural regions and small vegetation areas in urban regions. The distribution of USGS urban fractions is concrete, with large numbers of extremely high and low values. The UHIC of USGS-based simulation shows drastic fluctuations. In contrast, the

up-to-date CLC and UA data with fine resolution show more continuous distributions of urban fractions. The UHIC of CLC- and UA-based simulations are smoother than that of USGS-based simulation. The number of grids with high urban fraction can be taken as the UHI extent. Although USGS data shows a larger number of grids for the extremely high interval of 0.98 – 1.00, its cumulative number of grids with high urban fraction is smaller than that of CLC and UA data. Taking 0.5 as the criteria for the high urban fraction, the number of USGS (543) data is much smaller than that of CLC (1086) and UA (1128) data. The simulation with old USGS data obviously underestimates the extent compared to the CLC- and UA-based simulations. Given the good positive correlation between temperature and urban fraction, the variation of temperature along with the increase in urban fraction from 0 to 1 can be taken as an indicator of UHI intensity (UHII). USGS-based simulation underestimates the temperature in both urban and rural regions than CLC and UA based simulations, and the underestimation of LST in the rural regions is more significant than in the urban regions. Although the new CLC and UA data help to recognize more UHI areas, the intensity of UHI simulated by them is not enhanced.

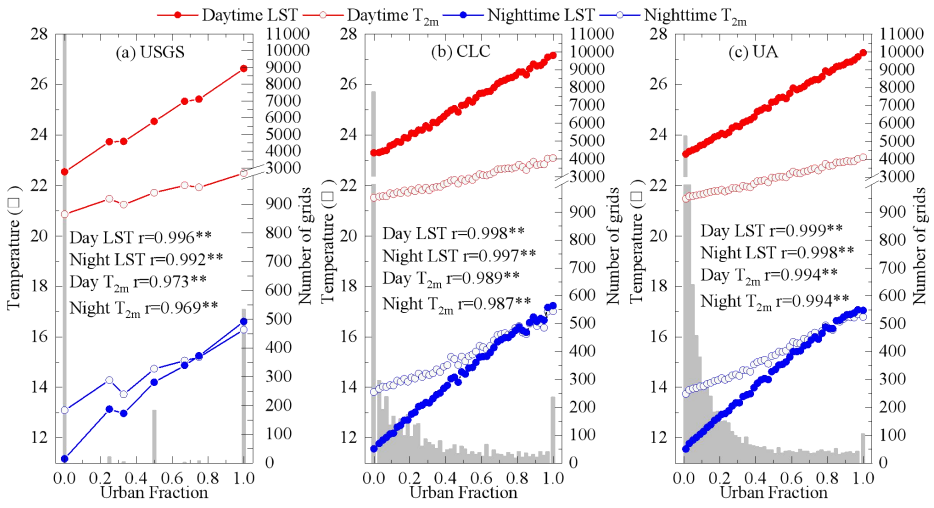

Fig. 8 Variation of mean temperature versus urban fraction (UHIC). The mean temperature and urban fraction are calculated using the grids within each urban fraction interval (2%). The red and blue dots represent temperature during the day and at night. The solid dots and hollow dots represent LST and 2m air temperature, respectively. The grey bars represent the distribution of the number of grids within each interval of urban fraction. r is the Pearson Correlation Coefficient between the mean temperature and urban fraction ($p<0.01$).

4 Discussions

4.1 Comparison of the simulated surface energy balance

Land cover significantly controls the energy budget on the earth surface. The difference of surface energy budget between urban and rural regions, caused by different surface properties, leads to UHI (Oke 1982; 1988). UHI effect is closely related to land cover. To further explore the cause of the different performance of these three simulations, the distributions of mean surface energy balance components during the day, including net radiation, sensible heat flux, latent heat flux and ground heat flux, are presented in Fig. 9. The urban regions show greater net radiation than rural regions, due to the lower albedo (Christen and Vogt 2004). The CLC- and UA-based simulations show large areas with great net radiation, not only in the central city but also in urbanized surrounding areas. Great radiation areas of the USGS-based simulation are smaller, only located in central regions. The net radiation difference between central and rural regions of the USGS-based simulation is larger than in the CLC- and UA-based simulations. In urban regions, the surface absorbed energy is mainly allocated to sensible heat flux or stored in the ground, while in the rural regions, most absorbed energy is allocated to latent heat flux. Comparison of the longitudinal variations of the energy components is presented in Fig. 10. It shows that the difference of the energy allocation of USGS-based simulation is very noticeable in the rural regions. For CLC- and UA-based simulations, the sensible heat flux in rural regions is very close to the latent heat flux. In some grids with high urban fractions, the sensible heat flux even exceeds latent heat flux. Meanwhile, the rural ground heat flux of CLC- and UA-based simulations is larger than that of USGS-based simulation. The greater net radiation and larger allocation to the sensible heat flux of CLC- and UA-based simulations make the rural regions much warmer than the rural regions of the USGS-based simulation. At night, solar radiation disappears, then the energy stored in the surface is released as the energy source to mitigate the surface cooling. The urban surface releases more energy than the natural surface due to more energy stored in the urban regions during the day, maintaining the UHI phenomena at night.

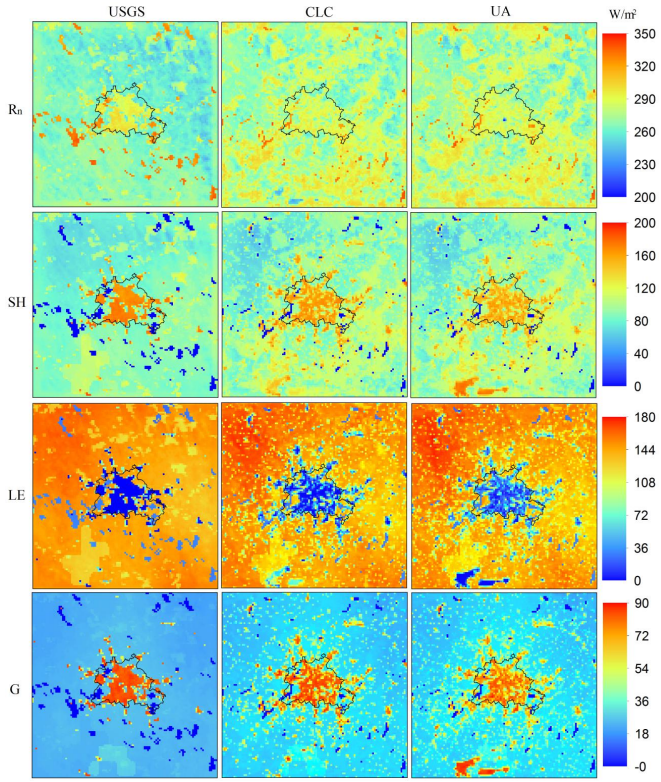

Fig. 9 Spatial distribution of mean simulated surface energy components during the day. R_n: net radiation; SH: sensible heat flux; LE: latent heat flux; G: ground heat flux.

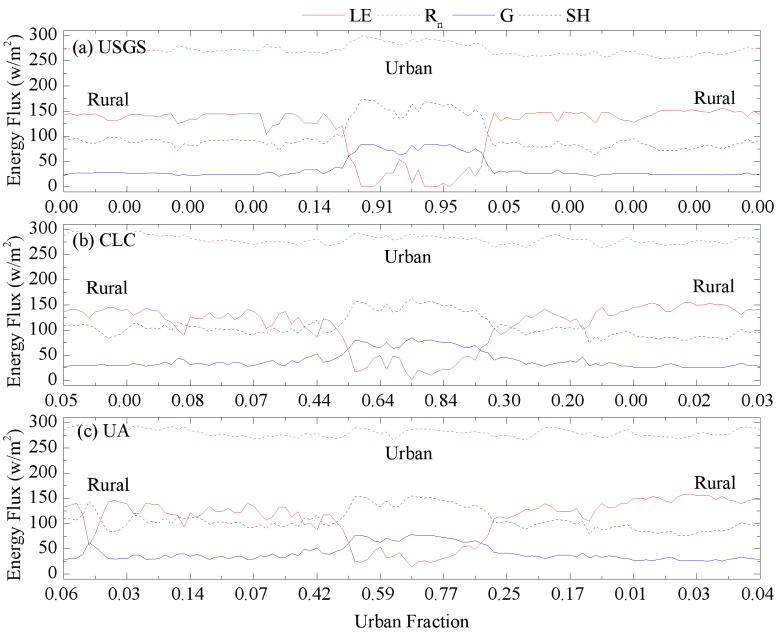

Fig. 10 Longitudinal variation of mean simulated daytime surface energy components versus urban fraction within the latitude 52.28-52.33 degrees north. R_n: net radiation; SH: sensible heat flux; LE: latent heat flux; G: ground heat flux.

4.2 Effect of urbanization and spatial resolution of land cover on the simulations of urban climate

Timeliness of land cover plays an important role for the simulation of urban climate. Our results showed that the old USGS land cover data created in the early 1990s cannot represent the recent urbanization and would underestimate the temperature in the real urban region and the extent of UHI. Similar results have been reported by many studies before. Cheng et al. (2013) found WRF simulation with USGS data underestimated daytime temperatures in western Taiwan due to the underestimation of urban areas. De Meij and Vinuesa (2014) found that CLC data showed higher fraction of urban and built-up area than USGS data in Lombardy region (north Italy). For both winter and summer periods, the WRF simulations with CLC data showed higher temperatures over the model domain than USGS-based simulation, especially in the summer with differences of average temperatures of up to 2.7 °C. Bhati and Mohan (2016) assessed the UHI in Delhi using WRF and found that modification of land cover improved the model performance for non-urban areas. In our study, the accuracy of the USGS-based simulation is significantly lower than that of the CLC- and UA-based simulations for both air temperature and LST, especially in the rural regions where land cover changed drastically. USGS-based simulation underestimates the temperature in the surrounding areas of Berlin and the extent of UHI. This is consistent with the previous study results mentioned above.

Land cover resolution is another indicator to weigh the accuracy of surface conditions and also affects the WRF simulations. In coarse-resolution data, it is easy to ignore small urban areas in rural regions and vegetation areas in urban regions. On average, the fraction of the first dominant land cover of USGS data exceeds 95.92% within the grids (Table 2). Although another land cover is included in the grids of USGS-based simulation, the simulation results are still mainly determined by the first dominant land cover (Fig. 3b). The simulation using coarse-resolution USGS data cannot reflect the sub-grid variation of temperature within each grid well. It can be seen from Figs.5 and 6 that the USGS simulated temperatures distribute very homogeneously within both high and low value regions, showing an obvious border between them. Meanwhile, too much urban areas within the urban grids

decrease the water availability of the surface, leading to extremely low latent heat flux (Figs. 9 and 10). CLC and UA data come from the same year and classification system. Both of them have fine resolution, much better than the grid size. Mosaic approach used here guarantees the CLC- and UA-based simulations to distinguish more land cover within the grid cells than USGS-based simulation (Table 2). The simulated temperatures vary gradually from the urban center to rural regions (Figs. 5 and 6). The finer resolution should be another reason for the better performance of CLC- and UA-based simulations than USGS-based simulation. On the other hand, the comparison between CLC- and UA-based simulations does not show a significant difference. None of them show absolute advantage over the other one. The simulation results are sensitive to the resolution of land cover only when the resolution of land cover is very coarse. When the resolution becomes fine enough (much better than the resolution of grids), the increase of land cover resolution will not further improve the model performance. The dependence of the simulation results on land cover resolution becomes weak. With the regard to the threshold of the so-called fine-enough resolution, further sensitivity studies are required.

4.3 Weaker dependence of air temperature than LST on land cover

LST represents the surface radiant temperature, while air temperature means the ambient temperature at 2-m height. LST is mainly dominated by the surface properties, while air temperature is controlled by the surface sensible heat flux and air advection, together. Heaviside et al. (2015) found that during the heat wave, the air temperature downwind of Birmingham were up to 2.5 °C warmer than the air temperature upwind, due to horizontal advection of warm air. Azevedo et al. (2016) quantified and identified the spatial pattern of UHI and SUHII using high-resolution air temperature and MODIS LST data in Birmingham, UK, and found that the distribution of the SUHI appeared to be clearly linked to land cover data, while advective processes appeared to play an important role in the distribution of UHI besides land cover data. In this study, the comparison of Figs. 5 and 6 shows that the spatial distribution of air temperature is always smoother than LST. LST changes more significantly than air temperature. Furthermore, the LST shows a much higher correlation with the land cover than air temperature does (Fig. 8). As noted by Azevedo et al. (2016), the impact of

advective processes on air temperature could be the cause of the weaker correlation between air temperature and urban fraction.

5 Conclusions

The appropriate representation of land cover is essential for urban climate simulation due to its high heterogeneity in urban areas. This paper evaluated the impact of three land cover data on the simulation of urban heat island using WRF coupled with Noah-LSM. USGS data (with coarse resolution), CORINE land cover data, and Urban Atlas data (both with fine resolution) were used in this paper. Mosaic approach was applied to consider more land cover types within each grid. Urban heat island curves (UHIC) were used to analyze the comprehensive feature of UHI. The results show that the UA- and CLC-based simulations perform better than the USGS-based simulation for both air temperature and land surface temperature. The USGS-based simulation underestimates the temperature, especially in the rural areas. The UA- and CLC-based simulations more accurately reflect the spatial distribution of urban heat island, while the USGS-based simulation underestimates the extent of urban heat island. The longitudinal variation of temperature is in good agreement with urban fraction. The CLC- and UA-based simulations show smoother UHICs than USGS-based simulation. Generally, the updated and fine-resolution land cover data reflect the real land surface condition and are much better for the simulation of urban heat island.

The difference between old USGS data and up-to-date CLC and UA data partly reflects the urbanization process, particularly in the surrounding developing regions. As for the cities like Berlin, the central regions are already highly urbanized. The simulated temperature in central regions based on different land cover is very similar. The further urbanization mainly happens in the rural regions. As the city was extending, more natural surfaces were converted into impervious surfaces. The surrounding regions get warmer, leading to the decrease of urban-rural temperature difference. Therefore, in the well-developed cities, the further urbanization process would increase the extent of UHI but maybe not increase the intensity of UHI. For the long-term calculation of UHII using traditional two in situ stations, the influence of land-use change on the calculation results must be considered, especially around the rural station. In addition, it should be noticeable that the conclusions above are drawn from the

perspective of the change of land cover. The real urbanization also includes the increase of population, traffic, and factories and the following emissions of anthropogenic heat. The comprehensive influence of urbanization on UHI is more complex and need more studies.

Mosaic approach enables the model to consider more fine resolution land cover types in each grid. The resolution of land cover can affect the simulation results as well, and the influence of the resolution on the model performance is related to the magnitude of the resolution itself. When the resolution of land cover data is very coarse, increasing the resolution would produce better simulation results. But when the resolution becomes fine enough (much better than the resolution of grids), increasing the land cover resolution may not further improve the model performance. The sensitivity of resolution of land cover data on the simulation of UHI needs to be conducted in the next research to find out the best choice for the resolution of land cover data.

Acknowledgements

This research is supported by the China Scholarship Council and FUBright Mobility Allowances for Research Stays promoted by the German Academic Exchange Service (DAAD)-Dahlem Research School of Freie Universität Berlin. The authors thank the Beijing Office of Freie Universität Berlin. Special thanks go to David Mottram for proofreading this manuscript and to Dr. Hamid Taheri Shahraiyni for help in processing remote sensing data.

References

Arnfield AJ (2003) Two decades of urban climate research: a review of turbulence, exchanges of energy and water, and the urban heat island. Int J Climatol 23:1–26.https://doi.org/10.1002/joc.859

Azevedo JA, Chapman L, Muller CL (2016) Quantifying the daytime and night-time urban heat island in Birmingham, UK: a comparison of satellite derived land surface temperature and high resolution air temperature observations. Remote Sens 8:153

Bhati S, Mohan M (2016) WRF model evaluation for the urban heat island assessment under varying land use/land cover and reference site conditions. Theor Appl Climatol

126:385–400

Chen F, Manning KW, LeMone MA, Trier SB, Alfieri JG, Roberts R, Tewari M, Niyogi D, Horst TW, Oncley SP, Basara JB (2007) Description and evaluation of the characteristics of the NCAR high-resolution land data assimilation system. J Appl Meteorol Clim 46(6):694–713

Chen F, Kusaka H, Bornstein R, Ching J, Grimmond CSB, GrossmanClarke S, Loridan T, Manning KW, Martilli A, Miao S, Sailor D, Salamanca FP, Taha H, Tewari M, Wang X, Wyszogrodzki AA, Zhang C (2011) The integrated WRF/urban modelling system: development, evaluation, and applications to urban environmental problems. Int J Climatol 31:273–288.https://doi.org/10.1002/joc.2158

Chen F, Kusaka H, Tewari M, Bao J, Hirakuchi H (2004) Utilizing the coupled WRF/LSM/urban modeling system with detailed urban classification to simulate the urban heat island phenomena over the Greater Houston area. Fifth Symposium on the Urban Environment. https://ams.confex.com/ams/pdfpapers/79765.pdf

Cheng FY, Hsu YC, Lin PL, Lin TH (2013) Investigation of the effects of different land use and land cover patterns on mesoscale meteorological simulations in the Taiwan area. J Appl Meteorol Clim 52:570–587

Christen A, Vogt R (2004) Energy and radiation balance of a central European city. Int J Climatol 24(11):1395–1421 De Meij A, Vinuesa J (2014) Impact of SRTM and Corine Land Cover data on meteorological parameters using WRF. Atmos Res 143:351–370

Dugord P-A, Lauf S, Schuster C, Kleinschmit B (2014) Land use patterns, temperature distribution, and potential heat stress risk—the case study Berlin, Germany. Comput Environ Urban Syst 48:86–98

Fallmann J, Forkel R, Emeis S (2016) Secondary effects of urban heat island mitigation measures on air quality. Atmos Environ 125:199–211

Feranec J, Hazeu G, Christensen S, Jaffrain G (2007) Corine land cover change detection in Europe (case studies of the Netherlands and Slovakia). Land Use Policy 24(1):234–247

Giannaros TM, Melas D, Daglis IA, Keramitsoglou I, Kourtidis K (2013) Numerical study of the urban heat island over Athens (Greece) with the WRF model. Atmos Environ 73:103–111.https://doi.org/10.1016/j.atmosenv.2013.02.055

Grimm NB, Faeth SH, Golubiewski NE, Redman CL, Wu J, Bai X, Briggs JM (2008) Global change and the ecology of cities. Science 319:756–760

Heaviside C, Cai XM, Vardoulakis S (2015) The effects of horizontal advection on the urban heat island in Birmingham and the West Midlands, United Kingdom during a heatwave. Quart J Roy Meteor Soc 141(689):1429–1441

Hu L, Brunsell NA (2015) A new perspective to assess the urban heat island through remotely sensed atmospheric profiles. Remote Sens Environ 158:393–406

Huang H, Ooka R, Kato S (2005) Urban thermal environment measurements and numerical simulation for an actual complex urban area covering a large district heating and cooling system in summer. Atmos Environ 39:6362–6375

Huang Q, Lu Y (2015) The effect of urban heat island on climate warming in the Yangtze River Delta urban agglomeration in China. Int J Environ Res Public Health 12:8773–8789

Hong SY, Dudhia J, Chen SH (2004) A revised approach to ice microphysical processes for the bulk parameterization of clouds and precipitation. Mon Weather Rev 132(1):103–120

Kolokotroni M, Ren X, Davies M, Mavrogianni A (2012) London's urban heat island: impact on current and future energy consumption in office buildings. Energy Build 47:302–311

Kovats RS, Hajat S (2008) Heat stress and public health: a critical review. Annu Rev Public Health 29:41–55

Li D, Bou-Zeid E, Barlage M, Chen F, Smith JA (2013) Development and evaluation of a mosaic approach in the WRF-Noah framework. J Geophys Res Atmos 118:918–935

Li H, Wang A, Yuan F, Guan D, Jin C, Wu J (2016) Evapotranspiration dynamics over a

temperate meadow ecosystem in eastern Inner Mongolia. China, Environ Earth Sci 75:978.https://doi.org/10.1007/s12665-016-5786-z

Mccarthy MP, Best MJ, Betts RA (2010) Climate change in cities due to global warming and urban effects. Geophys Res Lett.https://doi.org/10.1029/2010GL042845

Mlawer EJ, Taubman SJ, Brown PD, Iacono MJ, Clough SA (1997) Radiative transfer for inhomogeneous atmospheres: RRTM, a validated correlated-k model for the longwave. J Geophys Res Atmos 102:16663–16682

Myrup LO (1969) A numerical model of the urban heat island. J Appl Meteorol 8:908–918

Oke TR (1982) The energetic basis of the urban heat island. Q J R Meteorol Soc 108:1–24

Oke TR (1988) The urban energy balance. Prog Phys Geogr 12:471–508

Oke TR (2006) Instruments and observing methods: report no. 81: initial guidance to obtain representative meteorological observations at urban sites. World Meteorological Organization, WMO/TD, 1250

Oke TR, Maxwell GB (1975) Urban heat island dynamics in Montreal and Vancouver. Atmos Environ 9(2):191–200

Pineda N, Jorba O, Jorge J, Baldasano J (2004) Using NOAA AVHRR and SPOT VGT data to estimate surface parameters: application to a mesoscale meteorological model. Int J Remote Sens 25:129–143

Prastacos P, Chrysoulakis N, Kochilakis G (2011). Urban Atlas, land use modelling and spatial metric techniques. In 51st European congress of the Regional Science Association International. European Regional Science Accossiation. Barcelona, Spain.http://www.ekf.vsb.cz/export/sites/ekf/projekty/cs/weby/esf-0116/databazeprispevku/clanky_ERSA_2011/ERSA2011_paper_01406.pdf

Rizwan AM, Dennis LYC, Liu C (2008) A review on the generation, determination and mitigation of urban heat island. J Ecol Environ Sci 20:120–128.https://doi.org/10.1016/s1001-0742(08)60019-4

Roth M (2007) Review of urban climate research in (sub)tropical regions. Int J Climatol 27:1859–1873

Sarrat C, Lemonsu A, Masson V, Guedalia D (2006) Impact of urban heat island on regional atmospheric pollution. Atmos Environ 40:1743–1758.https://doi.org/10.1016/j.atmosenv.2005.11.037

Sertel E, Robock A, Ormeci C (2010) Impacts of land cover data quality on regional climate simulations. Int J Climatol 30(13):1942–1953

Schubert S, Grossman-Clarke S (2013) The influence of green areas and roof albedos on air temperatures during extreme heat events in Berlin, Germany. Meteorol Z 22(2):131–143

Trusilova K, Fruh B, Brienen S, Walter A, Masson V, Pigeon G, Becker P (2013) Implementation of an urban parameterization scheme into the regional climate model COSMO-CLM. J Appl Meteorol Clim 52: 2296–2311.https://doi.org/10.1175/jamc-d-12-0209.1

Trusilova K, Schubert S, Wouters H, Früh B, Grossman-Clarke S, Demuzere M, Becker P (2016) The urban land use in the COSMO-CLM model: a comparison of three parameterizations for Berlin. Meteorol Z 25(2):231–244

Wan Z (2014) New refinements and validation of the collection-6 MODIS land-surface temperature/emissivity product. Remote Sens Environ 2014:36–45

Twine TE, Kucharik CJ, Foley JA (2004) Effects of land cover change on the energy and water balance of the Mississippi River basin. J Hydrometeorol 5:640–655

ZhouY, Shepherd JM (2010) Atlanta's urban heat island under extreme heat conditions and potential mitigation strategies. Nat Hazards 52:639–668

Zuvela-Aloise M, Bokwa A, Dobrovolny P, Gal T, Geletic J, Gulyas A, Hajto M, Hollosi B, Kielar R, Lehnert M (2015) Modelling urban climate under global climate change in Central European cities. EGU General Assembly Conference Abstracts 17:1594

Paper II

This article has been published on “Science of the Total Environment”. It is open access and available at https://doi.org/10.1016/j.scitotenv.2017.11.360. This paper was attached below with kind permission from the journal.

Citation: Li H., Zhou Y., Li X., Meng L., Wang X., Wu S., Sodoudi S. 2018. A new method to quantify Surface Urban Heat Island Intensity. *Science of the Total Environment*, 624:262-272.

Author Contributions: Li H. designed the paper, analyzed the data, and draft the manuscript. Sodoudi S. contributed to the analysis of results, reviewed the manuscript, and supervised the study. Zhou Y., Li X., and Meng L. contributed to the research design and provide technical support, and reviewed the manuscript. Wang X. and Wu S. contributed ideas to the discussion of results and reviewed the manuscript.

A new method to quantify surface urban heat island intensity

Huidong Li[1], Yuyu Zhou[2], Xiaoma Li[2], Lin Meng[2], Xun Wang[1], Sha Wu[3], Sahar Sodoudi[1*]

1 Institute of Meteorology, Freie Universität Berlin, Berlin, Germany

2 Department of Geological and Atmospheric Sciences, Iowa State University, Ames, USA

3 Forestry Experiment Center of North China, Chinese Academy of Forestry, Beijing, China

Abstract

Reliable quantification of urban heat island (UHI) can contribute to the effective evaluation of potential heat risk. Traditional methods for the quantification of UHI intensity (UHII) using pairs-measurements are sensitive to the choice of stations or grids. In order to get rid of the limitation of urban/rural divisions, this paper proposes a new approach to quantify surface UHII (SUHII) using the relationship between MODIS land surface temperature (LST) and impervious surface areas (ISA). Given the footprint of LST measurement, the ISA was regionalized to include the information of neighborhood pixels using a Kernel Density Estimation (KDE) method. Considering the footprint improves the LST-ISA relationship. The LST shows highly positive correlation with the KDE regionalized ISA (ISA_{KDE}). The linear functions of LST are well fitted by the ISA_{KDE} in both annual and daily scales for the city of Berlin. The slope of the linear function represents the increase in LST from the natural surface in rural regions to the impervious surface in urban regions, and is defined as SUHII in this study. The calculated SUHII show high values in summer and during the day than in winter and at night. The new method is also verified using finer resolution Landsat data, and the results further prove its reliability.

1. Introduction

Urban areas show higher temperature than the surrounding rural areas, which is well known as Urban Heat Island (UHI) effect. Since its first observation by Howard in London (Mills, 2008), UHI phenomenon has been widely reported in different sized cities (e.g. Arnfield, 2003; Zhang et al., 2010; Zhou et al., 2017). Warmer air caused by UHI increases heat load stress of urban residents, potentially raising the threat of mortality (e.g. Tan et al., 2010;

Constantinescu et al., 2016). Meanwhile, higher temperature increases energy consumption and associated greenhouse gas emissions due to the use of air conditioning (e.g. Zhou and Gurney, 2010; Zhou et al., 2012). Under the background of fast urbanization (e.g. Kuang et al., 2013, 2016b) and global change (e.g. Grimm et al., 2008), residential living in cities is suffering from higher risk of heat wave (e.g. Zhou et al., 2014, 2015; Yang et al., 2017). Concerning the increasing possible hazards caused by UHI, more and more attention has been paid to the studies of UHI (Inouye, 2015; McDonnell and MacGregor-Fors, 2016; Lee et al., 2015).

Accurate quantification of UHI can help to efficiently evaluate the potential heat risk and to guide the city management and development for government and city planners. Urban heat island intensity (UHII), the difference in temperature between urban and surrounding rural regions, is the classical indicator to quantitatively describe UHI effect (Rizwan et al., 2008; Stewart, 2011). Traditionally, the detection of UHII is conducted at two fixed in-situ stations, one in urban and the other in rural regions (e.g.Yang et al., 2013; Earl et al., 2016). Similarly, the study of the surface UHII (SUHII) using remote sensing data is conducted over selected pixels that are located in the urban and rural regions, separately (e.g. Stewart, 2011). The estimation of UHII (SUHII) relies on the definitions of urban and rural stations or pixels (e.g. Roth et al., 1989; Azevedo et al., 2016; Du et al., 2016). However, urban regions are strongly affected by human activities with high heterogeneity over the urban surface, and even the surrounding rural areas may have different ecosystems (Buyantuyev and Wu, 2010; Cadenasso et al., 2007). The urban-rural dichotomy alone cannot sufficiently guide the choice of the stations (Stewart and Oke, 2012). Schwarz et al. (2011) compared eleven approaches for quantifying SUHII with MODIS land surface temperatures for European cities, and found that the calculated SUHIIs using different rural pixels showed weak correlations. The different definitions of the urban/rural regions make the intercomparison study of UHII among different cities challenging. Stewart (2011) argued that previous UHI studies that used two stations measurements are often not comparable because of the different definitions of the measurement stations and the lack of the crucial description of these stations. On the other hand, fixed stations or pixels only represent the local micro-climate around these stations or

pixels (Oke, 2006). Limited measurements only reflect parts of the characteristics of UHI (SUHI), and cannot identify the spatial variation and the structure of UHI within a whole city, especially for the cities which have multiple UHI centers (e.g. Li and Yin, 2013; Dou et al., 2015). The shape of cities could significantly influence the amplitude of UHI (Zhang et al., 2012; Zhou et al., 2017). To overcome the problems mentioned above, a promising way for the quantification of UHII (SUHII) should try to get rid of the limitation of urban/rural divisions, and consider the comprehensive conditions of cities by integrating the urban surface properties.

Land use change caused by urbanization is the primary driving factor of UHI (e.g. Cheval and Dumitrescu, 2015; Du et al., 2016; Li et al., 2017). The lower albedo and higher sealing degree of urban areas significantly alter the surface energy budget and lead to higher temperature than rural areas (Oke, 1982, 1988; Kuang et al., 2015a, 2015b). Near surface temperatures are closely related to urban indicators, such as Impervious Surface Area (ISA). Yuan and Marvin (2007) found that there was a strong linear relationship between LST and ISA for all seasons in Minnesota. Rajasekar and Weng (2009) pointed out that the areas with high heat signatures had a strong correlation with impervious surfaces in central Indiana. Imhoff et al. (2010) concluded that ISA was the primary driver for the increase in temperature, explaining 70% of the total variance in LST for 38 the most populous cities combined in the continental United States. Zhang et al. (2010) pointed out that ~60% of the total LST variance was explained by ISA for urban settlements within forests at mid to high latitudes globally. Li et al. (2011) reported a strong positive relationship between LST and ISA in Shanghai. Schatz and Kucharik (2014) found that ISA within the footprint of measurement stations was the dominant driver of air temperature and accounted for 74% and 80% of the explained spatial variation of the air temperature at night and during the day, respectively, in Madison, Wisconsin. Kuang et al. (2017) found that the highly dense impervious surface areas significantly increased land surface temperature. Wang et al. (2017) found that ISA was responsible for 31%–38% and 49%–54% of air temperature variability during the day and at night, respectively in Beijing. Compared with UHII, SUHII is usually more dependent on ISA. This is because that the land cover is the single most dominant factor of LST, while the air

temperature is affected by land cover, air advection and anthropogenic heat emission, together (Azevedo et al., 2016). To summer up, as a good indicator of urban land use, ISA could reflect the spatial pattern of UHI (SUHI) well. The relationship between temperature and ISA can be a potential powerful tool for the quantification of UHII (SUHII).

The temperature at each site is also affected by the surrounding environment (Rannik et al., 2000). There is a footprint for the temperature measurement (Oke, 2006). The measured temperature is related to the overall land use information within the footprint. Schatz and Kucharik (2014) and Wang et al. (2017) considered the footprint when examining the relationship between in-situ air temperature and ISA. As for the remote sensing, there is a mismatch between the observation results and its ground source, especially for the mixed pixels over heterogeneous areas, due to the variation of the view zenith angles and gridding processes. Campagnolo and Montano (2014) found that the width of the ground-projected instantaneous fields of view (IFOV) of MODIS products was larger than the nominal resolutions, and increased with the view zenith angles. The IFOV errors also exist in the Lansat data, especially in the thermal band (Lee et al., 2004). The satellite observation result in each pixel also contains information from neighboring pixels. Townshend et al. (2000) found that parts of the signal in MODIS pixels come from the surroundings. Peng et al. (2015) found that the size of the signal source of MODIS pixels is larger than the nominal resolution of the pixel. As thus, it is necessary to consider the influence of the footprint of remote sensing observation when study LST-ISA relationship.

This paper comes up with an approach to calculate SUHII based on the linear relationship between LST and ISA. Given the footprint of LST measurement, the ISA was regionalized to include the information of neighborhood pixels within the footprint using a Kernel Density Estimation (KDE) method. The linear regression function of LST was fitted using the KDE regionalized ISA (ISA_{KDE}). The regression slope of the fitted function was used as SUHII. The temporal variations of the calculated SUHII of Berlin in 2010 were investigated. In addition, the new developed ISA_{KDE} was compared with the raw ISA in terms of the fitted functions of LST and the calculated SUHII. The goal of this paper is to develop a promising approach for the quantification of SUHII.

2. Study area, data, and methodology

2.1. Study area

The study area is Berlin, the capital city of Germany. Berlin (52.34°–52.68° N, 13.10°–13.77° E) is located in Northeast Germany with a flat topography (34–122 m, altitude), and covers an area of about 900 km^2. According to a report in the year of 2015 of the Statistical Office of Berlin-Brandenburg (https://www.statistik-berlin-brandenburg.de), Berlin has ~3.6 million inhabitants, with one third living in the inner city in an area of about 88 km^2. It is the second most populous city in the European Union. Fig. 1 shows the spatial pattern of CORINE land cover (Feranec et al., 2007) version 2012 in the study area. Berlin is an urbanized region with about 35% built-up areas. In addition, transportation and infrastructure areas cover about 20% of the city. Berlin's built-up areas create a microclimate with noticeable urban heat island effects, leading to a higher potential heat stress risk in the central inner-city areas (Dugord et al., 2014).

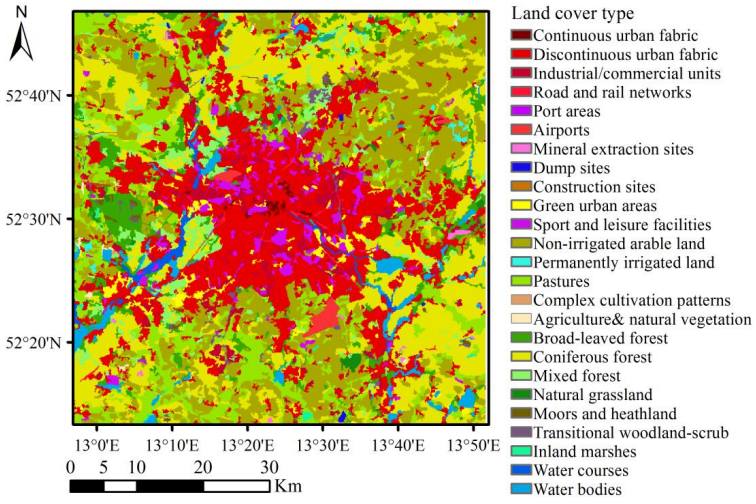

Fig. 1. Spatial pattern of the land cover in the study area.

Berlin has a temperate maritime climate with a mean annual temperature of 9.5 °C and annual precipitation of 591 mm (data based on the German Meteorological Office Dahlem station measurements in the 30-years period of 1981–2010). Affected by the prevailing westerlies and abundant water vapor from Atlantic, Berlin has a windy and cloudy climate (Kottek et al., 2006). Fig. 2 exhibits the seasonal variations of the cloud fraction, wind speed, and precipitation in 2010. Most of the winter days were cloudy with more than half of the sky

covered by clouds, while a lot of the summer days had clear skies. The winter days had stronger winds compared to the summer days. The precipitation was not very concentrated. More than half of the days had precipitation larger than 0.1 mm/d, and almost one-third of the days had precipitation larger than 1.0 mm/d. Although the intensity of the precipitation was not strong, the frequency was high. Most of the typical weather for UHI with few clouds and calm wind occurred in summer.

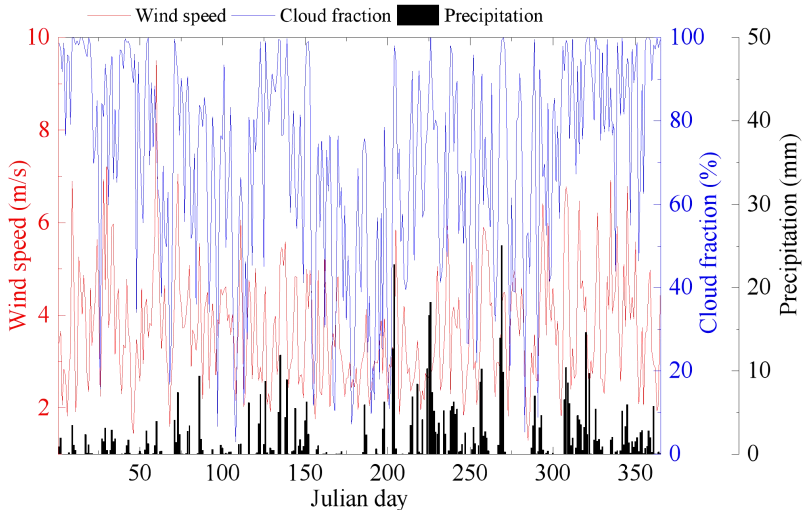

Fig. 2. Seasonal variations of cloud fraction (blue curve), wind speed (red curve), and precipitation (black curve) in 2010 for Berlin.

2.2. LST data

Daily MODIS LST products (MOD11A1&MYD11A1) collection 005 with 1000 m resolution grids in 2010 were used in this study (Coll et al., 2009). MODIS products have high temporal resolution, four observations per day. Moreover, MODIS LST data have high quality. Wan (2008) reported that the accuracy of MODIS LST product (collection 5) is better than 1 K in most cases. Rigo et al. (2006) reported an accuracy of MODIS LST < 5%, even in urban environments. The freely available data are easy to access. MODIS LST data have been widely used to study SUHI in different regions, such as Europe (e.g. Schwarz et al., 2011; Azevedo et al., 2016), Asia (e.g. Kuang et al., 2015a, 2015b), and North America (e.g. Zhang et al., 2014; Hu and Brunsell, 2015; Hu et al., 2016).

Affected by the variation in sensing geometry of the MODIS instruments, the effective

signal source is larger than the size of a MODIS pixel. Wolfe et al. (2002) estimated that the width of the instantaneous field of view of the MODIS observation cells reached approximately 2.0 times and 4.8 times the nadir resolution in the track and scan directions at the scan edge. Campagnolo and Montano (2014) found that in near optimal locations, the effective resolution of the 250 m MODIS gridded products varied between 344 and 835 m along rows and between 292 and 523 m along columns, respectively.

Two MODIS sensors are mounted on the Terra and Aqua satellites, separately. Every day, the Aqua satellite passed over Berlin at UTC time around 11:50 and 01:20, and the Terra satellite passed over Berlin at UTC time around 20:50 and 10:20. As for the MODIS daily LST images, there is slight difference in the observation time among the pixels, around 9 & 13 min for the two MOD images and 9 & 14 min during the study period. Special care needs to be taken into this problem during the interpretation of the results. Clouds absorb the longwave radiation from the earth surface, and then block the observation of LST (Williamson et al., 2013). Here, the cloud-covered pixels are filtered out for each image. The images with too much missing pixels, in particular within urban regions, cannot show the real feature of SUHII well. Meanwhile, too many clouds could weaken UHI effect (Morris et al., 2001). In this study, only the images having >90% of valid pixels within both the study areas and the urban areas (ISA larger than 25%) are chosen for analysis. Berlin has a cloudy climate. Most days are cloudy days, especially in winter (Fig. 2). Eventually, a total of 47, 34, 76 and 61 images at four observation times 10:20, 11:50, 20:50, and 01:20 are kept. The mean LST for the whole year, summer (May to September) and winter (October to April) are calculated using these selected images.

2.3. ISA data

High Resolution Layer imperviousness product version 2012 from Copernicus Land Monitoring Service Pan-European Component (http://land.copernicus.eu/pan-european) was applied in this study. HRL products are produced from multi-source high resolution satellite imagery through a combination of automatic processing and interactive rule based classification (Lefebvre et al., 2013). The imperviousness shows the percentage of artificial impervious cover (0–100%), referring to the built-up areas that are characterized by the

substitution of the original natural land cover or water surface with an artificial surface (Langanke, 2013). Copernicus provides ISA products at both 20 m and 100 m resolution. The accuracy of the data was accessed based on a stratified systematic sampling approach using the EUROSTAT Land Use/Cover Area from statistical Survey sampling frame (Sannier et al., 2016). The results suggested that the Copernicus ISA data reached or even exceeded the required level of accuracy with <10–15% error for both omission and commission errors. This accuracy is similar to the other studies (Kuang et al., 2016a). To make ISA match with LST in grids, the nearest approach was applied to re-sample the ISA data from the resolution of 100 m to 1000 m on the platform of ArcGIS.

2.4. Regionalization of ISA using a kernel density estimation method

Land surface temperature measurement over each pixel has a footprint due to the adjacency effect (Justice et al., 1998). The measurements data are not only affected by the surface of corresponding pixel, but also affected by the surrounding pixels. In order to take the influence of the footprint on the LST measurement into account, the ISA was regionalized using a Kernel Density Estimation (KDE) method. As one of the most well-established spatial techniques, KDE method could calculate the contribution of the surrounding points. The density (f_{KDE}) of a specific point (x_0) was calculated as the sum of the weights of neighbor points (x_i) within a circular neighbor areas as follows

$$f_{KDE}(x_0) = \frac{1}{n}\sum_{i=1}^{n} K\left(\frac{x_0 - x(i)}{r}\right) \quad (1)$$

where r is the kernel radius and controls the size of the circular neighborhoods around x_0. K is the kernel function and controls the weight of the neighbor points.

In this paper, the KDE calculation was conducted on the platform of ArcGIS. Firstly, the raster image of ISA was converted to point feature using the function of ‘Raster to Point’ under the toolbox ‘Conversion Tools’. Then the function of ‘Kernel Density’ under the toolbox of ‘Spatial Analyst Tools’ was used to calculate the density of each point in a neighborhood around each output raster cell with a resolution of 1000 m. During this process,

a smoothly curved surface (kernel surface) is fitted over a circular neighborhood of each point based on quartic kernel function (Silverman, 1986). The surface value is largest at the location of the point and decreases with increasing distance from the point, reaching zero at the border of the circular neighborhood. The density at each output raster cell is calculated by adding the values of all the kernel surfaces where they overlay the raster cell center. Then the f_{KDE} were normalized to the range of 0 to 100% as follows

$$ISA_{KDE} = \frac{f_{KDE} - \min(f_{KDE})}{\max(f_{KDE}) - \min(f_{KDE})} \times 100\% \quad (2)$$

The kernel radius could affect the KDE calculation results (Anderson, 2009; Thakali et al., 2015). Based on the calculation process of the KDE method, the kernel radius should be larger than the distance between the centers of two neighbor pixels (value of the spatial resolution of the pixels, 1000 m). Meanwhile, the largest radius should be b4.8 times (4800 m) the nadir resolution of MODIS LST data based on the study of Wolfe et al. (2002). In order to find out the optimal kernel radius, a sensitivity test was conducted using kernel radius ranging from 1500 m to 5000 m with an interval of 500 m. The LST shows best relationship with KDE regionalized ISA using kernel radius of 3000 m. The details of the sensitivity study are discussed in Section 4.1.

2.5. Quantification of SUHII

The change of land use from the natural to the sealing surface is the dominant reason for SUHI. Usually, the temperature increases with the increase in ISA from rural to urban regions, presenting positive linear trend (e.g. Yuan and Marvin, 2007; Schatz and Kucharik, 2014, 2015). A linear regression function of LST can be fitted using ISA (Fig. 3). The slope of the fitted function refers to the increase of LST versus ISA increasing from 0% to 100%. The regression slope can be used to define SUHII, if a good regression function is fitted. In this study, the regionalized ISA_{KDE} is chosen to fit the linear function of LST. Urban surface has high heterogeneity. LST may vary largely among the grids that have similar ISA_{KDE}, due to the difference in material, elements configuration and morphological characteristics (Oke, 2006; Wang et al., 2017). Here, the zonal analysis method was applied referring to Yuan and

Marvin (2007). All the pixels within the study areas were divided into 50 parts with 2% interval of the ISA_{KDE}. Given the sub-interval variation of LST caused by the heterogeneity of urban surface and different ecosystems of the rural surface, the mean values of LST and ISA_{KDE} were calculated within each interval to fit the function of LST. Least square method was applied to fit the linear regression function. The coefficient of determination (R^2) was used to evaluate the accuracy of the fitted function. Water bodies have strong thermal properties, which may skew the trend of LST with the change in ISA (Hu and Brunsell, 2015). Given the large areas of water bodies in the study areas (6.7% based on Corine land cover data), the pixels with more than one-quarter of water bodies areas were excluded during the calculation process.

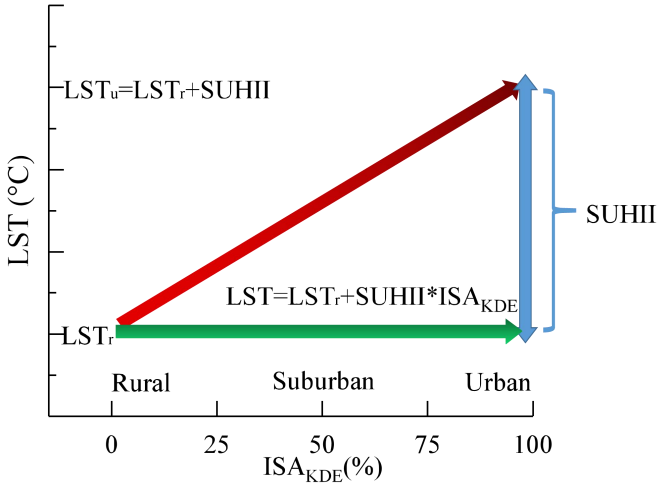

Fig. 3. Schematic diagram of the quantification of SUHII based on the linear regression relationship between LST and ISA_{KDE}. LST_u and LST_r mean the LST in the urban and rural areas.

3. Results

3.1. Spatial patterns of the LST

Fig. 4 shows the spatial variations of the mean LST at the four observation times for the different periods in 2010 for Berlin. The LST within the city center is obviously higher than those within the surrounding rural regions, presenting pronounced surface urban heat island effect. The distribution of high LST areas is corresponding with the urban land cover

distribution shown in Fig. 1. The max-min ranges of the annual mean LST are up to 9.20, 11.24, 6.32 and 8.52 °C at the four observation times (Table 1). The LST shows larger urban-rural difference in daytime and summer than in nighttime and winter.

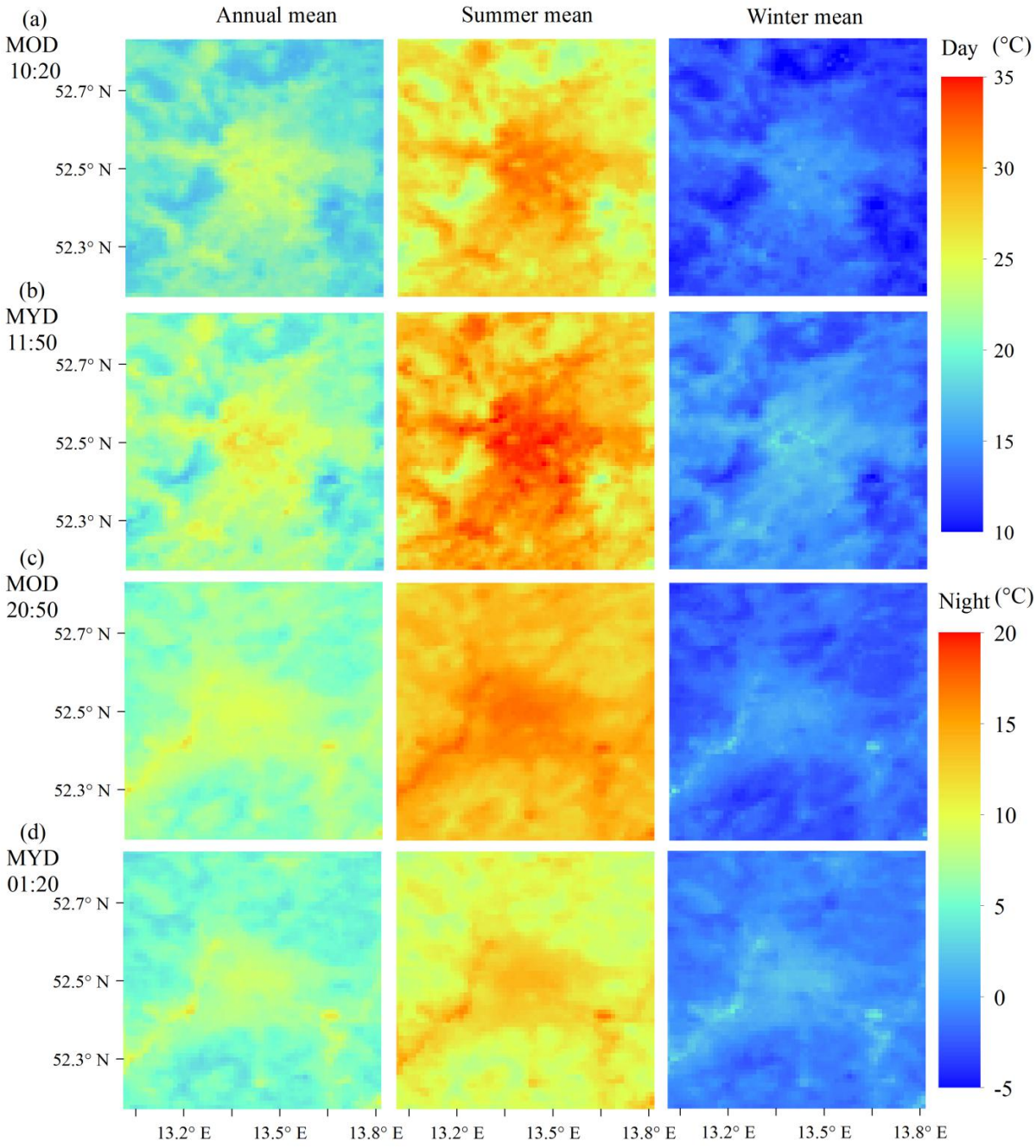

Fig. 4. Spatial distributions of the mean LST in the year of 2010. Three columns represent the mean values during different time periods: whole year (left), summer (middle) and winter (right). Rows of (a), (b), (c) and (d) represent four observation times at 10:20, 11:50, 20:50 and 01:20.

Table 1. Min-Max range of the mean LST (°C) for different periods and times of the day in Berlin.

Observation times	Annual mean	Summer mean	Winter mean
MOD 10:20	9.20	11.09	7.91
MYD 11:50	11.24	12.76	8.88
MOD 20:50	6.32	6.45	5.97
MYD 01:20	8.52	8.35	5.40

3.2. Spatial patterns of the ISA

Fig. 5 shows the spatial distributions of the raw ISA and KDE regionalized ISA (ISA_{KDE}) using the kernel radius of 3000 m for Berlin. Most of the high ISA areas are located in the central regions of the city. In the surrounding rural regions, the pixels with large and small values crossly distribute. The spatial pattern of the ISA is very similar to that of the LST in Fig. 4. The ISA_{KDE} shows a smoother and more continuous distribution, compared with the raw ISA. The Standard Deviation (STD) of the ISA_{KDE} (20.91%) is smaller than that of the raw ISA (25.74%).

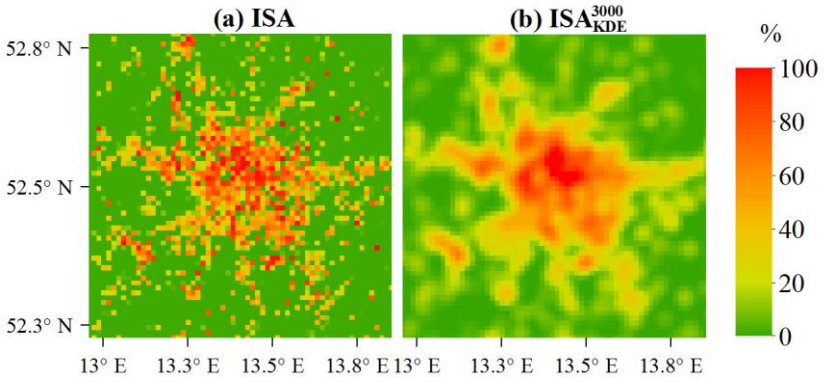

Fig. 5. Spatial distributions of (a) the ISA and KDE regionalized ISA using kernel radius of (b) 1200 and (c) 1400 m. Values of Standard Deviation (STD) of the ISA and ISA_{KDE} are shown at the top right corner.

3.3. Longitudinal variations of the LST versus the ISA_{KDE}

In order to clearly show the spatial configuration of LST-ISA_{KDE}, the mean longitudinal

variations of the LST and ISA_{KDE} are presented in Fig. 6. It shows that as the areas change from rural to inner-city and the land covers change from natural to urban, both the LST and ISA_{KDE} increase. In the city center, the mean ISA_{KDE} are close to 80%, and the temperatures maintain high values, presenting a typical urban heat island phenomenon. Then back from the city center towards rural regions, the LST and ISA_{KDE} decrease with the land covers changing from urban to natural. The longitudinal variation of the LST shows good agreement with the ISA_{KDE}. Daytime and summer show more significant urban-rural variation in LST than nighttime and winter. The grids that are affected by water show lower LST during the day and higher LST at night than other land cover types. These pixels are filtered out when calculating the SUHII.

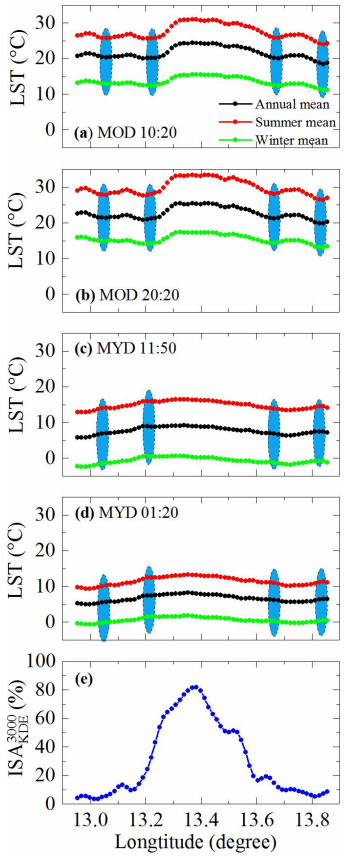

Fig. 6. Longitudinal profiles of (a-d) the mean LST and (e) the ISA_{KDE} across the city within the latitude extent between 52.34° N and 52.68° N (the administrative border of Berlin). The mean values of LST of the whole year (black curve), summer (red curve), and winter (green curve) were calculated, separately. The blue bars indicate the grids that strongly affected by water bodies.

3.4. ISA_{KDE} fitted functions of LST and calculated SUHII in annual scale

Fig. 7 shows the variations of the mean LST versus ISA_{KDE} for the different time periods and observation times. In general, the LST increases smoothly with the increase in ISA_{KDE}, showing a good agreement. ISA_{KDE} accounts for most of the variation in LST. The regression functions of LST were well fitted, with high R^2 for all seasons and times of the day. The values of R^2 for the fitted function of the annual mean LST are up to 0.96, 0.97, 0.97 and 0.98, respectively at the four observation times. The regression functions of LST fitted by ISA_{KDE} can be used to quantify SUHII. The slopes of the fitted functions of LST are defined as the SUHII, and are also shown in Fig. 7. At an annual scale, the values of the SUHII are 5.43, 5.39, 3.58 and 3.95 K at 10:20, 11:50, 20:50 and 01:20, respectively. The SUHII in summer and daytime are higher than that in winter and nighttime. This is consistent with the max-min range of the LST within the study areas in Table 1.

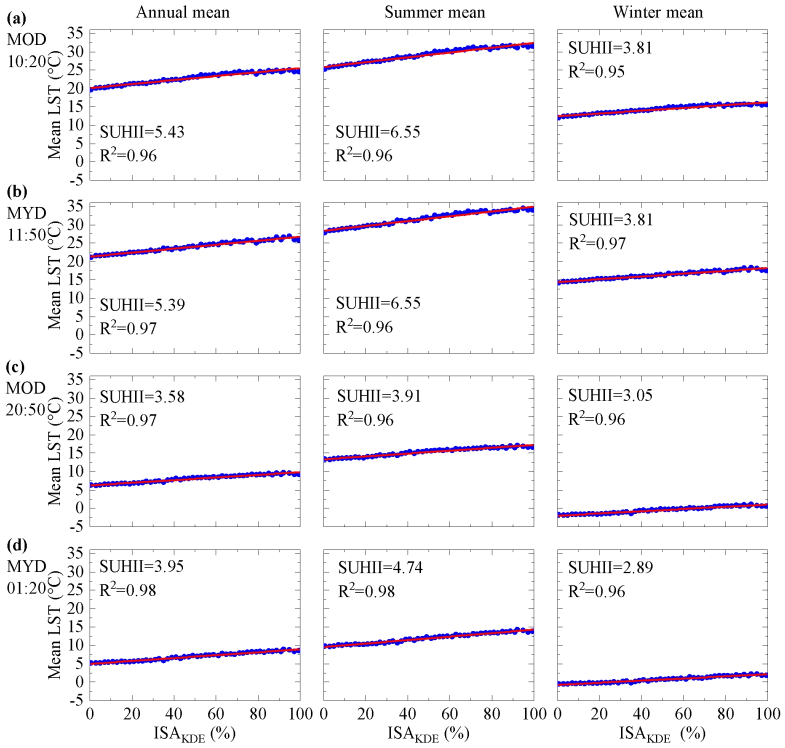

Fig. 7. Variations of the (left) annual mean LST, (middle) summer mean LST and (right) winter mean LST versus ISA_{KDE}. Red lines are the fitted linear regression function. The values of SUHII (K) were calculated using the regression slope. Rows of (a), (b), (c), and (d) represent four observation time at 10:20, 11:50, 20:50 and 01:20. All the correlation are significant here ($p<0.01$).

3.5. Calculated daily SUHII and its temporal variation

The linear regression functions of the daily LST were fitted for each valid image in 2010 using ISA_{KDE}. Most of the LST images show good relationships with ISA_{KDE}. More than three-quarters of the R^2 of the fitted functions are larger than 0.90. Wet surface caused by the precipitation (including rain and snow) before or during the observation time should be the main reason for the weak LST-ISA_{KDE} relationships in some days, and is further discussed in Section 4.4. In general, the ISA_{KDE} can be used to quantify the daily SUHII well when the disturbance of precipitation is removed. The well fitted linear regression functions of LST with R^2 larger than the lower outlier boundary (0.82) were used to calculate daily SUHII. Seasonal variations of the daily SUHII are shown in Fig. 8. Generally, the daily SUHIIs display higher values in summer and lower values in winter. It is consistent with the results at annual scale shown in Fig. 7. The maximum value of the daily SUHII reaches up to 10.32 K happening at 11:50 on Julian day 156, while minimum value is 1.35 K happening at 01:20 on Julian day 274. The mean values are 5.73, 5.38, 4.09 and 4.61 K, respectively, at the four observation times (Table 2). Daytime always shows higher SUHII than nighttime.

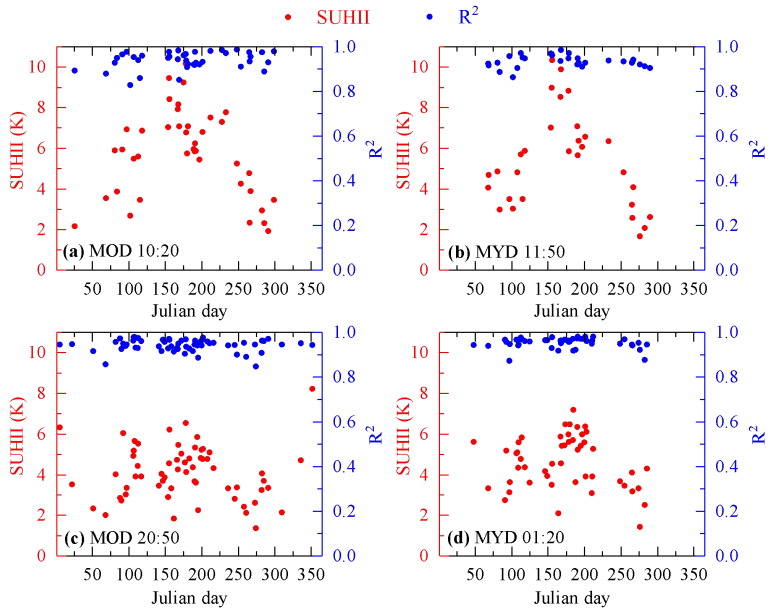

Fig. 8. Seasonal variations of the daily SUHII (red dots) and its corresponding R^2 (blue dots) at four observation time in 2010 over Berlin. Subplots of (a), (b), (c), and (d) represent four observation times.

Table 2. Statistics of daily SUHII (K) calculated using the valid regression functions of LST, with R^2 within the outlier boundary. The upper boundary is 1.5 times of the Interquartile Range (IQR) larger than the 3rd interquartile, while the lower boundary is 1.5 times of IOR lower than the 1st interquartile.

Observation times	Max	1st Interquartile	Median	3rd Interquartile	Min	Mean
MOD 10:20	10.16	7.07	5.88	3.87	1.93	5.73
MYD 11:50	10.33	6.57	5.25	3.49	1.67	5.38
MOD 20:50	8.22	4.95	4.04	3.29	1.35	4.09
MYD 01:20	7.18	5.60	4.56	3.62	1.42	4.61

4. Discussion

4.1. Sensitivity of the quantification of SUHII to kernel radius

In this study, the kernel radius represents the extent of the footprint of the LST measurement over each pixel. The kernel radius could affect the calculation results of KDE method, and then further affect the LST-ISA_{KDE} relationship. In order to obtain the optimal kernel radius for the SUHII calculation, a sensitivity test at annual scale was conducted. The linear functions of the mean LST during different periods were fitted using the kernel radius ranging from 1500 to 5000 m with an interval of 500 m. The R^2 of the fitted functions and the calculated SUHII versus kernel radius are present in Fig. 9. The variations of the R^2 and SUHII with kernel radius show similar trend for the whole year, summer, and winter. The best regression functions of LST with highest R^2 is achieved at radius of 3000 m (3.0 times of the resolution). Either smaller or larger kernel radius would weaken the LST-ISA_{KDE} relationship. That is because when the radius is too small, the KDE results could not contain enough information inside the footprint, while when the radius is too large, the KDE results would contain some noise information and outliers outside the footprint (Thakali et al., 2015). The calculated SUHII is also affected by kernel radius. Larger radius tends to produce higher SUHII when the value was <2000 m. When the radius further increase, the sensitivity of the calculated SUHII to kernel radius disappear.

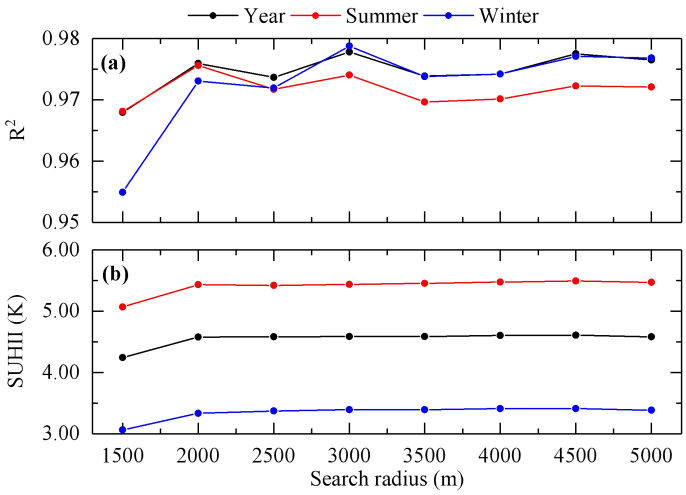

Fig. 9. Variations of (a) R^2 of the fitted functions and (b) the calculated SUHII versus kernel radius. The LST used here are the mean values of the four observation everyday.

4.2. Influence of the regionalization of ISA on the quantification of SUHII

Table 3. Comparison of the R^2 for the fitted functions of LST using ISA_{KDE} and raw ISA.

Observation time	ISA_{KDE}			Raw ISA		
	Year	Summer	Winter	Year	Summer	Winter
MOD 10:20	0.96	0.96	0.95	0.92	0.91	0.91
MYD 11:50	0.97	0.96	0.97	0.90	0.90	0.89
MOD 20:50	0.97	0.96	0.96	0.83	0.84	0.79
MYD 01:20	0.98	0.98	0.96	0.84	0.86	0.79

In order to evaluate the advantage of the newly developed ISA_{KDE} in calculating SUHII, a comparison study between the linear functions of LST fitted by ISA_{KDE} and raw ISA was conducted. Tables 3 and 4 present the R^2 of the fitted functions and calculated SUHII using these two indicators. In general, the functions of LST were better fitted by ISA_{KDE} with higher R^2 for all time periods. ISA only reflects the surface property, and does not include the influence of neighboring pixels on the LST measurements within the footprint. So it cannot perform as well as ISA_{KDE} in terms of the fitting of LST functions. The SUHII calculated using ISA_{KDE} shows larger values than those calculated using raw ISA. Compared with the map of the ISA_{KDE}, the ISA clearly detects the distributions of the peak values among pixels (Fig. 5a). The spatial variation of the ISA_{KDE} is smoother than that of the raw ISA with lower

STD. The urban-rural difference in the ISA_{KDE} is smaller than that of the raw ISA, leading to higher SUHII.

Table 4. Comparison of the SUHII calculated using the slope of the fitted functions of LST using $ISA_{KDE,}$ and raw ISA.

Observation times	ISA_{KDE}			Raw ISA		
	Year	Summer	Winter	Year	Summer	Winter
MOD 10:20	5.43	6.55	3.81	3.23	3.90	2.27
MYD 11:50	5.30	6.55	3.81	3.01	3.79	2.11
MOD 20:50	3.58	3.91	3.05	1.74	2.00	1.38
MYD 01:20	3.95	4.74	2.89	1.83	2.25	1.26

4.3. Validation of the new method using Landsat data

MODIS data can be used to study the synoptic overview and the temporal variation of urban areas (Pu et al., 2006). In this study, MODIS LST achieved good relationships with ISA_{KDE}, and the diurnal and seasonal patterns of the SUHII are analyzed. However, the coarse spatial resolution MODIS data cannot distinguish the fine-scale variation of urban surface, limiting the accurate detection of complex urban thermal environment in detail. Urban surface temperature varies largely in both the city and street scales due to the high heterogeneity of urban surface. Strong sub-pixel variations of temperature even exist within the coarse MODIS pixels. A more accurate study of SUHI demands higher resolution thermal remote sensing data. In order to further examine the reliability of the new method, Landsat data at a 30 m resolution and Copernicus ISA data version 2012 at a 20 m resolution were used to calculate the SUHII. Two Landsat 7 ETM+ images (Fig. 10a, b) were collected from the USGS website (https://earthexplorer.usgs.gov/). The LST was calculated using a mono-window algorithm (Zhang et al., 2006). The ISA data was resampled to 30 m firstly, and then further regionalized using KDE method with a kernel radius of 90 m (3 times resolution of Landsat images referring to the sensitivity analysis results above). The ISA_{KDE} shows a smoother spatial pattern than the raw ISA (Fig. 10c, d). The functions of LST are fitted using the raw ISA and ISA_{KDE}, respectively, and the slopes of the functions are used to calculate the SUHII. Table 5

shows the statistics of the fitted functions and the calculated SUHII. The R^2 of two fitted functions using ISA_{KDE} is larger than those using the raw ISA. Compared with the raw ISA, the ISA_{KDE} better reflects the spatial variation of the Landsat LST. Meanwhile, the STD of ISA_{KDE} (27.67%) is smaller than the raw ISA (31.82%), which leads to larger values of the calculated SUHII using ISA_{KDE}. The difference between the ISA_{KDE} and the raw ISA in fitting the functions of LST and the calculated SUHII using the Landsat data are consistent with those using MODIS data as shown in Tables 3 and 4.

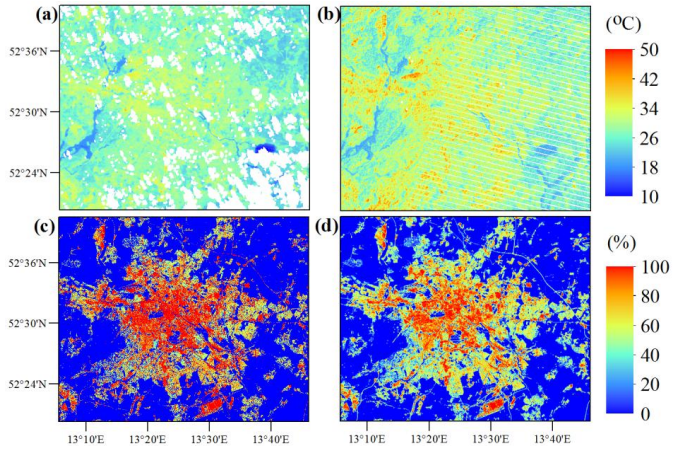

Fig. 10. Spatial patterns of (a and b) the Landsat LST data and (c and d) ISA. The (a) and (b) show the retrieved LST at time 9:53 UTC, 28th April and 9:55 UTC, 9th July, 2010, respectively. The (c) and (d) show the raw ISA and regionalized ISA.

Table 5. Statistics of the fitted functions of the Landsat LST and calculated SUHII.

Image	Indicator	R^2	SUHII (K)
28th, April	ISA	0.84	2.23
	ISA_{KDE}	0.95	4.38
9th, July	ISA	0.92	4.13
	ISA_{KDE}	0.97	6.83

4.4. Influence of precipitation on the new method application

Precipitation could alter surface moisture, and decrease the urban-rural difference in both albedo and water availability, weakening the LST-ISA_{KDE} relationship. The foundation of the

hypothesis of this new method shown in the Fig. 3 would be broken by precipitation. Fig. 11 shows the box plots of the R^2 of the fitted functions of daily LST under rainy and non-rainy conditions. When precipitation occurs, the R^2 shows a lot of small values (Fig. 11a). The 25th percentile and lower boundary of outliers are only 0.77 and 0.48. When no precipitation occurs, the R^2 shows high values, with the 25th percentile and the lower boundary of outliers of 0.91 and 0.84, respectively. Here only the precipitation happened within 12 h before observation times are taken into account. Strong precipitation has a longer term impact on the ground moisture. Most of the outliers in Fig. 11b happen due to the strong precipitation before 12 h of the observation times. In addition, the evaporation and the melting of snow in winter is very slow (Li et al., 2016). The snow covering could last long time and weaken the UHI effect, which leads to parts of the outliers in Fig. 11b.

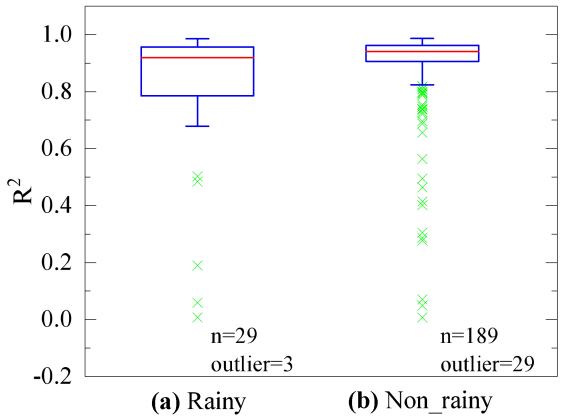

Fig. 11. Box plots of R^2 for the fitted functions under (a) rainy and (b) non-rainy conditions within the 12 hours before the observation times. Top and bottom of the blue boxes represent the 75th and 25th percentile and red horizontal line within the box indicates the median. Short top and bottom bars outside the boxes are the boundaries of upper and lower outlier defined by 1.5 IQR, green crosses are the outliers.

5. Conclusions and outlook

This paper proposed a new approach to quantify the SUHII by fitting the linear functions of LST using ISA. Given the footprint of LST measurement, the ISA was regionalized using a Kernel Density Estimation approach. The spatial variation of the LST in Berlin region displayed pronounced SUHI characteristic. The spatial patterns of the LST and ISA_{KDE} were

similar. The linear functions of LST were well fitted using ISA_{KDE} in both annual and daily scale. The slope of the linear regression was defined as SUHII. The annual mean SUHII were 5.72, 5.38, 4.09 and 4.61 K at UTC time 10:20, 11:50, 20:50 and 01:20, respectively. The LST showed higher correlation with ISA_{KDE} than with raw ISA across all time periods. The reliability of the new method was further verified using fine resolution Landsat data. Precipitation could weaken the dependence of LST on surface imperviousness and then influence the calculation of SUHII. The practical application of the new method should avoid rainy days.

The well fitted linear functions of LST using ISA_{KDE} provide a promising approach to quantify the SUHII using remote sensing data. Compared with the traditional approach of calculating the deficit of measurements at urban and rural stations or pixels, the new approach could avoid the bias caused by the choice of the stations or pixels. This method can be easily applied in other cities, which makes the comparisons of SUHI among different cities possible. Nevertheless, it should be noted that the hypothesis of the new method is that LST increases along with ISA. This hypothesis is true for most cities in biomes dominated by forests and grasslands. However, for the cities in desert environments, the LST's response to ISA presented U-shaped horizontal gradient (e.g. Imhoff et al., 2010; Zhang et al., 2010). So this method does not work for the cities in the arid or desert environment. Compared with SUHII, UHII calculated by air temperature is more concerned in term of heat stress. Usually SUHII is larger than UHII. This study only focuses on the quantification of SUHII. As for the feasibility of this method for quantifying UHII, a further study is needed in the next step. In addition, there is a slight difference in the acquired time among the pixels within the images of daily MODIS LST products. This may affect the result to some extent and can be investigated in future studies.

Acknowledgements

This research is supported by the China Scholarship Council, FUBright Mobility Allowances for Research Stays promoted by the German Academic Exchange Service (DAAD)-Dahlem Research School of Freie Universität Berlin, Mobility Allowance for Junior Research Stays from University Alliance for Sustainability promoted by Freie Universität Berlin. The authors

thank the Beijing Office of Freie Universität Berlin. Special thanks go to Dr. Hamid Taheri Shahraiyni for help in processing remote sensing data and Patricia Margerison for proofreading this manuscript.

References

Anderson, T.K., 2009. Kernel density estimation and K-means clustering to profile road accident hotspots. Accid. Anal. Prev. 41 (3), 359–364.

Arnfield, A.J., 2003. Two decades of urban climate research: a review of turbulence, exchanges of energy and water, and the urban heat island. Int. J. Climatol. 23, 1–26.

Azevedo, J.A., Chapman, L., Muller, C.L., 2016. Quantifying the daytime and night-time urban heat island in Birmingham, UK: a comparison of satellite derived land surface temperature and high resolution air temperature observations. Remote Sens. 8:153. https://doi.org/10.3390/rs8020153.

Buyantuyev, A., Wu, J.G., 2010. Urban heat islands and landscape heterogeneity: linking spatiotemporal variations in surface temperatures to land-cover and socioeconomic patterns. Landsc. Ecol. 25 (1), 17–33.

Cadenasso, M.L., Pickett, S.T., Schwarz, K., 2007. Spatial heterogeneity in urban ecosystems: reconceptualizing land cover and a framework for classification. Front. Ecol. Environ. 5 (2), 80–88.

Campagnolo, M.L., Montano, E.L., 2014. Estimation of effective resolution for daily MODIS gridded surface reflectance products. IEEE Trans. Geosci. Remote Sens. 52 (9), 5622–5632.

Cheval, S., Dumitrescu, A., 2015. The summer surface urban heat island of Bucharest (Romania) retrieved from MODIS images. Theor. Appl. Climatol. 121, 631–640.

Coll, C., Wan, Z., Galve, J.M., 2009. Temperature-based and radiance-based validations of the V5 MODIS land surface temperature product. J. Geophys. Res. Atmos. 114 (20).

Constantinescu, D., Cheval, S., Caracaş, G., Dumitrescu, A., 2016. Effective monitoring and

warning of Urban Heat Island effect on the indoor thermal risk in Bucharest (Romania). Energ. Buildings 127, 452–468.

Dou, J., Wang, Y., Bornstein, R., Miao, S., 2015. Observed spatial characteristics of Beijing urban climate impacts on summer thunderstorms. J. Appl. Meteorol. Climatol. 54 (1), 94–105.

Du, H., Wang, D., Wang, Y., Zhao, X., Qin, F., Jiang, H., Cai, Y., 2016. Influences of land cover types, meteorological conditions, anthropogenic heat and urban area on surface urban heat island in the Yangtze River Delta Urban Agglomeration. Sci. Total Environ. 571, 461–470.

Earl, N., Simmonds, I., Tapper, N., 2016. Weekly cycles in peak time temperatures and urban heat island intensity. Environ. Res. Lett. 11 (7), 074003.

Feranec, J., Hazeu, G., Christensen, S., Jaffrain, G., 2007. Corine land cover change detection in Europe (case studies of the Netherlands and Slovakia). Land Use Policy 24 (1), 234–247.

Grimm, N.B., Faeth, S.H., Golubiewski, N.E., Redman, C.L., Wu, J., Bai, X., Briggs, J.M., 2008.

Global change and the ecology of cities. Science 319, 756–760.

Hu, L., Brunsell, N.A., 2015. A new perspective to assess the urban heat island through remotely sensed atmospheric profiles. Remote Sens. Environ. 158, 393–406.

Hu, L., Monaghan, A., Voogt, J.A., Barlage, M., 2016. A first satellite-based observational assessment of urban thermal anisotropy. Remote Sens. Environ. 181, 111–121.

Imhoff, M.L., Zhang, P., Wolfe, R.E., Bounoua, L., 2010. Remote sensing of the urban heat island, effect across biomes in the continental USA. Remote Sens. Environ. 114 (3), 504–513.

Inouye, D.W., 2015.The next century of ecology. Science 349, 565.

Justice, C.O., Vermote, E., Townshend, J.R., Defries, R., Roy, D.P., Hall, D.K., Salomonson,

V.V., Privette, J.L., Riggs, G., Strahler, A., 1998. The moderate resolution imaging spectroradiometer (MODIS): land remote sensing for global change research. IEEE Trans. Geosci. Remote Sens. 36, 1228–1249.

Kottek, M., Grieser, J., Beck, C., Rudolf, B., Rubel, F., 2006. World map of the Köppen-Geiger climate classification updated. Meteorol. Z. 15 (3), 259–263.

Kuang, W., Liu, J., Zhang, Z., Lu, D., Xiang, B., 2013. Spatiotemporal dynamics of impervious surface areas across China during the early 21st century. Chin. Sci. Bull. 58 (14), 1691–1701.

Kuang, W., Liu, Y., Dou, Y., Chi, W., Chen, G., Gao, C., Yang, T., Liu, J., Zhang, R., 2015a. What are hot and what are not in an urban landscape: quantifying and explaining the land surface temperature pattern in Beijing, China. Landsc. Ecol. 30 (2), 357–373.

Kuang, W., Dou, Y., Zhang, C., Chi, W., Liu, A., Liu, Y., Zhang, R., Liu, J., 2015b. Quantifying the heat flux regulation of metropolitan land-use/land-cover components by coupling remote sensing-modelling with in situ measurement. J. Geophys. Res. Atmos. 120 (1), 113–130.

Kuang, W., Chen, L., Liu, J., Xiang, W., Chi, W., Lu, D., Yang, T., Pan, T., Liu, A., 2016a. Remote sensing-based artificial surface cover classification in Asia and spatial pattern analysis. Sci. China Earth Sci. 9 (59), 1720–1737.

Kuang, W., Liu, J., Dong, J., Chi, W., Zhang, C., 2016b. The rapid and massive urban and industrial land expansions in China between 1990 and 2010: a CLUD-based analysis of their trajectories, patterns and drivers. Landsc. Urban Plan. 145, 21–33.

Kuang, W., Yang, T., Liu, A., Zhang, C., Lu, D., Chi, W., 2017. An EcoCity model for regulating urban land cover structure and thermal environment: taking Beijing as an example. Sci. China Earth Sci. 60 (6), 1098–1109.

Langanke, T., 2013. GIO Land (GMES/Copernicus Initial Operations Land) High Resolution Layers (HRLs)—Summary of Product Specifications. European Environment Agency.

Lee, D.S., Storey, J.C., Choate, M.J., Hayes, R.W., 2004. Four years of Landsat-7 on-orbit

geometric calibration and performance. IEEE Trans. Geosci. Remote Sens. 42 (12), 2786–2795.

Lee, X., Gao, Z., Zhang, C., Chen, F., Hu, Y., Jiang, W., Liu, S., Lu, L., Sun, J., Wang, J., Zeng, Z., Zhang, Q., Zhao, M., Zhou, M., 2015. Priorities for boundary layer meteorology research in China. Bull. Am. Meteorol. Soc. 96 (9), 149–151.

Lefebvre, A., Beaugendre, N., Pennec, A., Sannier, C., Corpetti, T., 2013. Using data fusion to update built-up areas of the 2012 European High-Resolution Layer Imperviousness. Proceedings of the 33rd EARSeL Symposium Conference, Matera, Italy. 36, p. 321328.

Li, C.F., Yin, J., 2013. A study on urban thermal field of Shanghai using multi-source remote sensing data. J. Indian Soc. Remote Sens. 41 (4), 1009–1019.

Li, J., Song, C., Cao, L., Zhu, F., Meng, X., Wu, J., 2011. Impacts of landscape structure on surface urban heat islands: a case study of Shanghai, China. Remote Sens. Environ. 115 (12), 3249–3263.

Li, H., Wang, A., Guan, D., Jin, C., Wu, J., Yuan, F., Shi, T., 2016. Empirical model development for ground snow sublimation beneath a temperate mixed forest in Changbai Mountain. J. Hydrol. Eng. 21(11) https://doi.org/10.1061/(ASCE)HE.1943-5584.0001415.

Li, H., Wolter, M., Wang, X., Sodoudi, S., 2017. Impact of land cover data on the simulation of urban heat island for Berlin using WRF coupled with bulk approach of Noah-LSM. Theor. Appl. Climatol. https://doi.org/10.1007/s00704-017-2253-z.

McDonnell, M.J., MacGregor-Fors, I., 2016. The ecological future of cities. Science 352, 936–938.

Mills, G., 2008. Luke Howard and the climate of London. Weather 63 (6), 153–157.

Morris, C., Simmonds, I., Plummer, N., 2001. Quantification of the influences of wind and cloud on the nocturnal urban heat island of a large city. J. Appl. Meteorol. 40, 169–182.

Oke, T.R., 1982. The energetic basis of the urban heat island. Q. J. R. Meteorol. Soc. 108,

1–24.

Oke, T.R., 1988.The urban energy balance. Prog. Phys. Geogr. 12, 471–508.

Oke, T.R., 2006. Instruments and observing methods: Report No. 81: initial guidance to obtain representative meteorological observations at urban sites. World Meteorological Organization, WMO/TD (1250).

Peng, J., Liu, Q., Wang, L., Liu, Q., Fan, W., Lu, M., Wen, J., 2015. Characterizing the pixel footprint of satellite albedo products derived from MODIS reflectance in the Heihe River Basin, China. Remote Sens. 7 (6), 6886–6907.

Pu, R., Gong, P., Michishita, R., Sasagawa, T., 2006. Assessment of multi-resolution and multi-sensor data for urban surface temperature retrieval. Remote Sens. Environ. 104 (2), 211–225.

Rajasekar, U., Weng, Q.H., 2009. Urban heat island monitoring and analysis using a nonparametric model: a case study of Indianapolis. ISPRS J. Photogramm. Remote Sens. 64 (1), 86–96.

Rannik,Ü., Aubinet,M., Kurbanmuradov,O., Sabelfeld, K.K., Markkanen, T., Vesala, T., 2000. Footprint analysis for measurements over a heterogeneous forest. Bound.-Layer Meteorol. 97(1), 137–166.

Rigo, G., Parlow, E., Oesch, D., 2006. Validation of satellite observed thermal emission with in-situ measurements over an urban surface. Remote Sens. Environ. 104 (2), 201–210.

Rizwan, A.M., Dennis, L.Y.C., Liu, C., 2008. A review on the generation, determination and mitigation of Urban Heat Island. J. Environ. Sci. 20, 120–128.

Roth, M., Oke, T.R., Emery, W.J., 1989. Satellite-derived urban heat islands from three coastal cities and the utilization of such data in urban climatology. Int. J. Remote Sens. 10 (11), 1699–1720.

Sannier, C., Gallego, J., Dahmer, J., Smith, G., Dufourmont, H., Pennec, A., 2016. Validation of Copernicus high resolution layer on imperviousness degree for 2006, 2009 and 2012.

Proceedings of the International Symposium on Spatial Accuracy Assessment in Natural Resources and Environmental Sciences, Montpellier, France, pp. 5–8.

Schatz, J., Kucharik, C.J., 2014. Seasonality of the urban heat island effect in Madison, Wisconsin. J. Appl. Meteorol. Climatol. 53 (10), 2371–2386.

Schatz, J., Kucharik, C.J., 2015. Urban climate effects on extreme temperatures in Madison, Wisconsin, USA. Environ. Res. Lett. 10 (9), 094024.

Schwarz, N., Lautenbach, S., Seppelt, R., 2011. Exploring indicators for quantifying surface urban heat islands of European cities with MODIS land surface temperatures. Remote Sens. Environ. 115 (12), 3175–3186.

Silverman, B.W., 1986. Density Estimation for Statistics and Data Analysis. Chapman and Hall, New York.

Stewart, I.D., 2011. A systematic review and scientific critique of methodology in modern urban heat island literature. Int. J. Climatol. 31 (2), 200–217.

Stewart, I.D., Oke, T.R., 2012. Local climate zones for urban temperature studies. Bull. Am. Meteorol. Soc. 93, 1879–1900.

Tan, J., Zheng, Y., Tang, X., Guo, C., Li, L., Song, G., Zhen, X., Yuan, D., Kalkstein, A.J., Li, F., Chen, H., 2010. The urban heat island and its impact on heat waves and human health in Shanghai. Int. J. Biometeorol. 54 (1), 75–84.

Thakali, Lalita, Kwon, T.J., Fu, L., 2015. Identification of crash hotspots using kernel density estimation and kriging methods: a comparison. J. Mod. Transp. 23 (2), 93–106.

Townshend, J.R.G., Huang, C., Kalluri, S.N.V., Defries, R.S., Liang, S., Yang, K., 2000. Be ware

of per-pixel characterization of land cover. Int. J. Remote Sens. 21, 839–843.

Wan, Z., 2008. New refinements and validation of the MODIS land-surface temperature/ emissivity products. Remote Sens. Environ. 112 (1), 59–74.

Wang, K., Jiang, S., Wang, J., Zhou, C., Wang, X., Lee, X., 2017. Comparing the diurnal and

seasonal variabilities of atmospheric and surface urban heat islands based on the Beijing urban meteorological network. J. Geophys. Res. Atmos. 122(4), 2131–2154.

Williamson, S.N., Hik, D.S., Gamon, J.A., Kavanaugh, J.L., Koh, S., 2013. Evaluating cloud contamination in clear-sky MODIS Terra daytime land surface temperatures using ground-based meteorology station observations. J. Clim. 26 (5), 1551–1560.

Wolfe, R.E., Nishihama, M., Fleig, A.J., Kuyper, J.A., Roy, D.P., Storey, J.C., Patt, F.S., 2002. Achieving sub-pixel geolocation accuracy in support of MODIS land science. Remote Sens. Environ. 83, 31–49.

Yang, P., Ren, G., Liu, W., 2013. Spatial and temporal characteristics of Beijing urban heat island intensity. J. Appl. Meteorol. Climatol. 52, 1803–1816.

Yang, X., Leung, L.R., Zhao, N., Zhao, C., Qian, Y., Hu, K., Liu, X., Chen, B., 2017. Contribution of urbanization to the increase of extreme heat events in an urban agglomeration in east China. Geophys. Res. Lett. https://doi.org/10.1002/2017GL074084

Yuan, F., Marvin, E.B., 2007. Comparison of impervious surface area and normalized difference vegetation index as indicators of surface urban heat island effects in Landsat imagery. Remote Sens. Environ. 106 (3), 375–386.

Zhang, J., Wang, Y., Li, Y., 2006. A C++ program for retrieving land surface temperature from the data of Landsat TM/ETM+ band6. Comput. Geosci. 32 (10), 1796–1805.

Zhang, P., Imhoff, M.L., Wolfe, R.E., Bounoua, L., 2010. Characterizing urban heat islands of global settlements using MODIS and nighttime lights products. Can. J. Remote. Sens. 36 (3), 185–196.

Zhang, P., Imhoff, M.L., Bounoua, L., Wolfe, R.E., 2012. Exploring the influence of impervious surface density and shape on urban heat islands in the northeast United States using MODIS and Landsat. Can. J. Remote. Sens. 38 (4), 441–451.

Zhang, P., Bounoua, L., Imhoff, M.L., Wolfe, R.E., Thome, K.J., 2014. Comparison of MODIS land surface temperature and air temperature over the continental USA meteorological stations. Can. J. Remote. Sens. 40 (2), 110–122.

Zhou, Y., Gurney, K., 2010. A new methodology for quantifying on-site residential and commercial fossil fuel CO2emissions at the building spatial scale and hourly time scale. Carbon Manage. 1 (1), 45–56.

Zhou, Y., Weng, Q., Gurney, K.R., Shuai, Y., Hu, X., 2012. Estimation of the relationship between remotely sensed anthropogenic heat discharge and building energy use. ISPRS J. Photogramm. Remote Sens. 67, 65–72.

Zhou, Y., Smith, S.J., Elvidge, C.D., Zhao, K., Thomson, A., Imhoff, M., 2014. A cluster-based method to map urban area from DMSP/OLS nightlights. Remote Sens. Environ. 147, 173–185.

Zhou, Y., Smith, S.J., Zhao, K., Imhoff, M., Thomson, A., Bond-Lamberty, B., Asrar, G.R., Zhang, X., He, C., Elvidge, C.D., 2015. A global map of urban extent from nightlights. Environ. Res. Lett. 10 (5), 054011.

Zhou, B., Rybski, D., Kropp, J.P., 2017. The role of city size and urban form in the surface urban heat island. Sci. Rep. 7, 4791.

Paper III

This article has been published on “Science of the Total Environment”. It is available at https://doi.org/10.1016/j.scitotenv.2018.10.025. This paper was attached below with kind permission from the journal.

Li H., Zhou Y., Wang X., Zhou X., Zhang H., Sodoudi S. Quantifying Urban Heat Island Intensity in the City of Berlin Using WRF/UCM. *Science of the Total Environment* 650:3110-3119.

Author Contributions: Li H. designed the research, conducted the simulation, analyzed the data, and draft the manuscript. Sodoudi S. contributed ideas to the analysis of results, reviewed the manuscript, and supervised the study. Zhou Y. contributed ideas to the research design and the discussion of the results, and reviewed the manuscript. Wang X. and Zhou X. contributed technical support to the simulation and ideas to the discussion of results, and reviewed the manuscript. Zhang H. contributed ideas to the discussion of the results and reviewed the manuscript.

Quantifying Urban Heat Island Intensity and its Physical Mechanism Using WRF/UCM

Huidong Li[1], Yuyu Zhou[2], Xun Wang[1], Xu Zhou[3], Huiwen Zhang[1], Sahar Sodoudi[1*]

1 Institute of Meteorology, Freie Universität Berlin, Berlin, Germany

2 Department of Geological and Atmospheric Sciences, Iowa State University, Ames, USA

3 Key Laboratory of Tibetan Environment Changes and Land Surface Processes, Institute of Tibetan Plateau Research, Chinese Academy of Sciences, Beijing, China

Abstract

Reliable quantification of urban heat island intensity (UHII) is crucial for the evaluation of extreme heat waves and the related heat stress. As a powerful approach for the study of urban climate, numerical models can simulate urban heat island (UHI) in both high spatial and temporal resolutions. However, accurate quantification of UHII using modelling grid data is still a challenge at present, due the different criterions for the selection of urban/rural grids. This study simulates the high-resolution UHI in the city of Berlin using the Weather Research and Forecasting Model coupled with Urban Canopy Module. A new method to quantify UHII, which is based on the fitted linear functions of simulated 2-m air temperature (T_{2m}) using the impervious surface area in WRF grids (ISA_{WRF}), was adopted and evaluated. The simulated T_{2m} matches the observations well, with a correlation coefficient of 0.95 (P<0.01) and RMSE of 1.76 °C. The study area shows a strong UHI at nighttime. The simulated nighttime T_{2m} increases with the increase in the ISA_{WRF}. The linear functions of simulated nighttime T_{2m} against ISA_{WRF} are well fitted. The UHII is calculated as the products of the slopes of fitted functions and the largest ISA_{WRF}. The derived UHII shows U-shaped diurnal variations, with high values at nighttime. The difference of simulated surface temperature and sensible heat flux between the impervious surface and the vegetation surface jointly determines the derived UHII. The large difference of surface temperature and the small difference of sensible heat flux between the impervious and the vegetation surface generate the high UHII at nighttime and vice versa during the daytime. The method of ISA_{WRF}-based function of T_{2m} overcomes

the problems of traditional methods in arbitrary selecting urban/rural grids. It can be used easily to quantify UHII and to do the comparison study of UHII between different cities.

Keyword: urban heat island intensity, impervious surface area, urban parameters, WRF/UCM, Berlin

1 Introduction

The Urban Heat Island (UHI) effect refers to the warmer temperatures in urban areas than in surrounding rural areas, due to urbanization (Rizwan et al. 2008). UHI can strengthen heat waves, increasing the heat load to urban dwellers (Tan et al., 2010). It is projected that rapid urbanization will continue during this century (AAAS, 2016). With more build-up surface being constructed and more people crowding into cities, UHI will become more intense (Yang et al., 2017). Furthermore, climate change will enhance the frequency and intensity of extreme heat waves in the future (e.g. Meehl and Tebaldi, 2004). Urban residents will suffer from a higher risk of heat stress, which has a negative effect on human thermal comfort and heat-related illnesses. The studies on UHI (e.g. spatial and temporal patterns, driving factors, and mitigation strategies) became more important and received a great deal of attention in recent years (Phelan et al., 2015). Among all these topics, accurate quantification of UHI intensity (UHII) is the first step.

Currently, in-situ observation, remote sensing observation, and numerical modelling are the most used approaches for the study of UHI (Mirzaei and Haghighat, 2010). Usually, in-situ observation cannot reflect the spatial pattern of UHI well, due to sparse stations and remote sensing observation is unable to capture the temporal variation of UHI well, due to the low temporal resolution and the disturbance of clouds. Compared to in-situ and remote sensing observations, numerical modelling can be used to study UHI in both high spatial and temporal resolution (San José et al., 2013). Numerical modelling has become a powerful approach for the study of UHI and has been used for the wide studies of UHI, such as investigation of the physical mechanism and drivers of UHI (e.g. Li et al. 2017), the pre-warning of heat waves (e.g. Zauri et al., 2010), the simulation of future scenarios (e.g. Kusaka et al., 2012), and the evaluations of urbanization effect (e.g. Zhong et al., 2017) and

mitigation strategies of UHI (e.g. Jacobs et al., 2018).

However, accurate quantification of UHII using modelling grid data is still a challenge at present, although robust data are available from numerical modelling. In most of the previous studies, the UHII was calculated using the modelling data at selected urban grids and rural grids (e.g. Atkinson, 2003; Hamdi and Schayes, 2008; Salamanca et al., 2012). However, there is no unified criterion for the selections of urban and rural grids (Stewart and Oke, 2012). The grids are selected based on land cover categories (e.g. Zhao et al., 2014; Cao et al., 2016) or impervious surface areas (ISA) (e.g. Imhoff et al., 2010; Zhang et al., 2012). As a result, the derived UHII may vary largely and is not comparable due to the different selection of the grids. Schwarz et al. (2011) calculated UHII in European cities using eleven approaches for the selection of the grids and found that the derived UHII using different grids showed great differences. Different criterions for urban and rural grids make the inter-comparison of UHII among different studies challenging (Stewart, 2011). Additionally, the UHI intensity was defined as the maximum temperature difference between urban and rural areas in a city (e.g. Oke et al., 1973). This difference cannot be properly represented by a local temperature difference between the limited selected grids.

Land use change from natural surface to impervious surface is the major contribution to UHI (Oke, 1982). ISA represents the ratio of the impervious surface area in a grid, with a high value in highly-urbanized areas and a low value in rural areas. There is a close relationship between near-surface temperature and ISA in the spatial distribution (e.g. Kottmeier et al., 2007; Zhang et al., 2010). Schatz and Kucharik (2014) concluded that ISA was the primary driver of the spatial variations of air temperature and accounted for 80% of the spatial variations in the daytime and 74% of the spatial variations in the nighttime in Madison, USA, based on observations. Ryu and Baik (2012) also reported the important contribution of imperviousness on the UHI by using a mesoscale atmospheric model. Usually, the near-surface temperature increases with the increase in ISA, presenting a linear trend. Schatz and Kucharik (2014, 2015) and Li et al. (2018a) fitted the linear functions of in-situ observed air temperature and remote sensing land surface temperature, respectively, using ISA. The slope of fitted functions represented the increase in the temperatures when the surface

changed from natural to impervious and was used to calculate UHII. Although the ISA-based function of the near-surface temperature provides a promising method to quantify UHII using grid data, the application and evaluation of this new method in quantifying UHII using modelling grid data are still lacking and needed.

This study attempts to quantify UHII by applying the new method and the modelling data of Weather Research and Forecasting Model coupled with Urban Canopy Module (WRF/UCM), which is a widely used numerical model for the study of urban climate (Chen et al., 2011). The high-resolution UHI was simulated during a clear sky and calm wind period in the city of Berlin. The relationship between the simulated air temperature and the ISA in the WRF grids (ISA_{WRF}) was analyzed for different time periods of the day. The linear functions of the simulated air temperature were fitted against ISA_{WRF}. The temporal variation of the derived UHII was investigated and compared to those using traditional methods. The physical mechanism that controlled the derived UHII in the WRF/UCM was discussed based on the numerical functions of the model. The goal of this study is to (1) evaluate the feasibility of the ISA_{WRF}-based functions of the simulated air temperature in quantifying UHII, (2) investigate the spatial and temporal variations of the simulated UHI in the city of Berlin, and (3) examine the physical mechanism that controls the derived UHII.

2 Study Area and Methodology

2.1 Study area

The study area is Berlin (52.34°－52.68° N, 13.10°－13.77° E), the capital city of Germany (Figure 1a). Berlin is located in a temperate maritime climate zone. The mean annual temperature was 9.5 °C and the mean annual precipitation was 591 mm (based on the observation record at the DWD Dahlem station from 1981 to 2010). According to the report 2015 of the Statistical Office of Berlin-Brandenburg, about 3.5 million inhabitants live in this city. Berlin covers an area of around 900 km^2, with a flat topography (34－122 m, altitude). About 35% of the area is covered by the built–up surface and about 20% of the area is covered by the paving surface of transport and infrastructure (Figure 1b). The non-urban area is mainly covered by vegetation ecosystems, including forests and farmlands. Berlin's large

built-up and paving areas create a microclimate with pronounced UHI effects (Li et al., 2018b).

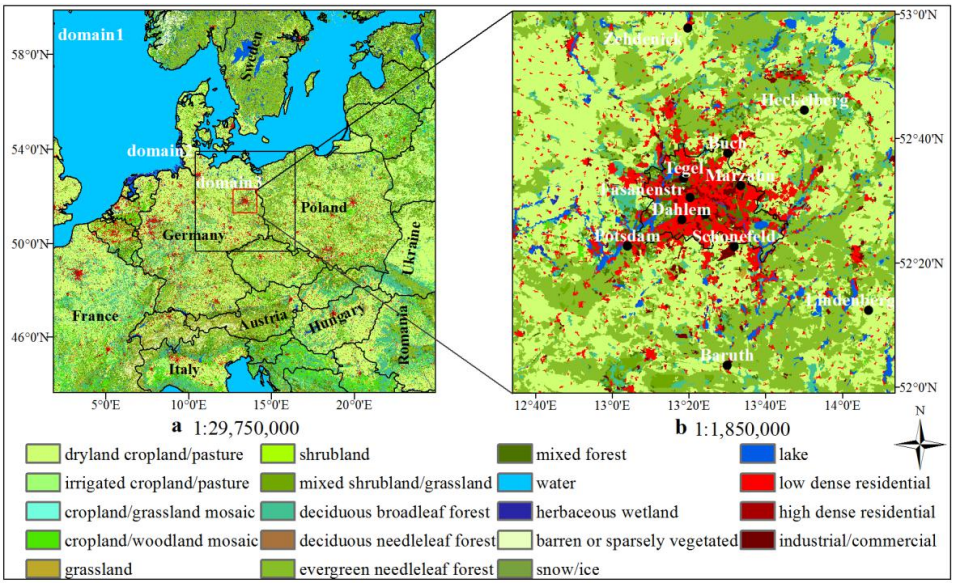

Figure 1. Setup of (a) the nested domains and (b) the innermost domain. The background shows CORINE land cover. The black points in subplot (b) show the locations of the in-situ observation stations.

2.2 Model description and configuration

2.2.1 WRF/UCM model

WRF/UCM version 3.7.1 was employed in this study. WRF is one of the most advanced numerical weather prediction system developed by the National Center for Atmospheric Research, USA. In order to address urban environmental issues, an integrated urban modelling system was developed to couple with the Noah-LSM scheme of WRF (Chen et al., 2011). The UCM used in this study is a single-layer model, which considers the shadowing, reflections, and trapping of radiation, the street orientation and diurnal variation of azimuth angle, surface energy budget of roofs, walls and roads, the wind profile in the canopy layer, and anthropogenic heat emissions (Kusaka et al., 2005). More detailed description of the UCM refers to Kusaka et al. (2001) and Kusaka and Kimura (2004). WRF/UCM is a promising utility for the urban climate related studies and has been widely used in the metropolitan regions of North America (e.g. Los Angeles) (Vahmani and Hogue, 2015), Asia (e.g. Beijing, Tokyo) (Miao et al., 2009; Kusaka et al., 2012) and Europe (e.g. London,

Athena, Helsinki, Firenze, Gliwice) (San José et al., 2013; Giannaros et al., 2018).

2.2.2 Domain setup and physical parameterization configuration

Three nested domains with the horizontal grid spacing of 15 km, 3 km, and 1 km were designed, with 119 x 119, 155 x 155 and 111 x 111 grid cells, respectively (Figure 1a). In the vertical direction, 35 levels were used. The physical parameterization schemes were chosen as follows: (1) the Lin scheme (Lin et al., 1983) for microphysics; (2) the Dudhia (Dudhia, 1989) and RRTM scheme (Mlawer et al., 1997) for shortwave and longwave radiation, respectively; (3) the Eta similarity scheme (Janjic, 1994) for surface layer; (4) the Bougeault–Lacarrére planetary boundary layer scheme (Jänicke et al., 2017); and (5) the Noah LSM scheme (Tewari et al., 2004) for land surface process over natural land cover and the UCM for urban surface process.

2.2.3 Update of urban parameters in the UCM

The critical parameters of UCM (Loridan et al., 2010), including morphological parameters, imperviousness of urban land cover, anthropogenic heat emissions, optical parameters, and thermal parameters, were updated for Berlin by using multi-source datasets. In the UCM, the city is represented as a combination of roofs, walls, and roads and is characterized by the size of the buildings and roads. These morphological parameters were calculated by using the virtual 3D city model datasets from the Department for Urban Development of Berlin Senate (Krüger and Kolbe, 2012). The mean building height ($Height_{building}$, m) and building width ($Width_{building}$, m) were calculated as the sum of the product of the height of each building and its area weight and the sum of the product of the width of each building and its area weight, respectively. The mean road width ($Width_{road}$, m) was calculated as the sum of the product of the width of each road and its area weight. In the UCM, the urban land cover includes impervious and vegetation components. The impervious component is characterized by the parameter of the fraction of the urban landscape which does not have vegetation (FRC_URB). The FRC_URB was calculated by using the product of imperviousness ($ISA_{Copernicus}$) version 2012 at a 100 m resolution from Copernicus Land Monitoring Service Pan-European Component (Sannier et al., 2016). The value of FRC_URB was calculated as the mean

$ISA_{Copernicus}$ at urban land cover areas. Anthropogenic heat emissions (AHE) were calculated by using a global anthropogenic heat flux database with a high spatial resolution of 30 s and a temporal resolution of 1 h from Dong et al. (2017). The value of AHE was calculated as the mean anthropogenic heat flux at urban land cover areas. The optical parameters (albedo and emissivity) and thermal parameters (thermal conductivity and capacity) of roofs, walls, and roads were determined by referring to the studies of Schubert and Grossman-Clarke (2013) and Wolter (2016), respectively. The updated urban parameters are listed in Table 1.

Table 1. Updated urban parameters in the UCM.

Urban Parameters	Objects	Unit	Low dense residential	High dense residential	Industrial/ commercial
$Height_{building}$	Building	m	10.27	17.86	10.88
$Width_{building}$	Buidling	m	16.61	22.83	48.29
$Width_{road}$	Road	m	13.52	16.85	16.28
Albedo & Emissivity	Roof	-		0.163 & 0.90	
	Wall	-		0.162 & 0.90	
	Road	-		0.162 & 0.95	
Thermal conductivity & Heat capacity	Roof	$J\ m^{-1}\ s^{-1}\ K^{-1}$ & $J\ m^{-3}\ K^{-1}$		$0.695\ \&\ 0.8x10^{-6}$	
	Wall			$0.695\ \&\ 0.8x10^{-6}$	
	Road			$0.4004\ \&\ 1.0x10^{-6}$	
FRC_URB	-	-	0.47	0.88	0.78
AHE (July)	-	W/m^2	11.25	37.93	9.95

2.2.4 Datasets of land cover, initial and lateral boundary conditions

The United States Geological Survey (USGS) land cover classification system with three categories of urban land cover, including low dense residential, high dense residential, and industrial/commercial, was adopted in WRF/UCM. This study used CORINE land cover (CLC) data version 2012 at a 100 m resolution to drive the land surface process in the model.

The CLC data was reclassified to the USGS classification system referring to the study of Pineda et al. (2004) and Tewari et al. (2007). The spatial resolution of CLC data is much finer than that of the grids in the domain 3. In order to distinguish the sub-grid variation of the land cover within the domain grids, the mosaic approach of Noah LSM was implemented in this study (Li et al., 2013). The mosaic approach considers more categories of land cover within each grid cell based on the choice of the user. The energy balance in each sub-grid land cover tile is calculated, separately. The mosaic approach helps the model to simulate land surface process more detailed and to avoid the simulation errors from the interpolation of land cover data. In this study, the maximum categories of land cover (N=9) in the grids across domain 3 was set. Figure 2 shows the spatial patterns of the fraction of the three categories of urban land cover within each grid. The low dense residential occupies a large number of grids with high fractions in the urban areas and several grids with low fractions in the surrounding rural areas. The high dense residential only occupies few grids concentrated in the urban center. The industrial/commercial areas are mainly located in the urban center and airport. The numbers of the grids that are dominated by the urban land cover (fraction>50%) of low dense residential, high dense residential, and industrial/commercial are 542, 2, and 82, respectively.

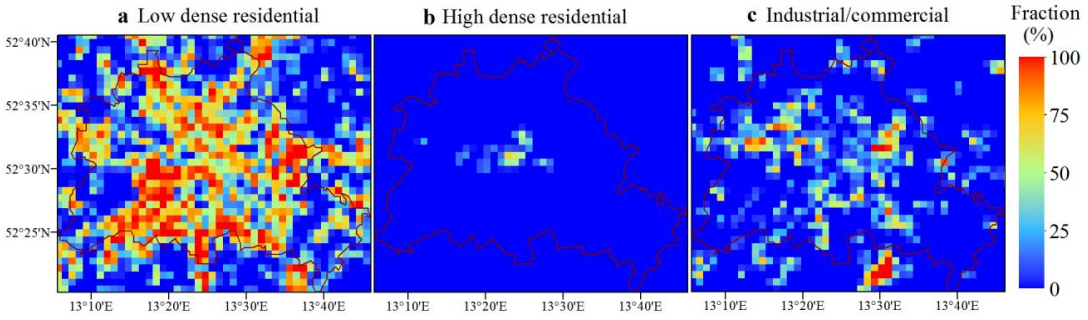

Figure 2. Spatial patterns of the fractions of (a) low dense residential, (b) high dense residential and (c) industrial/commercial.

Reanalysis data of Global Forecast System (GFS) developed by the National Centers for Environmental Prediction (NCEP) at a 0.5-degree spatial resolution and a 6 hour temporal resolution were applied as the initial and lateral boundary conditions for the model running. In addition, given the long-term running, the daily Real-Time Global Sea Surface Temperature data from NCEP at a 0.5-degree spatial resolution was applied to drive model running.

2.2.5 Simulation period

The period from 21st June to 3rd July 2010 was chosen to carry out the simulation. During this period, clear sky and calm wind situations were dominant. The cloud fraction was less than one quarter during the half of the period. The mean wind speed was 2.46 and 1.81 m/s for the daytime and nighttime, respectively. As recommended by the user's guide of WRF, 6 times of the grid resolution of domain 1 (in km) was set as the time-step (90 s). The hourly simulation data in domain 3 were used to analyze the UHI. The first 24 h were taken as spin-up time and were excluded during the post-processing and analysis of the simulation data.

2.2.6 Model evaluation

The simulated air temperature was evaluated by comparing against the in-situ observation data at twelve meteorological stations (Figure 1b). Six stations (Tempelhof, Fassanenstr, Buch, Tegel, Dahlem, and Marzahn) are located in the urban areas, and six stations (Heckelberg, Lindenberg, Zehdenick, Baruth, Potsdam, and Schoenefeld) are located in the surrounding rural areas. Statistical indicators, including root mean square error (RMSE), mean bias (MB), Pearson correlation coefficient (r) and Interobserver Agreement (IOA) were used to evaluate the model performance. The equations of these statistical indicators refer to the study of Li et al. (2017).

2.3 Calculation of UHII

The air temperature at 2 m height (T_{2m}) in the WRF/UCM is calculated based on the transfer function of sensible heat flux (Li and Bou-Zeid, 2014; Giannaros et al., 2018) as follows

$$T_{2m} = T_s - \frac{SH}{\rho C_{h2m} U_{2m}} \quad (1)$$

where T_s is the surface temperature; SH is the sensible heat flux; C_{h2m} is the transfer coefficient; U_{2m} is the wind speed at 2 m height. The urban land cover includes both impervious and vegetation components. In the UCM, the fractions of impervious and vegetation components are FRC_URB and (1-FRC_URB), respectively. The overall T_s and SH over urban land cover are calculated as the weighted sum of those two variables of

impervious and vegetation components as follows

$$T_s = FRC\_URB \times T_{s(impervious)} + (1 - FRC\_URB) \times T_{s(vegetation)} \quad (2)$$

$$SH = FRC\_URB \times SH_{(impervious)} + (1 - FRC\_URB) \times SH_{(vegetation)} \quad (3)$$

where $T_{s(impervious)}$ and $T_{s(vegetation)}$ are the surface temperature and $SH_{(impervious)}$ and $SH_{(vegetation)}$ are the sensible heat flux of impervious and vegetation components, respectively. Replacing the T_s and SH in Equation (1) with Equation (2) and (3), the equation of T_{2m} over urban land cover is changed to a new form as follows

$$T_{2m} = FRC\_URB \times \underbrace{\left(T_{s(impervious)} - T_{s(vegetation)} - \frac{SH_{(impervious)} - SH_{(vegetation)}}{\rho C_{h2m} U_{2m}}\right)}_{\text{UHII}} + \underbrace{T_{s(vegetation)} - \frac{SH_{(vegetation)}}{\rho C_{h2m} U_{2m}}}_{T_{2m(vegetation)}} \quad (4)$$

The calculation function of T_{2m} becomes a linear function that is fitted using FRC_URB as the variable. The intercept of the function is the air temperature over the vegetation surface, $T_{2m(vegetation)}$. The slope of the function represents the increase in the T_{2m} along with the increase in FRC_URB from 0 (vegetation surface) to 100% (impervious surface) and can be taken as UHII. The mosaic approach enables each grid to include both urban and non-urban land cover tiles (Li et al., 2013). Given that most of the non-urban surface is covered by vegetation in the study area, the land cover of each grid is composed of the impervious component from urban tiles and the vegetation components from urban tiles and non-urban tiles. Thus, the calculation function of T_{2m} becomes a function of the overall ISA_{WRF} at each grid, which is the weighted sum of the individual imperviousness and the corresponding fraction of the three categories of urban land cover tiles within the grid. The ISA_{WRF} is calculated as follows

$$ISA_{WRF} = \sum_{i=31}^{33} FRC\_URB(i) \times LANDUSEF(i) \times 100\% \quad (5)$$

where LANDUSEF(i) is the area fraction of low dense residential, high dense residential, and commercial/industrial, whose index (i) in the USGS land cover system are 31, 32, and 33, respectively. The data of LANDUSEF(i) was extracted from the output file of the WRF Preprocessing System program.

The analysis above provides a theoretical basis for the application of the ISA_{WRF}-based function of simulated T_{2m} to quantify UHII. Urban areas have highly inhomogeneous surface. The configuration of land cover categories within each grid vary greatly across the study areas. As a result, the simulated T_{2m} at the grids with the same ISA_{WRF} may show some differences, due to the different land cover configurations among the grids. In addition, the difference of the reanalysis data at the four latent boundaries may also generate some differences of the simulated T_{2m} among the grids at different locations in the domain. In order to achieve good ISA_{WRF}-based functions of T_{2m}, a zonal analysis method was used. All the grids in the study area were divided into 50 groups with a constant ISA_{WRF} interval of 2%. The first group contains the grids with the ISA_{WRF} ranging from 0 to 2%, and the second group contains the grids with the ISA_{WRF} ranging from 2% to 4%, and so forth until the last group contains the grids with the ISA_{WRF} ranging from 98% to 100%. The mean T_{2m} and ISA_{WRF} were calculated within each group. Then the ISA_{WRF}-based linear functions of the mean simulated T_{2m} were fitted using the mean values of all the groups. Referring to the previous studies (e.g. Oke 1973), the UHI intensity was defined as the maximum urban-rural difference of temperature in this study. Given that the largest ISA_{WRF} in the study area is smaller than 100% (based on the results in section 3.2 below), the real UHII is calculated as the products of the slope of the fitted functions and the largest ISA_{WRF}. The coefficient of determination (R^2) was used to evaluate the feasibility of the fitted functions. Water bodies are usually cooler in the daytime and warmer at nighttime than the other land cover, weakening the T_{2m}-ISA_{WRF} relationship. During the calculation of UHII, the grids with water tiles were excluded. The analysis was conducted over three time periods of the day, including daytime, nighttime, and the transition between daytime and nighttime. The daytime (7:00-17:00 UTC) refers to the hours with solar radiation and downward ground heat flux. The nighttime (21:00-03:00 UTC) refers to the hours without solar radiation. The transition period (4:00-6:00&18:00-20:00 UTC) refers to the hours with solar radiation, but upward ground heat flux.

3 Results

3.1 Model performance in simulating T_{2m}

In general, the simulated T_{2m} matches the observations in the diurnal cycle well (Figure 3),

with a correlation coefficient of 0.95 ($p<0.01$). The RMSE and IOA are 1.76 °C and 0.64, respectively (Table 2). The simulation shows an underestimation during the daytime, while an overestimation at nighttime. The mean bias is small, with a value of 0.02 °C. The simulation at the urban stations shows slightly larger errors, compared to the simulation at the rural stations. The model performance is broadly consistent with the previous study in this region for long-term running (Jänicke et al., 2017) and the case studies in other regions (Bhati and Mohan, 2016). Additionally, the large biases mainly happen when the temperatures change significantly. The model running was driven by the lateral boundary condition (reanalysis data). The systematic errors of the reanalysis data in capturing the change of weather processes may be the reason for the large simulation biases during the period with a large change of temperatures (Huang and Gao, 2018). The performance of the model at each station refers to Figure S1 in the supplementary file.

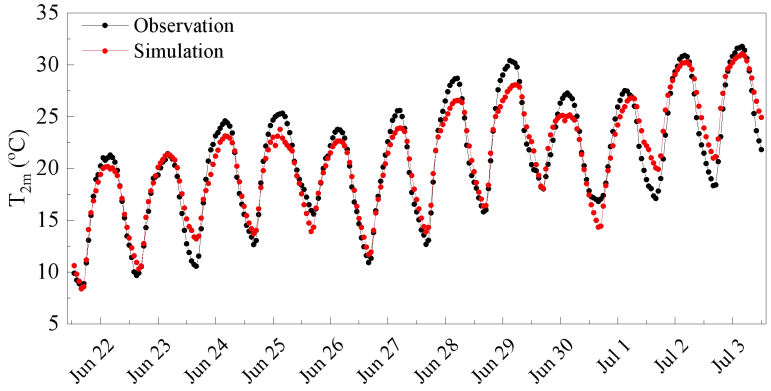

Figure 3. Comparison of the simulated and observed mean T_{2m} over all in-situ stations.

Table 2. RMSE, MB, r, and IOA of the simulated T_{2m} against the in-situ observations.

Stations	RMSE (°C)	MB (°C)	r	IOA
Overall	1.76	0.02	0.95	0.64
Urban stations	1.83	-0.11	0.94	0.60
Rural stations	1.70	0.15	0.96	0.67

3.2 Spatial patterns of ISA_{WRF} and $ISA_{Copernicus}$

Both derived ISA_{WRF} and observed $ISA_{Copernicus}$ are high in the urban areas and low in the

surrounding rural areas (Figure 4). The spatial patterns of the ISA_{WRF} and $ISA_{Copernicus}$ are similar, with a correlation coefficient of 0.74 ($p<0.01$). But the ISA_{WRF} shows less spatial variation than the $ISA_{Copernicus}$. Compared to the observed $ISA_{Copernicus}$, the ISA_{WRF} is lower in the urban center and higher in the rural areas. The FRC_URB in Equation 5 was calculated as the mean $ISA_{Copernicus}$ of the three categories of urban land cover in the whole study area. Thus, the derived ISA_{WRF} underestimates the $ISA_{Copernicus}$ in the high impervious areas, while it overestimates the $ISA_{Copernicus}$ in the low impervious areas. This may be one reason for the underestimation of the T_{2m} at the urban stations and the overestimation at the rural stations, as shown in Table 2. The largest ISA_{WRF} (84.97%) is < 100%. The spatial pattern of the ISA_{WRF} is controlled by the FRC_URB of the three categories of urban land cover. The low ISA_{WRF} is mainly consistent with the low dense residential land cover (Figure 2a), while the high ISA_{WRF} is mainly corresponding to high dense residential and industrial/commercial land cover (Figure 2b and c).

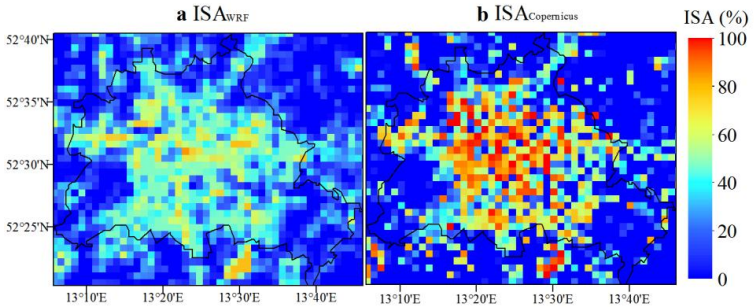

Figure 4. Spatial patterns of (a) ISA_{WRF} and (b) $ISA_{Copernicus}$.

3.3 Spatial patterns of simulated T_{2m}

The study area shows a UHI in the nighttime and transition period, with high simulated T_{2m} in the urban areas and low simulated T_{2m} in the surrounding rural areas (Figure 5). Especially at night, the UHI is pronounced. The spatial pattern of the UHI shows some similarity with that of the ISA_{WRF} as shown in Figure 4a. In the daytime, the simulated T_{2m} does not show a significant urban-rural difference. The simulated T_{2m} in some of the urban areas is even slightly lower than that in the rural areas. The results are consistent with the study of Jänicke et al. (2017) in this region.

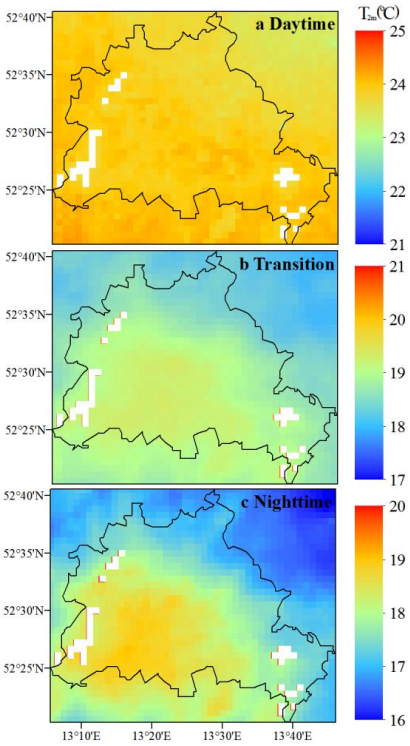

Figure 5. Spatial patterns of the simulated mean T_{2m} in the (a) daytime, (b) transition period, and (c) nighttime. Grids in white are areas covered by lakes.

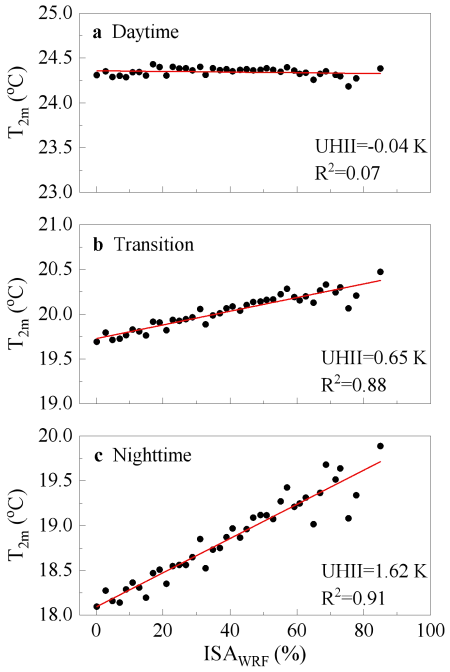

Figure 6. The relationship between the simulated mean T_{2m} and the ISA_{WRF} in the (a) daytime, (b) transition period, and (c) nighttime during the simulation period. The dots show the mean values of the simulated T_{2m} and ISA_{WRF} within all the 2% intervals of the ISA_{WRF} in the study area.

3.4 Quantifying UHII using ISA_{WRF}-based functions of T_{2m}

In the nighttime and the transition period, the mean T_{2m} increases with the increase in the ISA_{WRF} (Figure 6), presenting positive linear relationships between them. Two linear functions of the mean T_{2m} are well fitted using the ISA_{WRF}, with the R^2 of 0.91 (P<0.01) for the nighttime and 0.88 (P<0.01) for the transition period. The derived UHII is 1.62 K at nighttime and 0.65 K in the transition period, respectively. In the daytime, the T_{2m}-ISA_{WRF} relationship is not significant. The simulated daytime mean T_{2m} generally shows a minor variation with the increase in the ISA_{WRF}. The derived daytime UHII is -0.04 K.

The ISA_{WRF}-based functions of the simulated T_{2m} were also fitted at each hour during the simulation period. At night, most of the functions are well fitted, with > 75% of the R^2 larger than 0.8 (Figure 7). In the transition period, most of the fitted functions achieve large R^2 with half of the values larger than 0.6. In the daytime, the correlation between the simulated T_{2m} and ISA_{WRF} is not high, because of the minor urban-rural difference of the simulated temperature. The derived UHII is high in the nighttime and low in the daytime, presenting 'U-shaped' curves (Figure 8). The daily highest UHII usually appears within the three hours after sunset. During the daytime, the UHII are slightly negative sometimes from 7:00 to 17:00 UTC. The precipitation can affect the T_{2m}-ISA_{WRF} relationship, subsequently changing the derived UHII. On June 25, the slight precipitation leads to extreme low UHII.

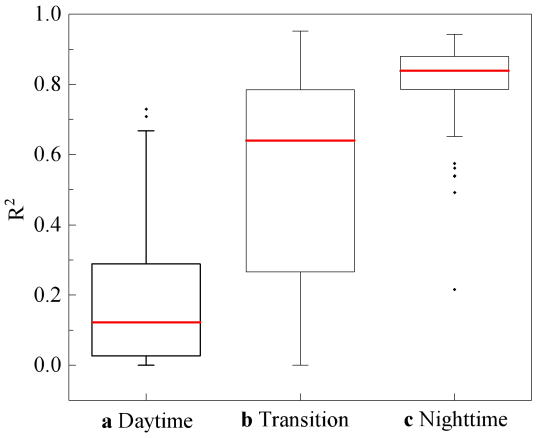

Figure 7. Box plots of the R^2 for the ISA_{WRF}-based functions of T_{2m} in the (a) daytime, (b) transition period, and (c) nighttime.

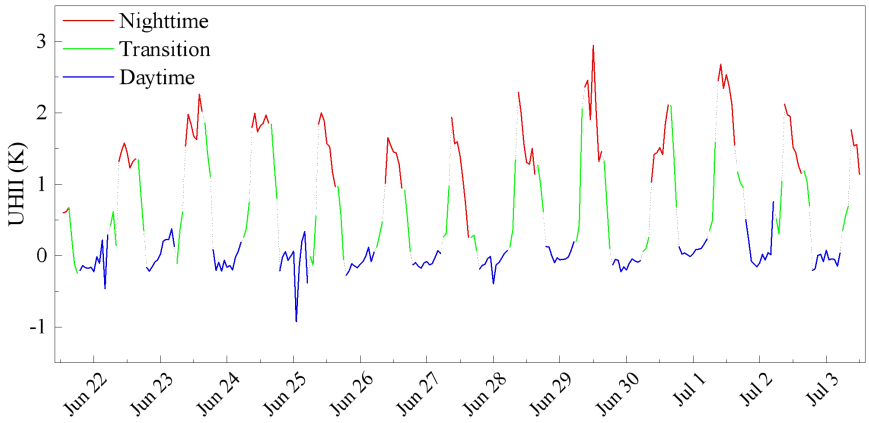

Figure 8. Diurnal variations of the derived UHII during the simulation period.

4 Discussion

4.1 Comparison with traditional calculation methods of UHII

In order to further evaluate the new method of the ISA_{WRF}-based function of T_{2m} in quantifying UHII, a comparison between the derived UHII by using the new method and those by using traditional methods was carried out. Traditionally, the difference of the air temperature between selected urban grids and rural grids was defined as UHII. However, the criterions for the selection of urban and rural grids vary. Here we chose three frequently used traditional methods to conduct the comparison study. Referring to the studies of Hamdi and Schayes (2008), Schwarz et al. (2011) and Zhou et al. (2017), the UHII was calculated using the mean temperatures of the grids in the dense urban areas and in the rural areas outside the city. We refer to it as traditional method 1. Referring to the studies of Atkinson (2003), Zhao et al. (2014), and Cao et al. (2016), the UHII was calculated using the mean temperatures of the selected urban grids in the city center and of the selected rural grids in the four directions of the surrounding areas. We refer to it as traditional method 2. Referring to the studies of Imhoff et al. (2010) and Zhang et al. (2012), the UHII was calculated using the mean temperature of the grids in urban and rural areas as defined by ISA. We refer to it as traditional method 3. In this study, the urban center areas within the ring subway (red zone) and the rural areas outside the border (green zone) in Figure 9 were selected for the calculation of method 1. The nine grids (3x3) in the urban center (square with yellow crossing) and thirty-six (3x3x4) grids in the rural areas (squares with yellow slashes) in the four

directions of the urban center (Figure 9) were selected for the calculation of method 2. The grids with ISA_{WRF} larger than 0.7 and the grids with ISA_{WRF} equal to 0 were selected for the calculation of method 3.

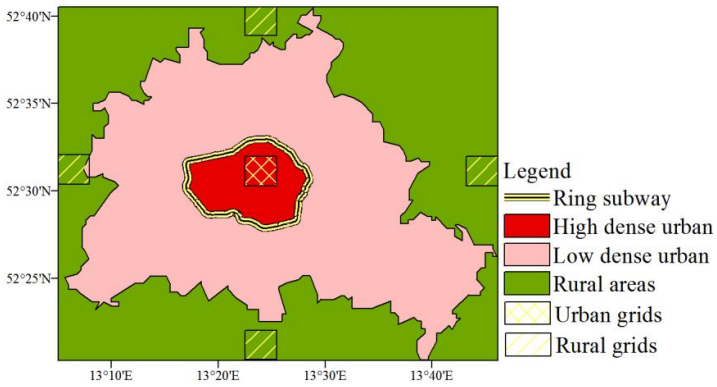

Figure 9. The location of the selected grids for the calculation of UHII using traditional methods.

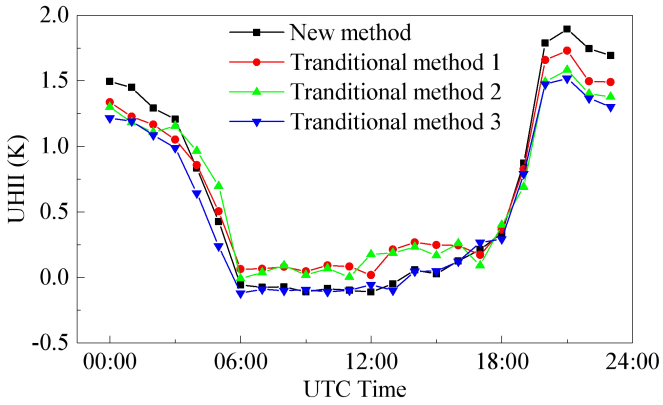

Figure 10. Diurnal variations of the UHII that is calculated using the new method and three traditional methods.

The derived UHII using four methods shows similar diurnal variations, with large values at nighttime and small values during the daytime (Figure 10). The derived UHII using the new method shows a good agreement with the derived UHII using the traditional methods. The correlation coefficients between the derived UHII of the new method and the results of the three traditional methods are 0.97, 0.93, and 0.97 ($p<0.01$), respectively. However, the derived UHII using the new method is unique for each city, while the derived UHII using the traditional methods varies with the different selections of urban and rural grids. The new method overcomes the uncertainties from the different selections of urban and rural grids.

Moreover, the new method considers the simulated T_{2m} of all the grids in the study area and reflects the overall characteristic of the simulated urban thermal environment, while the traditional methods only consider the T_{2m} of the selected grids (Stewart and Oke, 2012). The derived UHII using the new method shows larger absolute values of UHI than those using the traditional methods (Figure 10). The ISA_{WRF}-based function of the simulated T_{2m} is a promising approach for the quantification of UHII using WRF/UCM modelling data.

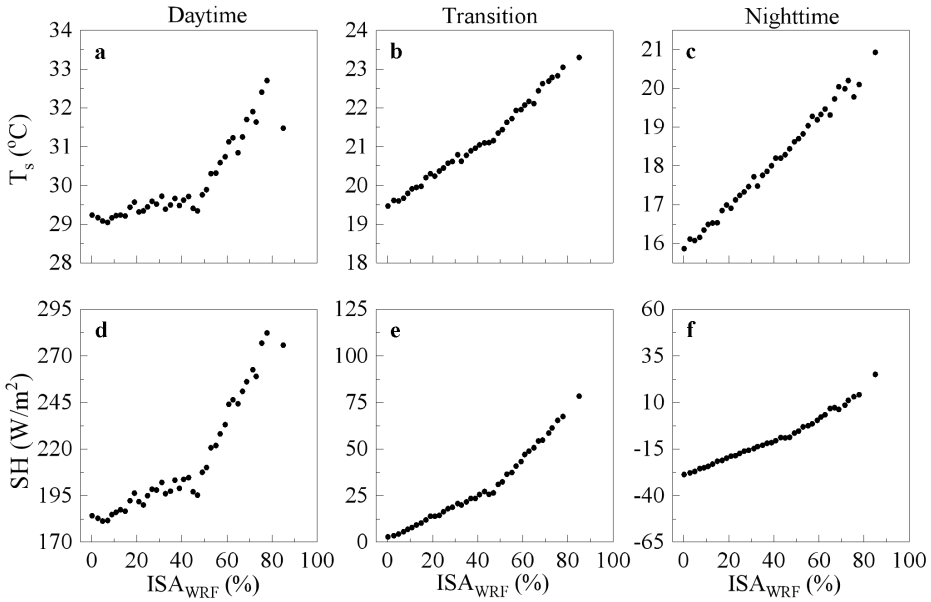

Figure 11. Variations of the simulated mean (a-c) T_s and (d-f) SH versus mean ISA_{WRF} in the different time periods of the day during the simulation period. Three columns represent the variations in the (left) daytime, (middle) transition period, and (right) nighttime. The dots in each subplot show the simulated mean T_s and SH within all the 2% intervals of the ISA_{WRF} in the study area.

4.2 Physical mechanism that controls the derived UHII

The simulated T_{2m} at each grid is mainly determined by the difference of the T_s and SH between impervious surface and vegetation surface and the ISA_{WRF}, referring to Equation 4. Usually, the impervious surface shows higher T_s and SH than the vegetation surface, due to lower Bowen ratio and larger energy storage (Oke, 1982; Rizwan et al., 2008). The increasing trends of T_s and SH with the increase in ISA_{WRF} reflect the difference of T_s and SH between impervious surface and vegetation surface. In order to investigate the physical mechanism that

controls the T_{2m}-ISA_{WRF} relationship and the derived UHII in WRF/UCM, the relationships between the simulated T_s and SH and the ISA_{WRF} were examined. In the nighttime and transition period, both the T_s and SH increase linearly with the increase in the ISA_{WRF} (Figure 11b, c, e, and f). The difference of the T_s and SH between impervious surface and vegetation surface is similar at all grids, leading to the good nighttime and transition -period T_{2m}-ISA_{WRF} relationship. However, in the daytime, the increasing trend of the daytime T_s and SH become larger when the ISA_{WRF} exceeds around 50% (Figure 11a and d). This two-phase increase reflects the various differences of the T_s and SH between impervious surface and vegetation surface among the grids, which lead to the weak daytime T_{2m}-ISA_{WRF} relationship.

The shading of the buildings could possibly be the main reason for the daytime two-phase increasing trend of the T_s and SH along with the increase in the ISA_{WRF} in the daytime. In the UCM, the T_s and SH of the impervious surface are jointly determined by the energy balance on the roofs, walls, and roads (Tewari et al., 2007; Chen et al., 2011). The daytime incoming radiation on the roads and walls is affected by the shading of the buildings. The low dense residential and high dense residential land cover have the smallest ratio of roof width to road width and the largest ratio of building height to road width (Table 3), respectively, while the industrial/commercial land cover has the largest ratio of roof width to road width and the smallest ratio of building height to road width. The industrial/commercial land cover is less affected by the shading of the buildings, resulting in the larger T_s and SH, compared to the low dense residential and high dense residential land cover. The major urban land cover of the grids with $ISA_{WRF} > 50\%$ is the industrial/commercial land cover, while the major urban land cover of the grids with $ISA_{WRF} < 50\%$ is the low dense residential land cover (Figure 2 and 4). Therefore, the increasing trend is more significant when the ISA_{WRF} is larger than 50%. The shading-induced two-phase increase in the T_s and SH with the increase in the ISA_{WRF} indicates that the differences of the T_s and SH between impervious surface and vegetation surface among the grids with different urban land cover are inconsistent. As a result, the overall daytime T_{2m}-ISA_{WRF} relationship is weak. In the transition period, the surface energy balance is also affected by the shading of the buildings. However, this influence is limited because of the weak solar radiation and the release of stored heat in the

impervious surface during this period. Thus, the increasing trends of T_s and SH do not change significantly with the increase in the ISA_{WRF} (Figure 11b and e).

Table 3. The ratio of building height to road width, and the ratio of roof width to road width in the three categories of urban land cover.

Variables \ Urban land cover	Low dense residential	High dense residential	Industrial/ commercial
Ratio of building height to road width	0.76	1.06	0.67
Ratio of roof width to road width	0.55	0.58	0.75

The overall difference of the T_s and SH between the impervious surface and the vegetation surface determines the derived UHII, based on Equation 4. The increasing ranges of the T_s and SH are 3.65, 3.82, and 5.06 K and 100.98, 75.75, and 53.78 W/m^2 for the daytime, transition period, and nighttime, respectively (Figure 11). There is a large overall difference of the T_s and a small overall difference of SH between impervious surface and vegetation surface at night, while a small overall difference of the T_s and a large overall difference of the SH between impervious surface and vegetation surface during the day. The former led to the high nighttime UHII, while the latter led to the low and even negative daytime UHII.

This study mainly focuses on the influence of urban geographic information on the urban surface process and UHI and examined its physical mechanisms. The development of convection can affect the heat flux, subsequently changing near-surface UHI. In order to further examine the comprehensive influencing mechanism of UHI, the influence of the development of convection on the simulated UHI needs to be investigated in the further study.

4.3 The influence of specifying urban parameters on the simulation of UHI

Specifying key urban parameters is a big challenge for the simulation of UHI using WRF/UCM (Chen et al., 2011). The current model applies a table lookup method to specify the urban parameters of each grid. In this method, the constant urban parameters are associated with urban land use types. Each parameter only has three values, corresponding to

the three types of urban land in the UCM. However, the urban surface has high heterogeneity. The constant urban parameters of limited types of urban land use cannot fully reflect the detailed actual information of urban canopy (Lin et al., 2016). As is shown in Figure 4, although the overall spatial pattern of the imperviousness is achieved, the derived ISA_{WRF} is lower than the observation in the urban center, while is higher than the observation in the surrounding rural areas, which leads to the under- and overestimation of the temperature in urban and rural areas, respectively. As a result, the derived UHII may be lower than the actual value. Similar problems also exist for other key parameters, such as anthropogenic heat emissions, which also plays an important role for the UHI (Ryu and Baik, 2012). Accurate simulation of UHI needs to input more detailed urban canopy information. The gridded urban parameter datasets may be a good solution. For example, the National Urban Database and Access Portal Tool provides accurate gridded datasets of urban parameters for the cities in the United States, which can contribute to the improvement of WRF/UCM performance (Ching et al. 2009). In northern Taiwan, Lin et al. (2016) modified the UCM by incorporating 2-D spatial distribution maps of urban fraction and anthropogenic heat and generated a better simulation result. Future study could consider establishing the gridded urban parameter datasets for more cities if robust urban datasets are available.

5 Conclusions

This study simulated UHI in the city of Berlin using WRF/UCM and quantified the UHII using the method of ISA_{WRF}-based functions of the simulated T_{2m}. The model performed well in simulating T_{2m} during the study period. The correlation coefficient and RMSE between the simulation and the observation were 0.95 ($p<0.01$) and 1.76 °C, respectively. The simulation results showed a pronounced UHI at nighttime in the study area. The simulated nighttime T_{2m} linearly increased with the increase in the ISA_{WRF}. The ISA_{WRF}-based linear functions of T_{2m} were well fitted. The derived UHII showed ‘U-shaped’ diurnal variations, with large values at nighttime. The daytime UHII was low and even negative. The differences of the simulated T_s and SH between impervious surface and vegetation surface jointly controlled the derived UHII. In the nighttime, the large difference of T_s and small difference of SH between impervious surface and vegetation surface generated high nighttime UHII and vice versa in

the daytime. The new method overcomes the uncertainties of traditional methods in selecting urban/rural grids and considers the overall characteristic of the simulated UHI at all the grids in the study area.

However, there are still some uncertainties and improvement space for the current simulation and quantification method. As for the simulation of temperature, the current WRF/UCM used a table-based method to input the urban parameters of the three types of urban land cover. The problems of under- and overestimation of the simulation exist because of the difference of the constant urban parameters and actual various values. Future simulation should consider applying the gridded urban parameters to drive model running if the robust datasets are available. As for the quantification of the UHII, this study used horizontal imperviousness to fit the function of temperature, referring to the calculation equations of temperature in the model. The vertical imperviousness associated with the wall may also have some influence on the simulated temperature. Future study should take this influence into consideration, despite the influence is thought to be complicated. Meanwhile, it should be noted that some functions in the daytime were not well fitted, because of the rather small urban-rural difference of the simulated daytime temperature. The derived UHII based on these fitted functions may have some uncertainties. It is better to check the magnitude and diurnal variation of the derived UHII carefully to avoid the possible incorrect values. Additionally, it should be noted that the good performance of the new method in estimating UHII was achieved under typical UHI conditions with the calm and cloudless weather. Under other weather conditions, the dependence of temperature on ISA may become weak. The feasibility of the application of the new method under other weather conditions needs further evaluation in the future study.

6 Acknowledgments

This research is supported by the China Scholarship Council. The authors thank the Beijing Office of Freie Universität Berlin. Special thanks go to Patricia Margerison for proofreading this manuscript.

7 References

American Association for the Advancement of Science (AAAS), 2016. Rise of the City. Science 352, 906-907.

Atkinson, B.W., 2003. Numerical modelling of urban heat-island intensity. Bound-Lay. Meteorol. 109, 285-310.

Bhati, S., Mohan, M., 2016. WRF model evaluation for the urban heat island assessment under varying land use/land cover and reference site conditions. Theor. Appl. Climatol. 126, 385-400.

Cao, C., Lee, X., Liu, S., Schultz, N., Xiao, W., Zhang, M., Zhao, L., 2016. Urban heat islands in China enhanced by haze pollution. Nat. commun. 7, doi:10.1038/ncomms12509.

Chen, F., Kusaka, H., Bornstein, R., Ching, J., Grimmond, C.S.B., Grossman-Clarke, S., Loridan, T., Manning, K.W., Martilli, A., Miao, S., Sailor, D., Salamanca, F.P., Taha, H., Tewari, M., Wang, X., Wyszogrodzki, A.A., Zhang, C., 2011. The integrated WRF/urban modelling system: development, evaluation, and applications to urban environmental problems. Int. J. Climatol. 31, 273-288.

Ching, J., Brown, M., McPherson, T., Burian, S., Chen, F., Cionco, R., Hanna, A., Hultgren, T., Sailor, D., Taha, H., Williams, D. 2009. National urban database and access portal tool. B. Am. Meteorol. Soc. 90(8), 1157-1168.

Dong, Y., Varquez, A.C.G., Kanda, M., 2017. Global anthropogenic heat flux database with high spatial resolution. Atmos. Environ. 150, 276-294.

Dudhia, J., 1989. Numerical study of convection observed during the Winter Monsoon Experiment using a mesoscale two–dimensional model. J. Atmos. Sci. 46, 3077-3107.

Giannaros, C., Nenes, A., Giannaros, T.M., Kourtidis, K., Melas, D. 2018. A comprehensive approach for the simulation of the Urban Heat Island effect with the WRF/SLUCM modeling system: The case of Athens (Greece). Atmos. Res. 201, 86-101.

Hamdi, R., Schayes, G. 2008. Sensitivity study of the urban heat island intensity to urban

characteristics. Int. J. Climatol. 28(7), 973-982.

Huang, D., Gao, S. 2018. Impact of different reanalysis data on WRF dynamical downscaling over China. Atmos. Res. 200, 25-35.

Imhoff, M.L., Zhang, P., Wolfe, R.E., Bounoua, L., 2010. Remote sensing of the urban heat island effect across biomes in the continental USA. Remote Sens. Environ. 114 (3), 504-513.

Jacobs, S.J., Gallant, A.J., Tapper, N.J., Li, D. 2018. Use of cool roofs and vegetation to mitigate urban heat and improve human thermal stress in Melbourne, Australia. J. Appl. Meteorol. Clim. https://doi.org/10.1175/JAMC-D-17-0243.1

Janjic, Z.I., 1994. The step-mountain Eta coordinate model: further developments of the convection, viscous sublayer and turbulence closure schemes. Mon. Wea. Rev. 122, 927-945.

Jänicke, B., Meier, F., Fenner, D., Fehrenbach, U., Holtmann, A., Scherer, D., 2017. Urban–rural differences in near‐surface air temperature as resolved by the Central Europe Refined analysis (CER): sensitivity to planetary boundary layer schemes and urban canopy models. Int. J. Climatol. 37(4), 2063-2079.

Kottmeier, C., Biegert, C., Corsmeier, U., 2007. Effects of urban land use on surface temperature in Berlin: Case study. J. Urban Plan. D. 133(2), 128-137.

Krüger, A., Kolbe, T.H., 2012. Building analysis for urban energy planning using key indicators on virtual 3D city models—the energy atlas of Berlin. International Archives of the Photogrammetry, Remote Sensing and Spatial Information Sciences 39(B2), 145-150.

Kusaka, H., Kimura, F., 2004. Coupling a single-layer urban canopy model with a simple atmospheric model: Impact on urban heat island simulation for an idealized case. J. Appl. Meteor. 82, 1899-1910.

Kusaka, H., Kondo, H., Kikegawa, Y., Kimura, F., 2001. A simple single-layer urban canopy model for atmospheric models: Comparison with multi-layer and slab models. Bound-Lay. Meteorol. 101(3), 329-358.

Kusaka, H., Chen, F., Tewari, M., Hirakuchi, H., 2005. Impact of using the urban canopy model on the simulation of the heat island. WRF/MM5 User's Workshop. Boulder, Colorado. Session 4.2, http://www2.mmm.ucar.edu/wrf/users/workshops/WS2005/abstracts/Session4/2-Kusaka.pdf

Kusaka, H., Hara, M., Takane, Y., 2012. Urban climate projection by the WRF model at 3-km horizontal grid increment: dynamical downscaling and predicting heat stress in the 2070's August for Tokyo, Osaka, and Nagoya metropolises. J. Meteorol. Soc. Jpn. 90, 47-63.

Li, D., Bou-Zeid, E., Barlage, M., Chen, F., Smith, J.A., 2013. Development and evaluation of a mosaic approach in the WRF-Noah framework. J. Geophys. Res. Atmos. 118, 918-935.

Li, D., Bou-Zeid, E., 2014. Quality and sensitivity of high-resolution numerical simulation of urban heat islands. Environ. Res. Lett. 9(5), 055001.

Li, H., Wolter, M., Wang, X., Sodoudi, S., 2017. Impact of land cover data on the simulation of urban heat island for Berlin using WRF coupled with bulk approach of Noah-LSM. Theor. Appl. Climatol. https://doi.org/10.1007/s00704-017-2253-z.

Li, X., Zhou, Y., Asrar, G.R., Imhoff, M., Li, X., 2017. The surface urban heat island response to urban expansion: A panel analysis for the conterminous United States. Sci.Total Environ. 605, 426-435.

Li, H., Zhou, Y., Li, X., Meng, L., Wang, X., Wu, S., Sodoudi, S., 2018a. A new method to quantify surface urban heat island intensity. Sci.Total Environ. 624, 262-272.

Li, H., Meier, F., Lee, X., Chakraborty, T., Liu, J., Schaap, M., Sodoudi, S., 2018b. Interaction between urban heat island and urban pollution island during summer in Berlin. Sci.Total Environ. 636, 818-828.

Lin, Y., Richard, D.F., Harold, D.O., 1983. Bulk Parameterization of the Snow Field in a Cloud Model. J. Climate Appl. Met. 22, 1065-1092.

Lin, C.Y., Su, C.J., Kusaka, H., Akimoto, Y., Sheng, Y.F., Huang, J.C., Hsu, H.H., 2016. Impact of an improved WRF urban canopy model on diurnal air temperature simulation over northern Taiwan. Atmos. Chem. Phys. 16, 1809-1822.

Loridan, T., Grimmond, C.S.B., Grossman-Clarke, S., Chen, F., Tewari, M., Manning, K., Martilli, A., Kusaka, H., Best, M., 2010. Trade-offs and responsiveness of the single-layer urban canopy parametrization in WRF: An offline evaluation using the MOSCEM optimization algorithm and field observations. Q. J. Roy. Meteor. Soc. 136(649), 997-1019.

Meehl, G.A., Tebaldi, C., 2004. More intense, more frequent, and longer lasting heat waves in the 21st century. Science 305, 994-997.

Miao, S., Chen, F., LeMone, M.A., Tewari, M., Li, Q., Wang, Y., 2009. An observational and modeling study of characteristics of urban heat island and boundary layer structures in Beijing. J. Appl. Meteorol. Clim. 48(3), 484-501.

Mirzaei, P.A., Haghighat, F., 2010. Approaches to study urban heat island–abilities and limitations. Build. Environ. 45(10), 2192-2201.

Mlawer, E.J., Steven, J.T., Patrick, D.B., Iacono, M.J., Clough, S.A., 1997. Radiative transfer for inhomogeneous atmospheres: RRTM, a validated correlated–k model for the longwave. J. Geophys. Res. 102, 16663–16682.

Oke, T.R. 1973. City size and the urban heat island. Atmos. Environ. 7, 769–779.

Oke, T.R., 1982. The energetic basis of the urban heat island. Q. J. Roy. Meteor. Soc. 108(455), 1-24.

Phelan, P.E., Kaloush, K., Miner, M., Golden Jay, Phelan B. Silva H. Taylor R.A. 2015. Urban heat island: mechanisms, implications, and possible remedies. Annu. Rev. Env. Resour. 40, 285-307.

Pineda, N., Jorba, O., Jorge, J., Baldasano, J., 2004. Using NOAA AVHRR and SPOT VGT data to estimate surface parameters: application to a mesoscale meteorological model. Int. J. Remote Sens. 25, 129-143.

Rizwan, A.M., Dennis, L.Y.C., Liu, C., 2008. A review on the generation, determination and mitigation of Urban Heat Island. J. Environ. Sci. 20, 120-128.

Ryu, Y.H., Baik, J.J. 2012. Quantitative analysis of factors contributing to urban heat island intensity. J. Appl. Meteorol. Clim. 51(5), 842-54.

Sannier, C., Gallego, J., Dahmer, J., Smith, G., Dufourmont, H., Pennec, A., 2016. Validation of Copernicus high resolution layer on imperviousness degree for 2006, 2009 and 2012. Proceedings of the International Symposium on Spatial Accuracy Assessment in Natural Resources and Environmental Sciences, Montpellier, France, 5-8.

Salamanca, F., Martilli, A., Yagüe, C., 2012. A numerical study of the Urban Heat Island over Madrid during the DESIREX (2008) campaign with WRF and an evaluation of simple mitigation strategies. Int. J. Climatol. 32(15), 2372-2386.

San José, R., Pérez, J.L., González, R.M., 2013. Very High Resolution Urban Simulations with WRF/UCM and CMAQ over European Cities. Urban Environment. Springer, Dordrecht, 293-301.

Schatz, J., Kucharik, C.J., 2014. Seasonality of the urban heat island effect in Madison, Wisconsin. J. Appl. Meteorol. Clim. 53(10), 2371-2386.

Schatz, J., Kucharik, C.J., 2015. Urban climate effects on extreme temperatures in Madison, Wisconsin, USA. Environ. Res. Lett. 10(9), 094024.

Schubert, S., Grossman-Clarke, S., 2013. The Influence of green areas and roof albedos on air temperatures during Extreme Heat Events in Berlin, Germany. Meteorol. Z. 22(2), 131-143.

Schwarz, N., Lautenbach, S., Seppelt, R., 2011. Exploring indicators for quantifying surface urban heat islands of European cities with MODIS land surface temperatures. Remote Sens. Environ. 115(12), 3175-3186.

Stewart, I.D., 2011. A systematic review and scientific critique of methodology in modern urban heat island literature. Int. J. Climatol. 31(2), 200-217.

Stewart, I.D., Oke, T.R. 2012. Local climate zones for urban temperature studies. B. Am. Meteorol. Soc. 93(12), 1879-1900.

Tan, J., Zheng, Y., Tang, X., Guo, C., Li, L., Song, G., Zhen, X., Yuan, D., Kalkstein, A.J., Li, F., Chen, H., 2010. The urban heat island and its impact on heat waves and human health in Shanghai. Int. J. Climatol. 54(1), 75-84.

Tewari, M., Chen, F., Wang, W., Dudhia, J., LeMone, M.A., Mitchell, K., Ek, M., Gayno, G., Wegiel, J., Cuenca, R.H., 2004. Implementation and verification of the unified NOAH land surface model in the WRF model. 20th conference on weather analysis and forecasting/16th conference on numerical weather prediction, 11-15.

Tewari, M., Chen, F., Kusaka, H., Miao, S., 2007. Coupled WRF/Unified Noah/urban-canopy modeling system. NCAR WRF Documentation, NCAR, Boulder, 122. http://citeseerx.ist.psu.edu/viewdoc/download?doi=10.1.1.468.3545&rep=rep1&type=pdf

Vahmani, P., Hogue, T.S., 2015. Urban irrigation effects on WRF-UCM summertime forecast skill over the Los Angeles metropolitan area. J. Geophys. Res. Atmos. 120(19), 9869-9881.

Wolter, M. 2016. Implementierung und Anpassung des WRF-Modells für Berlin & projektbezogene Ableitung der Straßenoberflächentemperatur. Master thesis, Freie Universität Berlin, Germany.

Yang, X., Leung, L.R., Zhao, N., Zhao, C., Qian, Y., Hu, K., Liu, X., Chen, B., 2017. Contribution of urbanization to the increase of extreme heat events in an urban agglomeration in east China. Geophys. Res. Lett. DOI: 10.1002/2017GL074084.

Zauri, R., Schiaroli, R., Leonardi, F.G., Berni, N., 2010. Numerical weather prediction models' temperature post-processing in heat wave early warning in Umbria: a case study and preliminary results. Ital. J. Agrometeorol. 15(3), 43-60.

Zhang, P., Imhoff, M.L., Bounoua, L., Wolfe, R.E., 2012. Exploring the influence of impervious surface density and shape on urban heat islands in the northeast United States using MODIS and Landsat. Can. J. Remote Sens. 38(4), 441-451.

Zhang, P., Imhoff, M.L., Wolfe, R.E., Bounoua, L., 2010. Characterizing Urban Heat Islands of Global Settlements Using MODIS and Nighttime Lights Products. Can. J. Remote

Sens. 36(3), 185-196.

Zhao, L., Lee, X., Smith, R.B., Oleson, K., 2014. Strong contributions of local background climate to urban heat islands. Nature 511, 216-219.

Zhong, S., Qian, Y., Zhao, C., Leung, R., Wang, H., Yang, B., Fan, J., Yan, H., Yang, X., Liu, D., 2017. Urbanization-induced urban heat island and aerosol effects on climate extremes in the Yangtze River Delta region of China. Atmos. Chem. Phys. 17(8), 5439-5457.

Zhou, B., Rybski, D., Kropp, J.P., 2017. The role of city size and urban form in the surface urban heat island. Sci. Rep. 7(1), 4791.

Paper IV

This article has been published on “Science of the Total Environment”. It is available at https://doi.org/10.1016/j.scitotenv.2018.04.254. This paper was attached below with kind permission from the journal.

Citation: Li H, Meier F, Lee X, Chakraborty T, Liu J, Schaap M, Sodoudi S. 2018. Interaction between urban heat island and urban pollution island during summer in Berlin. *Science of the Total Environment* 636:818-828.

Author Contributions: Li H. designed the research, analyzed the data, and draft the manuscript. Sodoudi S. contributed ideas to the research design and the discussion of results, reviewed the manuscript, and supervised the study. Meier F. provided radiation data at TUB, contributed to the discussion of the results, and reviewed the manuscript. Lee X. and Chakraborty T. provided technical support of the methodology, joined the discussion of the results, and reviewed the manuscripts. Liu J. and Schaap M. contributed ideas to the discussion of the results and reviewed the manuscript.

Interaction between urban heat island and urban pollution island during summer in Berlin

Huidong Li[1], Fred Meier[2], Xuhui Lee[3], Tirthankar Chakraborty[3], Junfeng Liu[4], Martijn Schaap[1,5], Sahar Sodoudi[1*]

1 Institute of Meteorology, Freie Universität Berlin, Berlin, Germany

2 Institute of Ecology, Technische Universität Berlin, Berlin, Germany

3 School of Forestry & Environmental Studies, Yale University, New Haven, USA

4 College of Urban and Environmental Sciences, Peking University, Beijing, China

5 Department Climate, Air and Sustainability, TNO, Utrecht, the Netherlands

Abstract

Urban Heat Island (UHI) and Urban Pollution Island (UPI) are two major problems of the urban environment and have become more serious with rapid urbanization. Since UHI and UPI can interact with each other, these two issues should be studied concurrently for a better urban environment. This study investigated the interaction between the UHI and UPI in Berlin, through a combined analysis of in-situ and remote sensing observations of aerosols and meteorological variables in June, July, and August from 2010 to 2017. The atmospheric UHI (AUHI), surface UHI (SUHI), atmospheric UPI (AUPI), and near-surface UPI (NSUPI) were analyzed. The SUHI and AUPI are represented by the remote sensing land surface temperature (LST) and aerosol optical depth (AOD), and the AUHI and NSUPI are represented by the in-situ air temperature and Particulate Matter (PM10) concentrations. The study area shows spatial consistency between SUHI and AUPI, with higher LST and AOD in the urban areas. UHI strengthens the turbulent dispersion of particles in the urban areas, decreasing the NSUPI. The NSUPI intensity shows a negative relationship with the AUHI intensity, especially at night with a correlation coefficient of −0.31. The increased aerosols in urban atmosphere reduce the incoming solar radiation and increase the atmospheric longwave radiation in the urban areas. The response of the surface to the change of absorbed radiation is

strong at night and weak during the day. This study estimates that the SUHI intensity is enhanced by around 12% at clear night by the increased absorbed radiation in the urban areas using an attribution method. The goal of this paper is to strengthen the understanding of the interactive influence between UHI and UPI and provide a basis for designing mitigation strategies of UHI and UPI.

1. Introduction

Intensive change of land use and emissions of air pollutants are two of the most important aspects of human activities in urban areas (McDonnell and MacGregor-Fors, 2016). The change of land surface from natural to impervious alters surface properties, resulting in lower albedo, higher Bowen ratio (ratio of sensible and latent heat flux), and larger energy storage of the surface in urban areas. As a result, urban areas produce warmer temperatures than the surrounding rural areas, which is called Urban Heat Island (UHI) phenomenon (e.g. Rizwan et al., 2008; Chakraborty et al., 2017). Meanwhile, the combustion of fossil fuels from factories, cars and other transportation means, as well as the daily human behaviour in cities emit a large number of pollution particles into the urban atmosphere (e.g. Ohara et al., 2007; Bonn et al., 2016). Thus, the urban atmosphere has more pollution particles than the rural atmosphere, which is called Urban Pollution Island (UPI) phenomenon (Crutzen, 2004). UHI increases the heat stress of city dwellers (e.g. Gabriel and Endlicher, 2011), while UPI increases the exposure of people to air pollutants (e.g. Monn and Becker, 1999; Han and Naeher, 2006). Furthermore, the superposition of heat stress and air pollution makes individuals more susceptible to the effect of each respective threat (e.g. Lai and Cheng, 2010; Meng et al., 2012; Burkart et al., 2013).

UHI and UPI can interact with each other. UHI-related warm temperatures can promote the dispersion of aerosol particles to higher atmospheric boundary level by increasing turbulent mixing (Sarrat et al., 2006). A temperature reduction in urban areas could decrease the rate of turbulent mixing and the height of mixing layer (Fallmann et al., 2016), leading to higher near-surface concentrations of PM10 (Fallmann, 2014). In turn, UPI-related increased aerosols in the urban atmosphere can generate larger radiative forcing. On the one hand, the increased aerosols can scatter more solar radiation back to space and reduce solar radiation

reaching the urban surface (e.g. Jin et al., 2010; Wang et al., 2015). On the other hand, the increased aerosols can trap more earth-emitted infrared radiation and re-emit more longwave radiation to the urban surface (e.g. Lubin and Simpson, 1994; Cao et al., 2016). The UPI-induced larger radiative forcing in urban areas affects the urban thermal environment and changes the UHI. Cao et al. (2016) reported that the haze in semi-arid Chinese cities enhanced the surface UHI intensity by 0.7 K at night.

Considering the interaction of UHI and UPI is important for a comprehensive understanding of the urban environment. However, most of the previous studies on UHI and UPI were conducted separately. Insufficient knowledge of the interaction between UHI and UPI inhibits the development of integrative mitigation strategies. Nowadays, fast urbanization process further strengthens UHI and UPI (e.g. Wei and Ye, 2014; AAAS, 2016). The interactive impacts of growing UHI and UPI are becoming a new direction for future studies (Crutzen, 2004). Baklanov et al. (2016) reviewed the previous studies on the complex interactions between climate, air quality, and megacities, and addressed the importance of the integrated studies of urban climate and air pollution in the changing climate. Recent European project MEGAPOLI focused on the feedbacks and interlinkages between climate change and regional air quality related to megacities (Baklanov et al., 2010). In China, the study of the interaction between air pollution and the physical state of the atmospheric boundary layer was taken as a priority study area of boundary layer meteorology (Lee et al., 2015). The modelling of urban air pollution and climate interactions was widely discussed in the 9th International Conference in Air Quality - Science and Application (Sokhi et al., 2017).

In this study, we attempted to connect UHI and UPI and carried out an integrated study of these two problems in the city of Berlin, Germany. In-situ and remote sensing observations of aerosols and meteorological variables in June, July, and August from 2010 to 2017 were collected. The atmospheric UPI (AUPI), near-surface UPI (NSUPI), atmospheric UHI (AUHI), and surface UHI (SUHI) were analyzed. The AUPI describes the urban-rural difference of the aerosol optical depth (AOD) from remote sensing observation, and the NSUPI describes the urban-rural difference of the near-surface aerosol concentrations characterized by the in-situ observation of Particulate Matter (PM10). The AUHI describes

the urban-rural difference of the air temperature from in-situ observation, and the SUHI describes the urban-rural difference of the land surface temperature (LST) from remote sensing observation. The study consists of three sections. Firstly, the relationship between the SUHI and AUPI in spatial variations was investigated using remote sensing data. Secondly, the impact of the AUHI on the NSUPI was examined using in-situ observations. Thirdly, the impact of the AUPI on the radiation transfer was studied by comparing the incoming solar radiation and atmospheric longwave radiation between the urban and rural areas. Moreover, the response of the SUHI to the urban-rural difference of the absorbed radiation was analyzed using an attribution method (Cao et al., 2016). Given the strong UHI (Fenner et al., 2014) and the good quality of remote sensing observation under cloudless conditions in the summer of Berlin (Li et al., 2018), this study only focuses on the summer period in June, July, and August. The goal of this study is to improve the understanding of the interactive influence between urban thermal environment and air pollution, and provide a scientific basis for the mitigation of these two problems.

2. Study area, datasets, and methodology

2.1. Study area

The study area is Berlin, the capital city of Germany. Berlin (52.34°–52.68° N, 13.10°–13.77° E) is located in Northeastern Germany and covers an area of around 900 km^2. Berlin has a temperate maritime climate with the annual mean temperature of 9.5 °C and annual precipitation of 591 mm. Affected by the prevailing westerlies, the wind mainly comes from the west directions in summer (Fig. S1). Berlin has ~3.6 million inhabitants, with one-third living in the inner city. Based on Corine land cover datasets (Feranec et al., 2007), around 35% of the area is covered by buildings, and around 20% of the area is covered by transportation/infrastructure in Berlin (Fig. 1a). Most of the non-urban area is covered by forest and farmland. The large built-up area creates distinct AUHI (e.g. Fenner et al., 2014; Li et al., 2017) and SUHI in this city (e.g. Li et al., 2017, 2018). The UHI-enhanced heat wave has a negative impact on the health of the Berlin dweller (Gabriel and Endlicher, 2011; Scherer et al., 2014). Meanwhile, Berlin suffers from air pollution. The air quality cannot meet the standards of the European Union in terms of PM10 (Görgen and Lambrecht, 2007).

The local emissions are the dominant source of the elevated urban particulate number and mass concentrations (Bonn et al., 2016). The fine mode aerosols are the dominant component of PM10, accounting for around three-quarters of the observed PM10 mass. Road traffic is the major emission source, due to a large number of vehicles (Lutz, 2013) and a dense traffic network in Berlin (Fig. 1.b). In 2015, 1.37 million motor vehicles were registered in the city (389 cars per 1000 residents). The traffic intensity is high in the urban center and low in the rural areas. The urban-rural differences in the emissions and air pollutants are significant (Kuik et al., 2016).

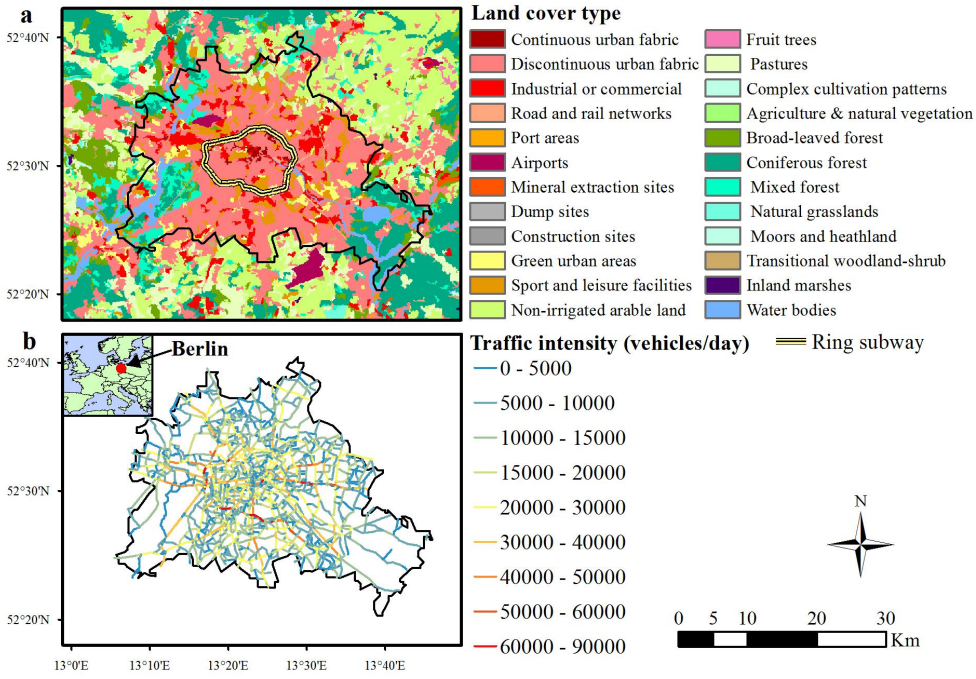

Fig. 1. Spatial patterns of the (a) land cover and (b) traffic intensity in the study area. The land cover data in (a) are Corine land cover data version 2012. The traffic intensity map in (b) is the average daily traffic volume version 2014, which comes from the FIS Broker of the Senate Department for Urban Development and the Environment, Berlin.

2.2. Datasets and processing

2.2.1. Remote sensing AOD and LST

Moderate Resolution Imaging Spectroradiometer (MODIS) observed AOD product (MYD04_3K) at a 3000 m resolution and LST product (MYD11_A1) at a 1000 m resolution (collection 006) by Aqua satellite were used in this study. The Aqua satellite passed over the

city of Berlin at UTC time around 11:50 in the daytime and 1:20 at night. MYD04_3K AOD data are derived from dark target algorithms at 550 nm (Munchak et al., 2013; Remer et al., 2013). The AOD data with the best quality (Flag = 3) were used in this study. Comparison of the MODIS AOD against sun photometer observations at station of Free University of Berlin shows a good agreement, with a correlation coefficient of 0.90 ($P<0.01$) and a RMSE of 0.05 (Fig. S2). MYD11_A1 LST data were retrieved using the generalized split-window algorithm (Wan and Dozier, 1996). The retrieval of LST was further refined by correcting bias resulting from cloud contamination and topographic differences (Wan, 2008). The collection 6 LST data achieve reliable quality with the standard deviation of errors <0.5 K (Wan, 2014). The AOD and LST data from 2010 to 2017 in June, July, and August were downloaded from the NASA website. In order to investigate the relationship of the spatial configurations of the AOD and LST, the LST data were reprojected to 3000 m resolution grids using the online post-processing tool on the NASA website. The post-processing tool supports the following operations: subset by dataset name, subset by geographic area of interest or shape, gridding swath data, reprojection to new map projection, mosaic, and reformat to different file formats. The detailed introduction of the online tool refers to https://ladsweb.modaps.eosdis.nasa.gov/tools-and-services/. The mean spatial patterns of AOD and LST were calculated using the images with more than three quarters of grids cloud free.

2.2.2. In-situ observations of PM10, air temperature, radiation, cloud, and wind

In-situ observed PM10, air temperature, incoming radiation, clouds, and wind speed were used in this study (Table 1). Hourly near-surface PM10 concentrations data from 2010 to 2015 were collected at twelve stations. Three rural background stations are located in the rural near city areas that are far away from anthropogenic emissions, three urban background stations are located in the urban areas that are influenced by the local anthropogenic emissions, but are far away from traffic emission sources, and six traffic stations are located on the urban areas close to traffic emissions. Detailed information about the PM10 observation stations refers to the study of Shahraiyni et al. (2015). Hourly 2 m air temperature data from 2010 to 2015 were collected at four stations (Potsdam, Schoenefeld, Tempelhof, and Fasanenstrasse). Hourly

incoming solar radiation data were collected at seven stations (FUB, Tegel, TUB, Wiener, HTW, Potsdam, and Lindenberg), and hourly incoming atmospheric longwave radiation data were collected at four stations (TUB, Wiener, Potsdam, and Lindenberg). The stations FUB, Tegel, TUB, Wienerstrasse, and HTW are located in the urban areas, while the stations Potsdam and Lindenberg are located in the near-city and far-city rural areas, respectively. Hourly cloud cover data were collected at two urban stations (Tegel and Dahlem) and two rural stations (Potsdam and Lindenberg). Hourly wind speed data were collected at Potsdam station. Summer (June, July, and August) observations were used in this study. The analysis was conducted for day and night, respectively. The daytime (5:00–21:00 CET) period and nighttime (22:00–4:00 CET) period were defined as the hours with and without solar radiation at Potsdam station, respectively. The geographic information of the stations and the time series of the observation data are listed in Table 1.

2.3. Methodology

2.3.1. Calculations of the intensities of AUHI and SUHI

The intensities of SUHI and AUHI quantify the urban-rural difference of the land surface temperature and air temperature, respectively. In this study, the former was calculated using remote sensing observations, and the latter was calculated using in-situ observations. The SUHI intensity was calculated as the difference of the mean MODIS LST of the urban grids within the ring subway and of the rural grids outside the border of Berlin (Fig. 1a), which were selected using the shape files of the ring subway and the city border through Matlab. The AUHI intensity was calculated as the difference of the mean air temperature at two urban stations (Fasanenstrasse and Tempelhof) and at two rural stations (Potsdam and Schoenefeld). Given the influence of strong wind to the advective transport of heat, the AUHI observed under wind speed faster than 3 m/s was omitted for analysis.

Table 1. The geographic information, operator, land cover, and time series of the in-situ observation data.

Variables	Stations	Operator*	Lon (E)	Lat (N)	Urban/Rural	Corine Land Cover	Time series
PM10	Grunewald	BLM	13.23	52.47	Rural background	Coniferous forest	2010-2015
	Buch	BLM	13.49	52.64	Rural background	Industrial or commercial	2010-2015
	Friedrichshagen	BLM	13.65	52.45	Rural background	Industrial or commercial	2010-2015
	Wedding	BLM	13.35	52.54	Urban background	Industrial or commercial	2010-2015
	Nansenstr	BLM	13.43	52.49	Urban background	Industrial or commercial	2010-2015
	Mitte	BLM	13.42	52.51	Urban background	Industrial or commercial	2010-2015
	Hardenbergplatz	BLM	13.33	52.51	Urban Traffic	Continuous urban fabric	2010-2013
	Steglitz	BLM	13.32	52.46	Urban Traffic	Industrial or commercial	2010-2015
	Mariendorf	BLM	13.39	52.44	Urban Traffic	Industrial or commercial	2010-2015
	Silbersteinstr	BLM	13.44	52.47	Urban Traffic	Industrial or commercial	2010-2015
	Friedrichshain	BLM	13.47	52.51	Urban Traffic	Industrial or commercial	2010-2015
	Karl-Marx-Str	BLM	13.43	52.48	Urban Traffic	Industrial or commercial	2010-2015
Radiation	FUB	FU	13.31	52.46	Urban	Discontinuous urban fabric	2010-2015
	Tegel	DWD	13.31	52.46	Urban	Airports	2016-2017
	HTW	HTW	13.52	52.46	Urban	Industrial or commercial	2017
	TUB	TU	13.33	52.51	Urban	Industrial or commercial	2014-2017
	Wiener	TU	13.43	52.50	Urban	Discontinuous urban fabric	2014-2017
	Potsdam	DWD	13.06	52.38	Rural	Green urban areas	2010-2017
	Lindenberg	DWD	14.12	52.21	Rural	Discontinuous urban fabric	2010-2017
Cloud	Dahlem	FU	13.31	52.46	Urban	Industrial or commercial	2010-2017
	Tegel	Same as Tegel above					2010-2017
	Potsdam	Same as Potsdam above					2010-2017
	Lindenberg	Same as Lindenberg above					2010-2017
Air temperature	Fasanenstrasse	FU	13.34	52.51	Urban	Industrial or commercial	2010-2017
	Tempelhof	DWD	13.40	52.47	Urban	Sport and leisure facilities	2010-2017
	Schoenefeld	DWD	13.53	52.38	Rural	Airports	2010-2017
	Potsdam	Same as Potsdam above					2010-2017
Wind	Potsdam	Same as Potsdam above					2010-2017

*BLM= Berliner Luftgüte Messnetz, http://www.berlin.de/senuvk/umwelt/luftqualitaet/luftdaten/index.shtml; FU = Freie Universität Berlin, http://www.geo.fu-berlin.de/en/met/service/stadtmessnetz/index.html; DWD = Deutscher Wetterdienst, German Weather Service, www.dwd.de; HTW = Hochschule für Technik und Wirtschaft, http://wetter.htw-berlin.de/; TU = Technische Universität Berlin, https://www.klima.tu-berlin.de/index.php?show=forschung_dch_messnetz&lan=en.

2.3.2. Calculations of the intensities of AUPI and NSUPI

The intensities of AUPI and NSUPI quantify the urban-rural difference of the AOD and near-surface PM10, respectively. In this study, the former was calculated using remote sensing observations, and the latter was calculated using in-situ observations. The AUPI intensity was calculated as the difference of mean MODIS AOD of the urban grids within the ring subway and of the rural grids outside the border of Berlin (Fig. 1a), which were selected using the shape files of the ring subway and the city border through Matlab. The NSUPI intensity was calculated as the difference of the mean PM10 at urban stations and at rural stations. The urban areas have urban background stations and traffic stations. The NSUPI intensity calculated using urban background station data was defined as NSUPI_B intensity, while the NSUPI intensity calculated using traffic station data was defined as NSUPI_T intensity. The NSUPI_B intensity reflects the integrated influence of anthropogenic emissions on the near-surface PM10 concentrations, while the NSUPI_T reflects the strong impact of traffic emissions. Given the influence of strong wind to the advective transport of aerosol particles, the NSUPI observed under strong wind conditions with speed >3m/s was omitted for analysis.

2.3.3. Calculation of the change of SUHI intensity caused by the urban-rural difference of incoming radiation

The change of SUHI intensity caused by the urban-rural difference of incoming radiation was calculated using an attribution method. The attribution method was developed to investigate the mechanism that caused the change of surface temperature by Lee et al. (2011). Zhao et al. (2014) further developed this method for SUHI studies, and investigated the attributions that caused SUHI for cities across North America. Cao et al. (2016) studied the impact of haze on SUHI intensity in China using this method. The incoming radiations in urban and rural areas usually show difference due to UPI-related different loading aerosols, which has an impact on the UHI. The physical mechanisms of the impact of UPI on the radiation and UHI were discussed in Sections 4.2 and 4.3. Referring to the study of Cao et al. (2016), the change of SUHI intensity (ΔSUHII, K) caused by the urban-rural difference of incoming radiation was calculated as

$$\Delta SUHII = \frac{\lambda_0}{1+f}\left[(1-\alpha_u)S_u - (1-\alpha_r)S_r + L_u - L_r\right] \quad (1)$$

where S_u and S_r, and L_u and L_r are the incoming solar radiation and atmospheric longwave radiation in the urban and rural areas, respectively. a_u and a_r are the surface albedo of urban and rural areas. λ_0 is the local climate sensitivity ($\lambda_0 = 1/4\sigma T_s^3$), and f is energy redistribution factor and is defined as

$$f = \frac{\rho C_p}{4 r_a \sigma T_s^3}(1+\frac{1}{\beta}) \quad (2)$$

where T_s is surface temperature; σ is Stephan Boltzmann constant, 5.67×10^{-8} W/(m^2 K^4); C_p is the specific heat of air at constant pressure, 1004 J/(Kg K); ρ is air density; r_a is aerodynamic resistance to heat diffusion; β is Bowen ratio.

In this study, the radiation data come from in-situ observations at urban and rural stations (Table 1). The radiation data were filtered under clear-sky conditions that the cloud fraction at all stations was less than or equal to 2 oktas and the cloud fraction at the rural stations was equal to or larger than that at the urban stations. In order to eliminate the impact of small clouds on the radiation observations, the radiation data with the urban-rural difference outside 5% and 95% at each hour were omitted for the calculation of hourly mean values. The values of a_u and a_r were calculated using MODIS Albedo 16-Day L3 Global product (MCD43C3) collection 6 at a 0.05 degree resolution (Schaaf et al., 2002). MODIS Albedo data from 2014 to 2017 in summer (June, July, and August) were used. MODIS albedo was compiled based on the bidirectional reflectance distribution function (BRDF) and includes Black-sky (a_{bsa}) and White-sky (a_{wsa}) albedo. The integrated albedo was calculated as

$$\alpha = (1-bw)\alpha_{bsa} + bw\alpha_{wsa} \quad (3)$$

where bw is the ratio of diffuse solar radiation to direct solar radiation. The value of bw (0.27) was calculated using the observed diffuse and global solar radiation under clear-sky conditions in June, July, and August during 2014-2017 at Potsdam station. The mean albedo over urban (0.12) and rural (0.14) areas were calculated using the albedo within the ring

subway and outside the border of Berlin, respectively, consistent with the calculation of SUHI intensity (Figure S2). The values of λ_0 and f were calculated using MERRA 2 reanalysis data (Gelaro et al., 2017) in June, July, and August during 2014-2017. Referring to the study of Zhao et al. (2014), the r_a was calculated as

$$r_a = \frac{\rho C_p (T_S - T_a)}{SH} \tag{4}$$

and the β was calculated as

$$\beta = SH / LH \tag{5}$$

where T_a is air temperature. SH and LH are sensible heat flux and latent heat flux. The calculations of r_a and β were performed for the whole day, with rainy and cloudy hours omitted. The values of ρ, T_s, T_a, SH, LH, precipitation, and cloud come from MERRA 2 reanalysis data at the grid that Berlin is located. In order to eliminate the outliers, the resulted r_a, β, and f outside 5% and 95 % were omitted for the calculation of hourly mean values. The calculation and statistical work were conducted using Matlab.

3. Results

3.1. Relationship between the SUHI and AUPI in spatial variations

The relationship between the SUHI and AUPI in spatial variations was analyzed using MODIS LST and AOD. High AOD values are mainly located in the central city within the ring subway (Fig. 2). The AOD in the surrounding rural areas is much lower than that in the urban areas. The study areas show an AUPI, with the intensity of 0.08. Meanwhile, the urban stations show higher PM10 concentrations than the rural stations. The spatial pattern of the PM10 concentrations is consistent with that of the AOD. The city is clearly a source of aerosols, due to the combined human activities, especially the traffic, which is the major emission source. Hence, the traffic stations show the highest PM10 concentrations. Besides, the spatial variation of aerosols is affected by wind. There is a plume in the downwind areas in the eastern Berlin, due to the prevailing westerly wind in summer (Fig. S1). Berlin also shows significant SUHI, with higher LST in the urban areas than in the rural areas (Fig. 3).

The SUHI intensities are 5.38 and 2.84 K for the daytime and nighttime, respectively. The SUHII during the day is higher than that at night, which is consistent with the previous studies (e.g. Schwarz et al., 2011; Li et al., 2017). The spatial patterns of the SUHI are similar with that of the AUPI. Generally, the LST shows a positive correlation with the AOD in spatial variations. This phenomenon is consistent with the study in other cities (Xu et al., 2013). The correlation coefficient between the LST and AOD is 0.62 ($P<0.01$) during the day.

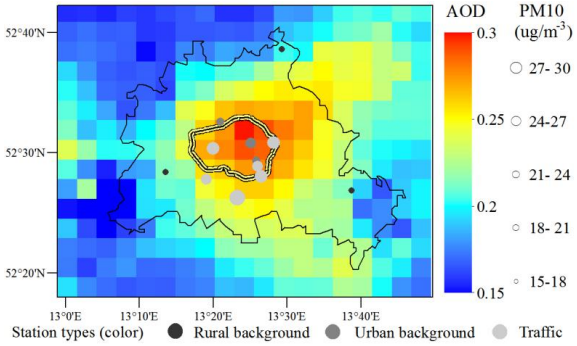

Fig. 2. Spatial patterns of the mean AOD and PM10 in July, July, and August from 2010 to 2017. The color and size of the circles show the types of the observation stations and the values of the observed PM 10 concentrations, respectively. The mean AOD were calculated using the images with more than three quarters of grids cloud free and the mean PM10 were calculated using the observations under wind speed less than 3m/s.

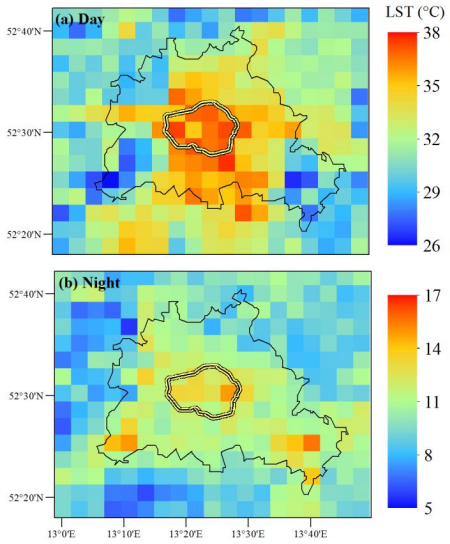

Fig. 3. Spatial patterns of the mean LST (a) during the day and (b) at night in June, July, and August from 2010 to 2017. The mean LST were calculated using the images with more than three quarters of grids cloud free.

3.2. The influence of AUHI on NSUPI

The diurnal variations of the mean PM10 concentrations of three types of observation stations were compared (Fig. 4). The diurnal variation of the PM10 concentrations of the rural background stations shows larger values at night and smaller values during the day. Atmospheric turbulence controls the aerosol concentrations at the rural background stations. Strong turbulent mixing during the day boosts the dispersion of aerosol particles and vice versa at night. The PM10 concentrations at the urban background stations and traffic stations are jointly controlled by turbulent mixing and anthropogenic emissions. At the urban background stations, turbulent mixing plays a dominant role in the PM10 concentrations, with smaller values in the daytime than in the nighttime. But there are several peaks during the day, due to the effect of emissions. At the traffic stations, emissions from intensive vehicles play a dominant role in the aerosol concentrations. Especially during the heavy traffic period in the morning, the PM10 concentrations of the traffic stations reach peak values. The influence of the anthropogenic emissions on the aerosol concentrations mainly happens during the day. Generally, the difference of the mean PM10 concentrations among the three types of stations is larger in the daytime than in the nighttime.

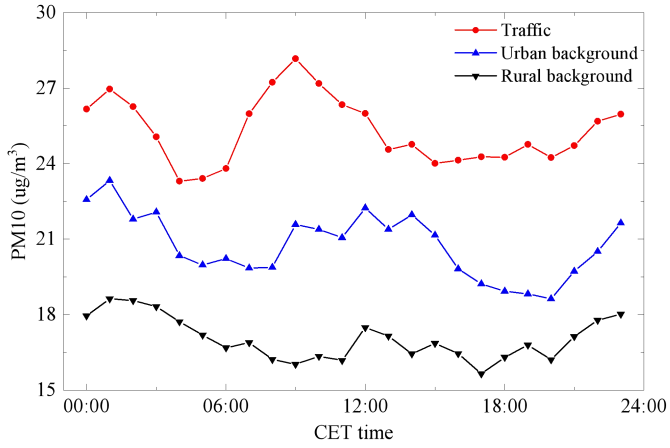

Fig. 4. Diurnal variations of the mean PM10 observed at traffic stations (red), urban background stations (blue), and rural background stations (black) in June, July, and August from 2010 to 2015. The mean PM10 were calculated using the observations under wind speed less than 3m/s.

UHI-related warm temperatures could decrease aerosol concentrations in urban areas and NSUPI by strengthening turbulent mixing. The NSUPI intensity shows a negative correlation with the AUHI intensity for both daytime and nighttime (Fig. 5). The NSUPI intensity decreases with the increase in the AUHI intensity. The correlation coefficients between NSUPI_B intensity and NSUPI_T intensity and AUHI intensity are −0.17 and −0.15 ($P<0.01$) during the day, and −0.31 and −0.30 （$P<0.01$) at night. The impact of the anthropogenic emissions on the NSUPI was not excluded from the correlation analysis in Fig. 5. Therefore, the correlation coefficients are not high. The nighttime shows a better NSUPI-AUHI relationship due to the less disturbance from anthropogenic emissions, as most of the anthropogenic emissions stop at night. Moreover, the relationship between NSUPI_B intensity and AUHI intensity is slightly better than the relationship between NSUPI_T intensity and AUHI intensity, because the urban background stations are less affected by traffic emissions.

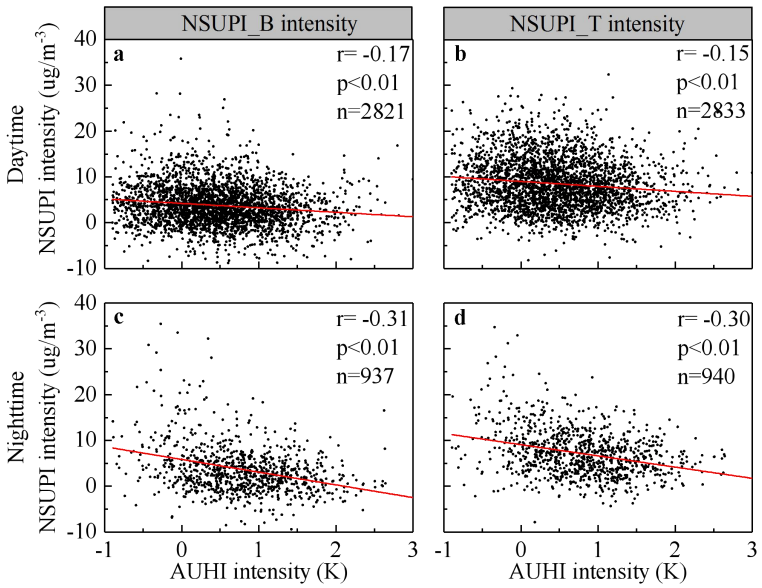

Fig. 5. Scatter plots of the NSUPI intensity and AUHI intensity for daytime (upper panels) and nighttime (lower panels) in June, July, and August from 2010 to 2015. Subplots (a) and (c) show NSUPI_B intensity, while subplots (b) and (d) show NSUPI_T intensity. The PM10 data observed under wind speed less than 3m/s were shown here.

3.3. Comparison of the incoming solar radiation and atmospheric longwave radiation between urban and rural areas

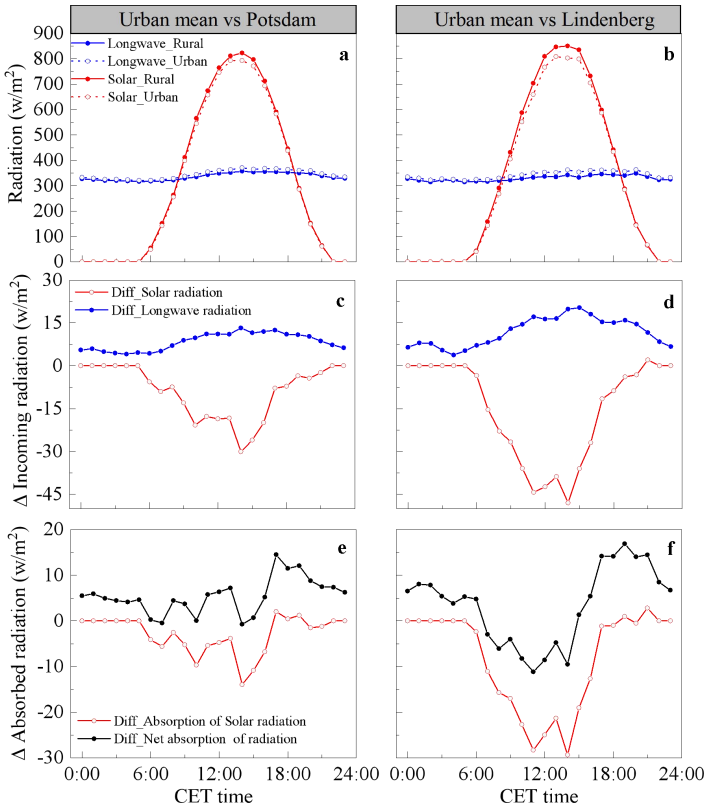

Fig. 6. Diurnal variations of the mean incoming solar radiation and atmospheric longwave radiation (upper panels a and b), and their urban-rural difference (middle panels c and d), and the urban-rural difference of the net absorption of radiation (lower panels e and f) in June, July, and August from 2010 to 2017. Subplots (a), (c) and (e) show the comparison between urban stations and Potsdam station, and subplots (b), (d), and (f) show the comparison between urban stations and Lindenberg station. The urban curves in subplot (a) and (b) are mean radiation observed at all urban stations in Table 1. The mean values at each hour were calculated under clear sky conditions with cloudy time omitted.

Increased aerosols in urban areas affect the radiation transfer process. Under the clear sky conditions, urban stations show lower solar radiation and higher atmospheric longwave radiation than the rural stations Potsdam (Fig. 6a) and Lindenberg (Fig. 6b). The urban-rural differences reach −30.07 and − 48.06 W/m^2 for the solar radiation, and 13.26 and 20.38 W/m^2 for the atmospheric longwave radiation in the midday, respectively (Fig. 6c and d). The

difference between urban stations and Lindenberg station is larger than the difference between urban stations and Potsdam station because the Lindenberg station is less affected by anthropogenic emissions due to its longer distance to urban areas than the Potsdam station. The decrease of the incoming solar radiation in urban areas is larger than the increase of the atmospheric longwave radiation. However, the absorption of solar radiation by the ground is affected by the surface albedo. The urban areas with lower albedo can absorb solar radiation more efficiently than the rural areas. The urban-rural difference of the absorbed solar radiation becomes much smaller than the urban-rural difference of incoming solar radiation (Fig. 6e and f) and is even smaller than the urban-rural difference of the atmospheric longwave radiation sometimes. As a result, the urban-rural differences of the net absorption of radiation, $(1-a_u)S_u-(1-a_r)S_r+L_u-L_r$, become rather small and even positive at some hours during the day (Fig. 6e and f).

3.4. The ΔSUHII caused by the urban-rural difference of net absorption of radiation

The urban-rural difference of the net absorption of radiation can affect the SUHI. Based on Eq. (1), the sensitivity of the surface to the change of net absorption of radiation is controlled by $\lambda_0/(1+f)$. The λ_0 has a small daily range from 0.16 to 0.19 (K m2)/W (Fig. 7a). The f is the dominant factor of the surface sensitivity. The f shows a significant diurnal variation, with large values during the day, while low values at night (Fig. 7b). The values of f are mainly determined by the aerodynamic resistance and Bowen ratio. During the day, the low aerodynamic resistance produced high f, while at night, the high aerodynamic resistance and the negative Bowen ratio produced low f (Fig. S4). Especially in the evening from 18:00 to 21:00 CET, the values of f change drastically, because of the transition of negative and positive Bowen ratio with small absolute values. The calculated f during this period was omitted for the following analysis. At night, the values of f are around 2.06, which are between the values of humid and semi-humid zones of China (Cao et al., 2016). The daily mean f is 7.80, similar to the study of Bright et al. (2017) in the same latitude. The $\lambda_0/(1+f)$ shows large values at night and low values during the day (Fig. 7c). Affected by the drastic change of f, the $\lambda_0/(1+f)$ shows extreme values in the evening.

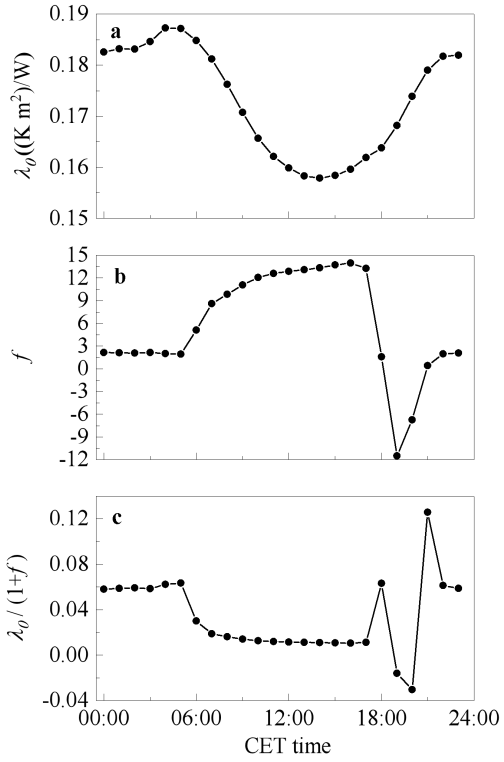

Fig. 7. Diurnal variations of the (a) λ_0, (b) f, and $\lambda_0/(1+f)$ in summer.

The diurnal variation of the calculated ΔSUHII is presented in Fig. 8. Given the extreme values of $\lambda_0/(1+f)$ from 18:00 to 21:00 CET could lead to unreasonable ΔSUHII, the calculation results during this period are not shown here and are excluded for the calculation of mean values. The ΔSUHII shows positive values at night. The mean values of $\Delta SUHII_{Potsdam}$ and $\Delta SUHII_{Lindenberg}$, are 0.33 ± 0.09 and 0.40 ± 0.09 K, respectively (Table 2). Potsdam station is located in the rural areas, which are selected for the calculation of SUHI intensity. The mean $\Delta SUHII_{Potsdam}$ accounts for 12 ± 3% of the nighttime SUHI intensity in Fig. 3b. The SUHI intensity is enhanced at night, consistent with the study of Cao et al. (2016). The daytime ΔSUHII is rather minor, with mean values of 0.06 ± 0.07 and 0.00 ± 0.13 K for the $\Delta SUHII_{Potsdam}$ and $\Delta SUHII_{Lindenberg}$,, respectively, because of the offset of the absorbed solar radiation and longwave radiation (Fig. 6eandf) and low $\lambda_0/(1+f)$ during the day (Fig. 7c). Compared to the high daytime SUHI intensity, the daytime ΔSUHII is negligible.

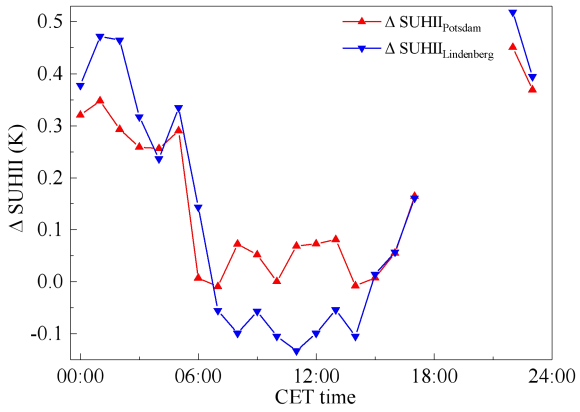

Fig. 8. Diurnal variation of the ΔSUHII in summer.

Table 2. The ΔSUHII caused by the urban-rural difference of net absorption of radiation in different time periods (mean±Standard_deviation, K).

Time	$\Delta SUHII_{Potsdam}$	$\Delta SUHII_{Lindenberg}$
Day	0.06±0.07	-0.00±0.13
Night	0.33±0.09	0.40±0.09

4. Discussion

4.1. The mechanism for the impact of UHI on NSUPI

Atmospheric turbulence plays a dominant role in the upward transport of aerosol particles in the atmospheric boundary layer (Sarrat et al., 2006). Wagner and Schäfer (2017) reported a strong correlation between pollution concentrations and boundary layer height. UHI-related warm temperatures in urban areas strengthen turbulent mixing and increase the height of urban boundary layer (e.g. Dupont et al., 1999; Fallmann et al., 2016). Sarrat et al. (2006) found that the urban boundary layer was two to three times higher than the rural one over Paris. Epstein et al. (2017) found that the urban boundary layer height decreased by 60% with AUHI intensity decreased by 0.35 K. Strong turbulence boosts the dispersion of aerosol particles inside a deeper boundary layer, decreasing the aerosol concentrations in urban areas and weakening the NSUPI intensity. At night, the particles in the rural atmosphere are usually trapped in a near-surface layer, due to the temperature inversion (Oke, 1995). While there is still a mixing layer below temperature inversion in the urban atmosphere, due to the release of

the stored energy in the urban surface (Godowitch et al., 1985; Gedzelman et al., 2003). The turbulent mixing can weaken the accumulation of aerosol particles in the near surface level at night, decreasing the nighttime near-surface aerosol concentrations in urban areas. Rendón et al. (2014) reported that urbanization could break up temperature inversion, improving air quality.

However, it should be noted that our results about AUHI-NSUPI relationship are achieved using the data observed in summer, when the atmosphere is unstable and the turbulent mixing is strong. In winter, the atmosphere is relatively stable with weak turbulence. The relationship between AUHI on NSUPI may become weak then, because of the small urban-rural difference of the intensity of turbulent mixing and of the height of atmospheric boundary layer. Meanwhile, it should be noted that the NSUPI is jointly affected by anthropogenic emissions and UHI. The correlation analysis between NSUPI and UHI intensity in this study did not exclude the impact of emissions, resulting in the low correlation coefficients, especially during the day (Fig. 5). All these problems need further studies in the future. Additionally, this study defined NSUPI using PM10 data. Besides PM10, other indicators, such as TSP, also can represent the characteristic of aerosol concentrations and can be used to define NSUPI. The definition of NSUPI needs further study.

4.2. The mechanism for the urban-rural difference of incoming radiation

Atmospheric aerosols can affect both the incoming solar radiation and atmospheric longwave radiation on the surface (Haywood and Boucher, 2000). On the one hand, aerosol particles scatter solar radiation back to the space, reducing the solar radiation reaching the surface (e.g. Jin et al., 2010). On the other hand, aerosol particles absorb infrared radiation emitted by the earth surface, especially within the longwave atmospheric window (wavelength range 8–12 mm) (e.g. Lubin and Simpson, 1994; Vogelmann et al., 2003), and some aerosol particles, such as black carbon, absorb solar radiation (e.g. Gatari and Boman, 2003; Ramanathan and Carmichael, 2008), heating the atmosphere. The heated atmosphere re-emits more longwave radiation to the surface. The dense aerosols in the urban atmosphere can reduce more solar radiation and increase more atmospheric longwave radiation, compared to the thin aerosols in rural areas. Additionally, the warmer urban surface could emit larger upward longwave

radiation, promoting the heating of the atmosphere through the absorption of the aerosols and the following re-emission of the longwave radiation (Oke, 1982). As a result, urban areas receive less solar radiation and more atmospheric longwave radiation, as shown in Fig. 6. The similar phenomena were also reported by other studies. Estournel et al. (1983) found that the urban site received 30 W/m^2 less solar radiation and 15 to 25 W/m^2 more longwave radiation than the rural site during cloudless days in Toulouse. Jauregui and Luyando (1999) reported that on average the Mexico City received 21.6% less solar energy than the rural surroundings on clear days during the dry season. Robaa (2009) found that the attenuation of solar radiation in the urban area was always higher than that in rural area in Greater Cairo region, and the urban-rural difference of the attenuation increased in the past years, because urbanization and industrialization processes produced more pollutants. Wang et al. (2015) reported that the monthly-averaged incoming solar radiation and longwave radiation at urban site was 3–20% lower and 3–15% higher than those at rural site in Beijing.

Urban surface allocates more heat to the atmosphere than natural surface, leading to the warmer atmosphere in urban areas than in rural areas (Oke, 1982). The UHI-related warm urban atmosphere may also strengthen the emission of atmospheric longwave radiation. Our observation data did not exclude this factor. However, UHI effect mainly exists within a thin layer near the ground and decreases fast with the increase of height due to the advection by strong wind in high-altitude (Chao, 1991). Rouse et al. (1973) and Tapper (1990) reported that the urban-rural difference of the mean atmosphere temperature of the boundary layer did not differ significantly. The urban-rural difference of the longwave radiation emission caused by the difference of the atmospheric temperature in the boundary layer was small. In our study, the urban-rural difference of the incoming longwave radiation did not increase with the increase of AUHII (Fig. S5). The larger urban-rural difference of the incoming longwave radiation appeared during the day, when the city had more loading aerosols, not at night, when the AUHI was strong (Fig. 6). The impact of the UHI-related warm atmosphere on the increase of the incoming longwave radiation in the urban areas may be rather limited.

This study only revealed the direct effect of aerosols on radiation transfer and its following effect on SUHI. The radiation data were filtered with the cloudless condition.

Nevertheless, aerosols also can affect radiation transfer processes indirectly, by affecting the formation and development of clouds (Mahowald, 2011). The indirect effect of aerosols is more complicated than its direct effect and has some uncertainties (Lohmann and Feichter, 2005). The indirect radiative effect of aerosols on UHI needs further study.

4.3. The influence of urban-rural difference of incoming radiation on SUHI

The influence of the urban-rural difference of incoming radiation on SUHI is affected by the surface albedo and sensitivity of the surface to the change of absorbed radiation (Oke, 1982). During the day, the urban-rural difference of incoming solar radiation is usually larger than the urban-rural difference of incoming longwave radiation (e.g. Estournel et al., 1983; Wang et al., 2015). Our results also show this phenomenon (Fig. 6b and c). However, as the albedo of the urban surface is lower than that of the natural surface, the urban-rural difference of absorbed solar radiation is reduced (Fig. 6e and f). Then the offset of the absorbed solar radiation and longwave radiation makes the urban-rural difference of net radiation absorption rather small (Oke, 1982). Moreover, the sensitivity of the surface temperature to the change of absorbed radiation is weak during the day (Fig. 7). Thus, the change of daytime SUHI caused by the urban-rural difference of absorbed energy is rather limited. At night, only longwave radiative forcing exists and the urban areas absorb more energy. Furthermore, the nighttime energy redistribution factor is small, resulting in the strong response of the surface to the change of absorbed radiation. As a result, the nighttime SUHI is enhanced by the more absorbed radiation in urban areas, as also found in Chinese cities (e.g. Cao et al., 2016). It should be noted that the values of the ΔSUHII in Fig. 8 were only calculated for summer. In winter, the urban-rural difference of the incoming radiation may be very small because of the decrease of the magnitude of the radiation (Wang et al., 2015), in spite of the increase of urban aerosols. Nevertheless, the surface sensitivity to the change of radiation in winter is larger than that in summer (Bright et al., 2017). The winter ΔSUHII caused by the urban-rural difference of radiation needs further study.

5. Conclusions

This study aimed to enhance the understanding of the interactive influence between UHI and UPI during summer in the city of Berlin through a combined analysis of in-situ and remote sensing observations of aerosols and meteorological variables from 2010 to 2017. The study area showed both SUHI and AUPI. There was a positive correlation between the spatial configurations of the SUHI and AUPI, with a coefficient of 0.62 ($P<0.01$) during the day. UHI-related warm temperature promoted the turbulent dispersion of aerosol particles in the urban areas, decreasing the NSUPI. The NSUPI intensity showed a negative relationship with the AUHI intensity, especially at night. The increased aerosols in the urban areas reduced the incoming solar radiation and increased the atmospheric longwave radiation. The SUHI was more sensitive to the change of absorbed radiation at night than during the day. It was estimated that the SUHI was enhanced by around 12% by the increased absorbed radiation in the urban areas at clear night using an attribution method. During the day, the change of SUHI intensity caused by the change of the incoming radiation was negligible, due to the offset of the opposite change of solar radiation and atmospheric longwave radiation and the weak sensitivity of the surface.

Our results imply that the mitigation of UPI could decrease the urban-rural difference of the incoming radiation, contributing to the mitigation of UHI at night, while the mitigation of UHI may have a negative impact on the near-surface pollution concentrations. Additional, the reduction of pollutant emissions promotes the reduction of anthropogenic heat emission, which is a contribution to UHI (Taha, 1997). Decreasing the emissions of aerosol pollutants should be given priority for the improvement of urban thermal environment and air quality. On the contrary, designing mitigation strategies of UHI should be carefully treated and considers the consequent change of air quality. Strategies that are better for both urban thermal environment and air quality are preferable. Our study shows some insights regarding the interaction between UHI and UPI that provide starting points for urban planning authorities in order to design reasonable mitigation strategies. This study mainly focuses on the overall characteristics of the UHI and UPI and their interaction in a city scale. Other factors that may affect the UHI and UPI, such as urban texture, vegetation, and water bodies,

are not considered and need further studies in the future. The effects of these potential mitigation strategies of UHI and UPI need further evaluations using numerical modelling and other methods before practical application.

Acknowledgments

This research is supported by the China Scholarship Council. Authors would like to thank Dr. Ines Langer from Freie Universität Berlin for the radiation data at FUB station and the air temperature data at Fasanenstrasse station. Thanks Ralf Becker, Lionel Doppler, and the group radiation processes (MOL4) of the observatory DWD/MOL-RAO (Deutscher Wetterdienst/Meteorologisches Observatorium Lindenberg–Richard Assmann Observatorium) for the radiation data at Tegel station. Thanks Dr. Andreas Kerschbaumer from Berlin Senate for the PM10 data. Thanks Daniel Fenner from Technische Universität Berlin for the discussion of results and the preparation of radiation data from the UCON (Urban Climate Observation network) stations TUB and Wienerstrasse. This study contributes to the research programme 'Urban Climate Under Change ([UC]²)', funded by the German Ministry of Research and Education (FKZ 01LP1602A). Special thanks go to Patricia Margerison for proofreading this manuscript.

Appendix A. Supplementary data Supplementary data to this article can be found online at https://doi.org/10.1016/j.scitotenv.2018.04.254.

References

American Association for the Advancement of Science (AAAS), 2016. Rise of the city. Science 352, 906–907.

Baklanov, A., Lawrence, M., Pandis, S., Mahura, A., Finardi, S., Moussiopoulos, N., Beekmann, M., Laj, P., Gomes, L., Jaffrezo, J.L., Borbon, A., Coll, I., Gros, V., Sciare, J., Kukkonen, J., Galmarini, S., Giorgi, F., Grimmond, S., Esau, I., Stohl, A., Denby, B., Wagner, T., Butler, T., Baltensperger, U., Builtjes, P., Hout, D., Gon, H.D., Collins, B., Schluenzen, H., Kulmala, M., Zilitinkevich, S., Sokhi, R., Friedrich, R., Theloke, J., Kummer, U., Jalkinen, L., Halenka, T., Wiedensholer, A., Pyle, J., Rossow, W.B., 2010. MEGAPOLI: concept of multi-scale modeling of megacity impact on air quality and

climate. Adv. Sci. Res. 4, 115–120.

Baklanov, A., Molina, L.T., Gauss, M., 2016. Megacities, air quality and climate. Atmos. Environ. 126, 235–249.

Bonn, B., Schneidemesser, E., Andrich, D., Quedenau, J., Gerwig, H., Lüdecke, A., Kura, J., Pietsch, A., Ehlers, C., Klemp, D., Kofahl, C., Nothard, R., Kerschbaumer, A., Junkermann, W., Grote, R., Pohl, T., Weber, K., Lode, B., Schönberger, P., Churkina, G., Butler, T.M., Lawrence, M.G., 2016. AERLIN2014–the influence of land surface types on and the horizontal heterogeneity of air pollutant levels in Berlin. Atmos. Chem. Phys. 16, 7785–7811.

Bright, R.M., Davin, E., O'Halloran, T., Pongratz, J., Zhao, K., Cescatti, A., 2017. Local temperature response to land cover and management change driven by non-radiative processes. Nat. Clim. Chang. 7 (4), 296–302.

Burkart, K., Canário, P., Breitner, S., Schneider, A., Scherber, K., Andrade, H., Alcoforado, M.J., Endlicher, W., 2013. Interactive short-term effects of equivalent temperature and air pollution on human mortality in Berlin and Lisbon. Environ. Pollut. 183, 54–63.

Cao, C., Lee, X., Liu, S., Schultz, N., Xiao,W., Zhang, M., Zhao, L., 2016. Urban heat islands in China enhanced by haze pollution. Nat. Commun. 7. https://doi.org/10.1038/ncomms12509.

Chakraborty, T., Sarangi, C., Tripathi, S.N., 2017. Understanding diurnality and interseasonality of a sub-tropical urban heat island. Bound.-Layer Meteorol. 163 (2), 287–309.

Chao, Z., 1991. Urban climate and air pollution in Shanghai. Energ. Buildings 16 (1), 647–656.

Crutzen, P., 2004. New directions: the growing urban heat and pollution island effect impact on chemistry and climate. Atmos. Environ. 38 (21), 3539–3540.

Dupont, E., Menut, L., Carissimo, B., Pelon, J., Flamant, P., 1999. Comparison between the atmospheric boundary layer in Paris and its rural suburbs during the ECLAP experiment.

Atmos. Environ. 33 (6), 979–994.

Epstein, S.A., Lee, S.M., Katzenstein, A.S., Carreras-Sospedra, M., Zhang, X., Farina, S.C., Vahmani, P., Fine, P.M., Ban-Weiss, G., 2017. Air-quality implications of widespread adoption of cool roofs on ozone and particulate matter in southern California. Proc. Natl. Acad. Sci. 114 (34), 8991–8996.

Estournel, C., Vehil, R., Guedalia, D., Fontan, J., Druilhet, A., 1983. Observations and modeling of downward radiative fluxes (solar and infrared) in urban/rural areas. J. Clim. Appl. Meteorol. 22 (1), 134–142.

Fallmann, J., 2014. Numerical Simulations to Assess the Effect of Urban Heat Island Mitigation Strategies on Regional Air Quality. Universität zu Köln http://kups.ub.unikoeln.de/5913/.

Fallmann, J., Forkel, R., Emeis, S., 2016. Secondary effects of urban heat island mitigation measures on air quality. Atmos. Environ. 125, 199–211.

Fenner, D., Meier, F., Scherer, D., Polze, A., 2014. Spatial and temporal air temperature variability in Berlin, Germany, during the years 2001–2010. Urban Climate 10, 308–331.

Feranec, J., Hazeu, G., Christensen, S., Jaffrain, G., 2007. Corine land cover change detection in Europe (case studies of the Netherlands and Slovakia). Land Use Policy 24 (1), 234–247.

Gabriel, K.M., Endlicher,W.R., 2011. Urban and rural mortality rates during heat waves in Berlin and Brandenburg, Germany. Environ. Pollut. 159 (8), 2044–2050.

Gatari, M.J., Boman, J., 2003. Black carbon and total carbon measurements at urban and rural sites in Kenya, East Africa. Atmos. Environ. 37 (8), 1149–1154.

Gedzelman, S.D., Austin, S., Cermak, R., Stefano, N., Partridge, S., Quesenberry, S., Robinson, D.A., 2003. Mesoscale aspects of the urban heat island around New York City. Theor. Appl. Climatol. 75 (1), 29–42.

Gelaro, R., McCarty, W., Suárez, M.J., Todling, R., Molod, A., Takacs, L., Randles, C.A.,

Darmenova, A., Bosilovicha, A.G., Reichlea, R., Wargan, K., Coy, L., Cullather, R., Draper, C., Akella, S., Buchard, V., Conaty, A., Silva, A.M., Gu, W., Kim, G., Koster, R., Lucchesi, R., Merkova, D., Nielsen, J.E., Partyka, G., Pawson, S., Putman, W., Rienecker, M., Schubert, S.D., Sienkiewicz, M., Zhao, B., 2017. The modern-era retrospective analysis for research and applications, version 2 (MERRA-2). J. Clim. 30 (14), 5419–5454.

Godowitch, J.M., Ching, J.K.S., Clarke, J.F., 1985. Evolution of the nocturnal inversion layer at an urban and nonurban location. J. Clim. Appl. Meteorol. 24 (8), 791–804.

Görgen, R., Lambrecht, U., 2007. Particulate matter in ambient air. J. Eur. Environ. Plann. Law 4, 278–288.

Han, X., Naeher, L.P., 2006. A review of traffic-related air pollution exposure assessment studies in the developing world. Environ. Int. 32 (1), 106–120.

Haywood, J., Boucher, O., 2000. Estimates of the direct and indirect radiative forcing due to tropospheric aerosols: a review. Rev. Geophys. 38 (4), 513–543.

Jauregui, E., Luyando, E., 1999. Global radiation attenuation by air pollution and its effects on the thermal climate in Mexico City. Int. J. Climatol. 19 (6), 683–694.

Jin, M., Shepherd, J.M., Zheng, W., 2010. Urban surface temperature reduction via the urban aerosol direct effect: a remote sensing and WRF model sensitivity study. Adv. Meteorol. https://doi.org/10.1155/2010/681587.

Kuik, F., Lauer, A., Churkina, G., Gon, H.A.D., Fenner, D., Mar, K.A., Butler, T.M., 2016. Air quality modelling in the Berlin-Brandenburg region using WRF-Chem v3.7.1: sensitivity to resolution of model grid and input data. Geosci. Model Dev. 9 (12), 4339.

Lai, L.W., Cheng,W.L., 2010. Urban heat island and air pollution-an emerging role for hospital respiratory admissions in an urban area. J. Environ. Health 72 (6), 32–35.

Lee, X., Goulden, M.L., Hollinger, D.Y., Barr, A., Black, T.A., Bohrer, G., Bracho, R., Drake, B., Goldstein, A., Gu, L., Katul, G., Kolb, T., Law, B.E., Margolis, H., Meyers, T., Monson, R., Munger, W., Oren, R., Paw, U.K.T., Richardson, A.D., Schmid, H.P.,

Staebler, R., Wofsy, S., Zhao, L., 2011. Observed increase in local cooling effect of deforestation at higher latitudes. Nature 479, 384–387.

Lee, X., Gao, Z., Zhang, C., Chen, F., Hu, Y., Jiang,W., Liu, S., Lu, L., Sun, J., Wang, J., Zeng, Z., Zhang, Q., Zhao, M., Zhou, M., 2015. Priorities for boundary layer meteorology research in China. Bull. Am. Meteorol. Soc. 96 (9), 149–151.

Li, H., Wolter, M., Wang, X., Sodoudi, S., 2017. Impact of land cover data on the simulation of urban heat island for Berlin using WRF coupled with bulk approach of Noah-LSM. Theor. Appl. Climatol. https://doi.org/10.1007/s00704-017-2253-z.

Li, H., Zhou, Y., Li, X., Meng, L., Wang, X., Wu, S., Sodoudi, S., 2018. A new method to quantify surface urban heat island intensity. Sci. Total Environ. 624, 262–272.

Lohmann, U., Feichter, J., 2005. Global indirect aerosol effects: a review. Atmos. Chem. Phys. 5 (3), 715–737.

Lubin, D., Simpson, A.S., 1994. The longwave emission signature of urban pollution: radiometric FTIR measurement. Geophys. Res. Lett. 21 (1), 37–40.

Lutz, M., 2013. Mitigation strategies: Berlin, Germany. Particulate Matter: Environmental Monitoring and Mitigation: pp. 74–95 https://doi.org/10.4155/ebo.13.489.

Mahowald, N., 2011. Aerosol indirect effect on biogeochemical cycles and climate. Science 334, 794–796.

McDonnell, M.J., MacGregor-Fors, I., 2016. The ecological future of cities. Science (6288), 936–938.

Meng, X., Zhang, Y., Zhao, Z., Duan, X., Xu, X., Kan, H., 2012. Temperature modifies the acute effect of particulate air pollution on mortality in eight Chinese cities. Sci. Total Environ. 435, 215–221.

Monn, C., Becker, S., 1999. Cytotoxicity and induction of proinflammatory cytokines from human monocytes exposed to fine (PM2. 5) and coarse particles (PM10–2.5) in outdoor and indoor air. Toxicol. Appl. Pharmacol. 155 (3), 245–252.

Munchak, L.A., Levy, R.C., Mattoo, S., Remer, L.A., Holben, B.N., Schafer, J.S., Hostetler, C.A., Ferrare, R.A., 2013. MODIS 3 km aerosol product: applications over land in an urban/suburban region. Atmos. Meas. Tech. 6, 1747–1759.

Ohara, T., Akimoto, H., Kurokawa, J.I., Horii, N., Yamaji, K., Yan, X., Hayasaka, T., 2007. An Asian emission inventory of anthropogenic emission sources for the period 198–2020. Atmos. Chem. Phys. 7 (16), 4419–4444.

Oke, T.R., 1982. The energetic basis of the urban heat island. Q. J. R. Meteorol. Soc. 108 (455), 1–24.

Oke, T.R., 1995. The Heat Island of the Urban Boundary Layer: Characteristics, Causes and Effects. Wind Climate in Cities. Springer, Dordrecht, pp. 81–107.

Ramanathan, V., Carmichael, G., 2008. Global and regional climate changes due to black carbon. Nat. Geosci. 1 (4), 221.

Remer, L.A., Mattoo, S., Levy, R.C., Munchak, L.A., 2013. MODIS 3 km aerosol product: algorithm and global perspective. Atmos. Meas. Tech. 6 (7), 1829.

Rendón, A.M., Salazar, J.F., Palacio, C.A., Wirth, V., Brötz, Björn, 2014. Effects of urbanization on the temperature inversion breakup in a mountain valley with implications for air quality. J. Appl. Meteorol. Climatol. 53 (4), 840–858.

Rizwan, A.M., Dennis, L.Y.C., Liu, C., 2008. A review on the generation, determination and mitigation of Urban Heat Island. J. Ecol. Environ. Sci. 20, 120–128.

Robaa, S.M., 2009. Urban–rural solar radiation loss in the atmosphere of Greater Cairo region, Egypt. Energy Convers. Manag. 50 (1), 194–202.

Rouse, W.R., Noad, D., McCutcheon, J., 1973. Radiation, temperature and atmospheric emissivities in a polluted urban atmosphere at Hamilton, Ontario. J. Appl. Meteorol. 12 (5), 798–807.

Sarrat, C., Lemonsu, A., Masson, V., Guedaliac, D., 2006. Impact of urban heat island on regional atmospheric pollution. Atmos. Environ. 40 (10), 1743–1758.

Schaaf, C.B., Gao, F., Strahler, A.H., Lucht, W., Li, X., Tsang, T., Strugnell, N.C., Zhang, X., Jin, Y., Muller, J.P., Lewis, P., Barnsley, M., Hobson, P., Disney, M., Roberts, G., Dunderdale, M., Doll, C., Entremont, R.P., Hu, B., Liang, S., Privette, J.L., Roy, D., 2002. First operational BRDF, albedo nadir reflectance products fromMODIS. Remote Sens. Environ. 83 (1), 135–148.

Scherer, D., Fehrenbach, U., Lakes, T., Lauf, S., Meier, F., Schuster, C., 2014. Quantification of heat-stress related mortality hazard, vulnerability and risk in Berlin, Germany. DIEERDE–J. Geogr. Soc. Berlin 144, 238–259.

Schwarz, N., Lautenbach, S., Seppelt, R., 2011. Exploring indicators for quantifying surface urban heat islands of European cities with MODIS land surface temperatures. Remote Sens. Environ. 115 (12), 3175–3186.

Shahraiyni, H.T., Sodoudi, S., Kerschbaumer, A., Cubasch, U., 2015. The development of a dense urban air pollution monitoring network. Atmos. Pollut. Res. 6 (5), 904–915.

Sokhi, R.S., Baklanov, A., Piringer, M., 2017. Special issue of journal of urban climate: modelling of urban air pollution and climate interactions. Urban climate 22:1.https://doi.org/10.1016/j.uclim.2017.11.002.

Taha, H., 1997. Urban climates and heat islands: albedo, evapotranspiration, and anthropogenic heat. Energ. Buildings 25 (2), 99–103.

Tapper, N.J., 1990. Urban influences on boundary layer temperature and humidity: results from Christchurch, New Zealand. Atmos. Environ. 24 (1), 19–27.

Vogelmann, A.M., Flatau, P.J., Szczodrak,M., Markowicz, K.M.,Minnett, P.J., 2003. Observations of large aerosol infrared forcing at the surface. Geophys. Res. Lett. 30 (12). https://doi.org/10.1029/2002GL016829.

Wagner, P., Schäfer, K., 2017. Influence of mixing layer height on air pollutant concentrations in an urban street canyon. Urban Climate 22, 64–79.

Wan, Z., 2008. New refinements and validation of the MODIS land-surface temperature/ emissivity products. Remote Sens. Environ. 112 (1), 59–74.

Wan, Z., 2014. New refinements and validation of the collection-6 MODIS land-surface temperature/emissivity product. Remote Sens. Environ. 140, 36–45.

Wan, Z., Dozier, J., 1996. A generalized split-window algorithm for retrieving land-surface temperature from space. IEEE Trans. Geosci. Remote Sens. 34 (4), 892–905.

Wang, L., Gao, Z., Miao, S., Guo, X., Sun, T., Liu, M., Li, D., 2015. Contrasting characteristics of the surface energy balance between the urban and rural areas of Beijing. Adv. Atmos. Sci. 32 (4), 505.

Wei, Y.D., Ye, X., 2014. Urbanization, urban land expansion and environmental change in China. Stoch. Env. Res. Risk A. 28 (4), 757–765.

Xu, L.Y., Xie, X.D., Li, S., 2013. Correlation analysis of the urban heat island effect and the spatial and temporal distribution of atmospheric particulates using TM images in Beijing. Environ. Pollut. 178, 102–114.

Zhao, L., Lee, X., Smith, R.B., Oleson, K., 2014. Strong contributions of local background climate to urban heat islands. Nature 511, 216–219.

Publication list

Li H., Wolter M., Wang X., Sodoudi S. 2017. Impact of land cover data on the simulation of urban heat island for Berlin using WRF coupled with bulk approach of Noah-LSM. *Theoretical and Applied Climatology*. https://doi.org/10.1007/s00704-017-2253-z.

Li H., Zhou Y., Li X., Meng L., Wang X., Wu S., Sodoudi S. 2018. A new method to quantify Surface Urban Heat Island Intensity. *Science of the Total Environment* 624:262-272.

Li H., Meier F., Lee X., Chakraborty T., Liu J., Schaap M., Sodoudi S. 2018. Interaction between urban heat island and urban pollution island in Berlin during summer. *Science of the Total Environment* 636:818-828.

Li H., Zhou Y., Wang X., Zhou X., Zhang H., Sodoudi S. 2019. Quantifying Urban Heat Island Intensity and its Physical Mechanism Using WRF/UCM. *Science of the Total Environment* 650:3110-3119.

Sodoudi S., Zhang H., Chi X., Müller F., **Li H**. 2018. The influence of spatial configuration of green areas on the micro climate and thermal comfort. *Urban Forestry & Urban Greening* 34: 85–96.

Acknowledgements

First of all, I would like to express my sincere gratitude to Prof. Dr. Sahar Sodoudi for her continuous support of my PhD study. Thank her for leading me to the field of urban climate. Thanks for her patience, motivation, and enthusiasm for the guidance throughout my PhD study. Meanwhile, I would like to thank Prof. Dr. Martijn Schaap for his encouragements and insightful comments for my work about atmospheric environment, which is new and interested to me. I learned a lot of useful knowledge and scientific skills from my two supervisors, which are pretty important for my future development.

I would also like to thank the professors and colleagues in the Institute of Meteorology, FUB. Thank Prof. Dr. Ulrich Cubasch and Prof. Dr. Peter Builtjes for their comments and suggestions to my PhD study. Thank Heiwen Zhang, Xun Wang, Michael Wolter, Bo Huang, Xiaoli Chi, Zhihong Zhuo for their help and encouragements during my PhD study. Thank Dr. Ingo Kirchner and Thomas Bergmann for their support in IT technique and numerical modelling. Thank Dr. Hamid Taheri Shahraiyni for the instructions in processing remote sensing data. Thank Dr. Bijan Fallah for the help in programming and thesis writing. Thank Dr. Ines Langer for preparing the datasets of urban observation network. Thank Patricia Margerison for proofreading my publications and the thesis. Thanks to all the other members at the working group of urban climate and climate system modelling for your help and encouragement.

Thank the partners from Iowa State University, Yale University, NCAR, IASS, Peking University, and Chinese Academy of Sciences for their suggestions and help to my PhD study. Thank China Scholarship Council for the financial support to my PhD study. Thank the Beijing Office of Freie Universität Berlin for the help and support during my PhD application.

Finally, I would like to thank my families for their support and encouragements to my PhD study. Love you forever!